Drop-on-demand inkjet printing of amphiphilic peptide I_3K micropatterns on regenerated silk fibroin surfaces to promote neuronal cell attachment and alignment

Ana Jimenez Franco

A thesis submitted to the University of Sheffield in partial fulfilment for the degree of
Doctor of Philosophy

The University of Sheffield

Faculty of Engineering

Department of Chemical and Biological Engineering

April 2023

Acknowledgments

To my parents Berta and Santiago, my sister Marta and her partner Alejandro, for being the constant, unconditional and essential support in this endeavour, for their never-ending love, care, understanding and patience with me all these years, I could not have completed this work without you, and I will be eternally grateful for this!

To my partner, Dr Sergio Rodriguez, for his resilience, company and love during the challenging times, thanks for never stop believing in me when I needed it the most. To his family that never ceased to cheer me up from a very long distance, you were an important motivation from abroad.

My gratitude also goes to my dear friends, Sara Memarpour, Dr Ana M. Sandoval, Dr David H. Ramos and colleague Dr David Alexander Gregory for their valuable guidance, knowledge, and support during the long journey of experimentation. You were a vital part of this process.

Special thanks to my supervisors Prof Joan Cordiner and Prof Ipsita Roy for their exceptional advice, guidance, motivation, and encouragement to complete this work when it seemed to be beyond my reach, the support I received from you was crucial to have made it to this point.

Finally, I would like to thank all my friends back home in Spain, here in the UK and those spread around the world, for believing in me, motivating me, for the really good times we had over these years of pursuing a PhD degree, for the old faithful friend to the wonderful people I met in recent years, thank you!

Publications

Peer-reviewed scientific video journal

Gregory, D. A., Kumar, P., **Jimenez-Franco, A**., Zhang, Y., Zhang , Y., Ebbens, S. J., Zhao, X. Reactive Inkjet Printing and Propulsion Analysis of Silk-based Self-propelled Micro-stirrers. J. Vis. Exp. (146), 2019

Peer-reviewed scientific journal

Weizhen Sun, Yi Zhang, David A. Gregory, **Ana Jimenez-Franco**, Mhd Anas Tomeh, Songwei Lv, Jiqian Wang, John W. Haycock, Jian R. Lu, Xiubo Zhao. Patterning the neuronal cells via inkjet printing of self-assembled peptides on silk scaffolds. Progress in Natural Science: Materials International, 2020

Ting Dai, Jiayi Ma, Su Ni, Chun Liu, Yan Wang, Siyu Wu, Jun Liu, Yiping Weng, Dong Zhou, **Ana Jimenez-Franco**, Hongbin Zhao, Xiubo Zhao. Attapulgite-doped electrospun PCL scaffolds for enhanced bone regeneration in rat cranium defects. Materials Science and Engineering: C., 2022

Piyush Kumar, Ana Jimenez-Franco, Xiubo Zhao. 3D culture of fibroblasts and neuronal cells on microfabricated free-floating carriers. Colloids and Surface B: Biointerfaces. Submitted 16th October 2022, *under review*.

Posters

A. Jimenez-Franco*, D. A. Gregory, J. W. Haycock, and X. Zhao, *Micropatterning of self-assembled peptide I_3K on regenerated silk fibroin substrate to lead proliferation of neuronal cells*, BiTEG, December 2019

A. Jimenez-Franco*, D.A. Gregory , I. Roy & J. Cordiner, *Micropatterning of self-assembled peptide I_3K on regenerated silk fibroin surfaces to guide attachment and proliferation of neuronal cells*, ISPNR, July 2022

A. Jimenez-Franco*, D.A. Gregory, I. Roy & J. Cordiner, *Drop-on-demand micropatterning of self-assembled peptide I_3K on regenerated silk fibroin surfaces to guide neuronal cells attachment and proliferation*, BiTEG, December 2022. Runner-up prize for poster presentation.

Oral presentations

Ana Jimenez-Franco*, David Alexander Gregory, Ipsita Roy, Joan Cordiner, *Drop-on-demand micropatterning of novel amphiphilic peptide I_3K on regenerated silk fibroin substrates to guide and promote adhesion and proliferation of neuronal cells*, TERMIS EU Chapter, March 2023, abstract shortlisted to win the SYIS Oral Presentation Award.

List of Figures

List of Tables

List of Equations

List of Abbreviations

RSF	regenerated silk fibroin
SEM	scanning electron microscopy
Ac-IIIK-NH_2	I_3K
Ac	acetyl group
I	isoleucine
K	lysine
PC12-Adherent	pc12-adh
SF	silk fibroin
SS	silk sericin
S	serine
D	aspartic acid
G	glycine
A	alanine
V	valine
L	leucine
F	phenylalanine
M	methionine
T	threonine
P	proline
Y	tyrosine
C	cysteine
S	serine
D	aspartic acid
E	glutamic acid
H	histidine
R	arginine

PGA	polyglycolic acid
ECM	extracellular matrix
pAAc	poly(acrylic acid)
(PEG)	poly(ethylene glycol)
PDMS	polydimethylsiloxane
nanoHA	nanohydroxyapatite
CNTF	ciliary neurotrophic factor
BDNF	brain derived neurotrophic factor
B. mori	*Bombyx mori*
BMIM Cl	1-butyl-3-methylimidazolium
DMBIM Cl	1-butyl-2,3-dimethylimidazolium chloride
EMIM Cl	1-ethyl-3-methylimidazolium chloride
PTFE	polytetrafluoroethylene
MWCO	molecular weight cut-off
W	weight
wt %	percentage by weight
DSC	differential scanning calorimetry
Cp	heat capacity
T	temperature
TGA	thermal gravimetric analysis
SDS-PAGE	sodium dodecyl sulphate polyacrylamide
FCS	foetal calf serum
DMEM	dulbecco's modified eagle medium
EDTA	ethylenediaminetetraacetic acid
TCP	tissue culture plastic
UV	ultraviolet
FA	formaldehyde
PBS	phosphate buffer saline

NGF	nerve growth factor
DAPI	4′,6-diamidino-2-phenylindole
Phalloidin-FITC	fluorescein isothiocyanate(fitc) labelled phalloidin
BSA	bovine serum albumin
HS	horse serum
F-actin	actin filaments
HEPES	n-2-hydroxyethylpiperazine-n-2-ethane sulfonic acid
AFM	atomic force microscopy
EtOH	ethanol
DoD	drop-on-demand
HTHP	high temperature high pressure
MW	molecular weight
ANOVA	analysis of variance
De	degummed
Td	degradation temperature
Tg	transition glass temperature
Tw	hydration temperature
ROCK	rho kinase
DNA	deoxyribonucleic acid
RNA	ribonucleic acid
NADH	nicotinamide adenine dinucleotide
NADPH	reduced nicotinamide adenine dinucleotide phosphate
MTT	3-(4,5-dimethylthiazol-2-yl)-2,5-diphenyl tetrazolium bromide
PHAs	polyhydroxyalkanoates
PCL	polycaprolactone
PLA	polylactic acid
SAP	self-assembly peptides
IEP	iso-electric point

Θ	contact angle
Ac-I$_3$QGK-NH$_2$	I$_3$QGK
Oh	Ohnesorge number
Re	Reynolds number
We	Weber number
DS	Droplet spacing
OOC	organ-on-a-chip

Table of Contents

Abstract

Silk is a biomaterial mainly composed of two proteins: silk sericin and silk fibroin [1]. After removing the silk sericin using a process called degumming, a regenerated silk fibroin (RSF) aqueous solution can be obtained. RSF has been used previously as a scaffold in tissue engineering due to its high biocompatibility and biodegradability and by varying the production and post-treatment process, RSF can be used for various biological purposes.

However, silk biomaterials can also lack the needed biological activity to support the adhesion and proliferation of cells [2, 3]. In this study, results show that the time of the degumming process can affect the final cell attachment on RSF surfaces. This would allow us to obtain a surface that can be tuned to either promote or prevent cell attachment and thus be used for different applications, while retaining its biocompatibility. Cell attachment of neuronal PC12-Adh cells was studied using crystal violet assay on RSF surfaces obtained from two different times of degumming. Moreover, SEM images and weight-loss during the degumming process were used to check that the removal of sericin was successful.

In addition, the non-adherent RSF surface is then used as a non-fouling surface for inkjet printing. Inkjet printing is a high definition technique that allows to deposit small volumes of liquid onto a surface to form a predefined pattern. This method allows the jetting of proteins and peptides under mild conditions with no waste. A novel amphiphilic peptide Ac-IIIK-NH$_2$ (I$_3$K) is used as a bio-ink to create patterns that can guide cell adhesion and proliferation. I$_3$K is dissolved in an aqueous solution and left to self-assemble to form nanotubes with the positively charged hydrophilic domain facing outwards. In this case, the positively charged I3K strongly interacts with the RSF surfaces via electrostatic interactions preventing the peptide to be redissolved into the culture media. To evaluate cell attachment, proliferation, and differentiation PC12-Adh cells were cultured on the patterns via fluorescent microscopy.

Chapter 1. Introduction

1.1. Silk as biomaterial

Silk is a widely known material. It can be obtained from animals such as silkworms or spiders. Its final purpose also differs depending on the animal producing it, while silkworms spin large amounts only to form cocoons where they will carry out their metamorphosis, spiders produce less quantities but for wider purposes such as web building, reproduction, feeding, etc [4]. Moreover, silk from worms tends to be wider than that from spiders, but spider silk tends to have much better mechanical properties (e.g., higher strain and higher stress) [5-8]. Despite this, both silks have better mechanical properties than most natural or manmade fibres [4].

The domestication of the most common type of silkworm, *Bombyx mori* (*B. mori*) (Figure 1B), provides with a commercial source for silkworm silk which has been used extensively in research during recent years, whereas the aggressivity of spiders and its lower production of silk makes this a less used option, albeit it still used in research [9].

Silk is made up of two proteins called sericin and fibroin. A process called degumming is used to separate the sericin from the fibroin (Figure 1A). Then, the fibres of silk fibroin (SF) can be used for textiles in which the fibroin is woven to make the fabric (Figure 1C). In addition, SF can be re-dissolved in aqueous solution to obtain regenerated silk fibroin solution (RSF). It is this RSF which can be transformed in numerous morphologies, e.g., hydrogels, sponges, films, etc. that can be used in multiple uses in the biomedical field (Figure 1D).

In addition to its versatility to obtain different morphologies, silk has good biocompatibility with almost no immunological response [10] and very good mechanical properties which results in high Young’s modulus and tensile strength [11]. It is these properties which makes silk a good material for biomedical applications. In the last decades, different morphologies have already been used in tissue engineering applications such as bone, nerve, or skin.

In the following section, the amino acid composition and structure of *B. mori* silk will be described. These will have an impact on its properties and therefore on its uses as a biomaterial. Different morphologies of silk and their applications in tissue engineering will be also discussed.

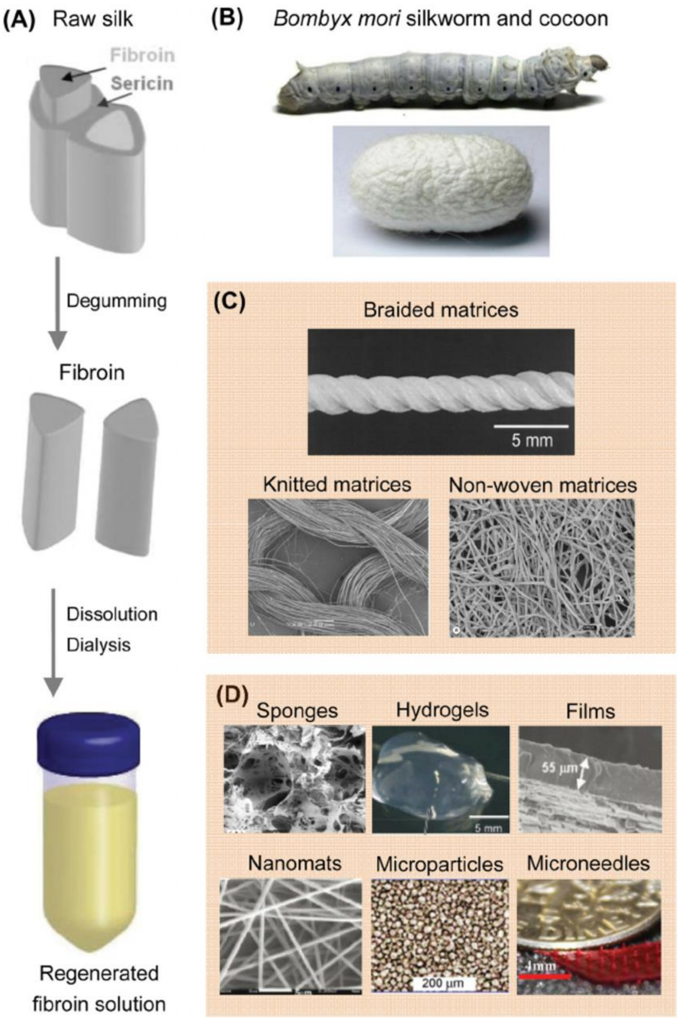

2.1

Figure 1. (A) Schematic of the production process of regenerated silk fibroin from raw cocoons. (B) Image of Bombyx mori silkworm and a cocoon. (C) Examples of materials made from degummed silk fibroin. (D) Examples of materials made from regenerated silk fibroin solution. Reproduced from the work of Koh, L.-D., et al. [10].

1.1.1. Silk properties, fibroin and sericin, polymorphism

Silk is naturally produced protein that is spun in specific glands in animals like silkworms and spiders. Among all of the silk produced, silk from silkworm *Bombyx mori* (*B. mori*) is one of the most studied silks since *B. mori* worms are easily domesticated and they produced large amounts of silk to form their cocoons in comparison with the lower amount of silk produced by spiders. Therefore, this review is going to focus on the structure, composition, and applications of *B. mori* silk in the area of biomaterials and tissue engineering.

Silk amino acid composition

Silk from *B. mori* is formed primarily by two different proteins: 25-30% is silk sericin (SS) and 70-75% would be silk fibroin (SF) [12]. SS acts as a glue, holding together the silk fibroin in the cocoon. It has a high proportion of polar amino acids, such as serine (S) and aspartic acid (D), in its composition with only around 22% of non-polar amino acids [13]. A more detailed amino acid composition of SS can be observed in

Table 1. Sericin has been usually associated with immune responses when used as a biomaterial, therefore it is usually separated from the silk fibroin. However, studies showed that these immunological responses only occurred when sericin was still in some way associated to fibroin and that SS can be used as a biomaterial on its own [14, 15]. Moreover, the use of SS as scaffolds has already been investigated, showing good results for adhesion and growth in bone tissue engineering [16, 17]. There are several methods to extract the sericin from the silk cocoons in a process called degumming. Chemical methods of degumming are the most widely used. Boiling the cocoon in sodium carbonate, dissolving sericin in urea (CH_4N_2O) or lithium bromide (LiBr) are some examples [18]. Other methods include boiling in water or enzymatic extraction using protease [19].

On the other hand, SF makes for about 70-75% of the whole cocoon [12]. Up to 76% of the amino acids found in it are non-polar. The most abundant are glycine (G) (43%) and alanine (A) (30%). The rest of the chain (around 24%) is formed by other amino acids, including some polar amino acids such as serine (S) and tyrosine (Y) [1, 13]. A detailed composition of SF can be observed in

Table 1.

SF is composed of two different domains joined by a covalent disulfide bond at the C-terminus: a heavy chain (390 kD) and a light chain (26 kD) [20, 21]. The heavy chain is formed of 12 crystalline (β-sheets) domains which contain hexapeptides like GAGAGS, short GY-GY subdomains and tetrapeptides such as GAGS or GAAS. These domains are joined together by the irregular GT-GT sequences, which can form turns to join the 12 crystalline domains. On the other hand, the N- and C-terminus of the heavy chain are composed of non-repeating amino acid segments. Moreover, the light chain is also composed of non-repeating units and forms part of the amorphous regions of the silk fibroin [1, 21]. A proposed 2D structure by Ha et. al. [21] can be observed in Figure 2.

Table 1. Amino acid composition of silk sericin (SS) and silk fibroin (SF) expressed in mol%. Adapted from the work of Cao, T.-T. and Y.-Q. Zhang [13]

Amino acids	**SS**	**SF**
Essential for the human body		
Valine (V)	4.05	2.58
Leucine (L)	1.49	0.54
Isoleucine (I)	1.02	0.72
Phenylalanine (F)	0.67	0.81
Methionine (M)	0.31	0.15
Threonine (T)	7.47	0.85
Lysine (K)	2.08	0.33
Non-essential for the human body		
Glycine (G)	17.85	42.62
Alanine (A)	6.70	33.38
Proline (P)	0.81	0.47
Tyrosine (Y)	3.10	5.84
Cysteine (C)	0.38	0.26
Serine (S)	25.50	7.65
Aspartic acid (D)	18.38	1.79
Glutamic acid (E)	5.74	1.36
Histidine (H)	1.32	0.21
Arginine (R)	3.12	0.44

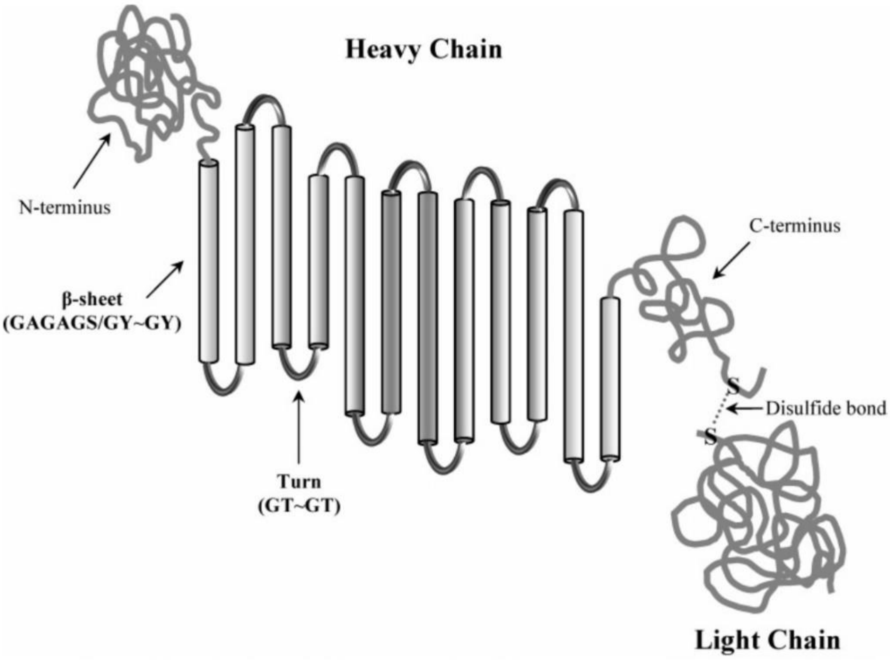

Figure 2. 2-D schematic of the heavy chain and light chain of silk fibroin. Reproduced from the work of Ha, S.-W., et al. [21].

Silk polymorphism

Three different polymorphs have been observed in silk. These are called: silk I (random coil), silk II (β-sheet) and silk III (film observed in air/water interfaces) [1, 22, 23].

Silk I has a random coil structure which is found in the spinning dope of the silkworm. It is water soluble and converts to the more stable silk II when exposed to heat or mechanical strain [1]. In vitro, the conformation change from silk I to silk II can be achieved when the first is exposed to methanol [24, 25]. Silk II consists of the secondary, more stable, crystalline β-sheet structure with amorphous domains between sheets. This structure is asymmetrical. It is arranged in a way that has the methyl side chain from the alanine to one side and the hydrogen side chain from glycine to the other. This helps forming strong hydrogen bonds between adjacent sheets [1]. The good mechanical properties of silk fibroin are a result of those inter-chain interactions [26]. In addition, this structure is insoluble in water and in other solvents even in mild acid and alkaline conditions [1]. The last known structure, silk III, is present in the water-air interface with a helical structure [23].

1.1.2. Properties of silk as a biomaterial

When comparing silk with other natural biopolymers, it is its good mechanical properties that makes silk stand out. Moreover, silk also has good biocompatibility and biodegradability rates which makes silk a good biomaterial. However, silk has a very low biological activity [27] which results in poor cell attachment. This is due to its highly hydrophobicity and high content of non-polar groups (up to 76%) [13]. Hydrophobicity and the presence of non-polar groups are important properties which can hinder cell attachment and growth [28].

Mechanical properties

Native silk fibre has a high Young's modulus (10-17 GPa) and high tensile strength (300-740 GPa) [10]. These makes silk a tough and ductile material, which can be used for load bearing scaffolds in tissue engineering. These properties are related to the hierarchical structures of silk fibres, mainly due to the inter-chain hydrogen bonds formed between β-sheets and hydrophobic interactions [10].

However, it is important to note that even though native silk fibre has good mechanical properties, materials made from silk fibroin solutions are weak and brittle [29], showing a lower tensile strength than native fibres [30]. The reason for this is that the regenerated fibroin lose the main structure of the native silk during processing [29]. Some examples can be seen in Table 2.

Table 2. Mechanical data of native silk and different morphologies of regenerated silk. Adapted from the work of Koh, L.-D., et al. [10].

	Young's modulus (GPa)	**Ultimate strength (MPa)**
Silkworm silk fibroin (*B. mori*)		
Silk fibroin	10-17	300-740
β-sheet crystallites	16-18	-
Silk Regenerated morphologies		
Methanol-treated sponges (6 wt%)	0.00043	0.02
Aqueous-derived sponges (4 w/v %)	0.00007-0.00013	0.011-0.013
Aqueous-derived sponges (8 w/v %)	0.0013-0.0033	0.1-0.32
Hydrogels (8 w/v %)	-	0.0252
Films (cast)	3.9	47.2
Films (methanol-treated)	3.5	58.8

Electrospun mat (conc. 15%, 2kV/cm and 5 cm spinning distance)	0.515	7.25
Electrospun mat (conc. 3%, 1kV/cm and 10-15 cm spinning distance)	-	15

Several methods including methanol treatment, water annealing treatment, different processing temperatures, etc. can be used to enhanced the mechanical properties of the regenerated fibroin [10]. Moreover, regenerated fibroin can be blended or chemically bound to other natural (e.g. collagen [31] or cellulose [32]) or synthetic polymers (polyethylene oxide [33] or nylon 66 [34]) to achieve better mechanical properties.

Biocompatibility

Silk has been used as sutures before, which have proven the biocompatibility of this material [35]. Nowadays, silk is also used as scaffolds for tissue engineering. However, removal of the sericin from native silk is an important step to improve the biocompatibility. Sericin, when still associated to the SF, has proven to cause some immunological responses [14, 15]. The biocompatibility of SF materials when degummed and sterilised properly can be compared to that of collagen or poly(lactic acid) [29].

Tang et al. proved that degummed silk fibres can support the proliferation *in vitro* of hippocampal neuron cells showing with no significant cytotoxicity [36]. Moreover, the inflammatory response of silk fibroin conduits compared to collagen conduits, or an autograft *in vivo* was studied by Ghaznavi et. al [37]. Silk showed more macrophage response than collagen with similar nerve repair. On the other hand, the subcutaneous implantation of silk and polyglycolic acid (PGA) scaffolds in rats showed less inflammatory response in silk than in PGA scaffolds [38].

Biodegradability

Biodegradation is the disintegration of materials by any biological mean such as enzymes, bacteria, etc. This term applied to the field of tissue engineering includes in its definition that the elements obtained after disintegration of the scaffold can be removed from the original location but not necessarily from the body [29]. In contrast, the elimination of those elements through filtration or metabolic pathways is known as bio-sorption.

Protease XIV is the most commonly used enzyme for biodegradation studies of silk *in-vitro* [39-41]. These studies proved that the degradation rate for silk can be predicted which can help design better scaffolds that can meet different requirements. This degradation is related to the crystallinity of the RSF materials. Lu et al. proved that the non-crystal blocks move to the solution of protease due to its hydrophilicity leaving behind the crystal blocks with a high β-sheet content [42]. Therefore, controlling the crystallinity of RSF materials, the rate of degradation can also be controlled.

Fragmentation of the silk fibroin, a decrease in the mechanical properties and thickness are some of the results of the exposure to the enzymes. However, Numata et. al. proved that the natural degradation with alpha-chymotrypsin showed less cytotoxicity than the degradation using protease [39].

On the other hand, studies of the *in vivo* responses to the use of silk scaffolds show mild inflammation and macrophage activation. It has been demonstrated that these responses are associated with the structure and morphology that results from different methods of preparing the different types of scaffolds [43, 44].

Cellular attachment

Cell attachment to silk fibroin scaffolds is poor [2]. This may be related to the high content of non-polar amino acids [13] and the crystalline hydrophobic structure of silk II [1]. Improving cell attachment on silk materials can be achieved by various methods including plasma treatment [45], coating or chemically binding silk with extracellular matrix (ECM) proteins such as laminin [46], fibronectin [27], collagen [47] or peptides derived from them such as IKVAV ("I" represents amino acid isoleucine, "K" lysine, "V" valine and "A" alanine)[48] or RGD ("R" is arginine, "G" glycine and "D" aspartic acid) [49]. For example, Hu et al. mixed silk fibroin with tropoelastin in different ratios proving that increasing the tropoelastin content led to better adhesion of primary cortical neurons [50]. However, neurons in silk fibroin only formed clusters whereas cell death occurred when the films were formed only of tropoelastin. Results from this study can be seen in Figure 3.

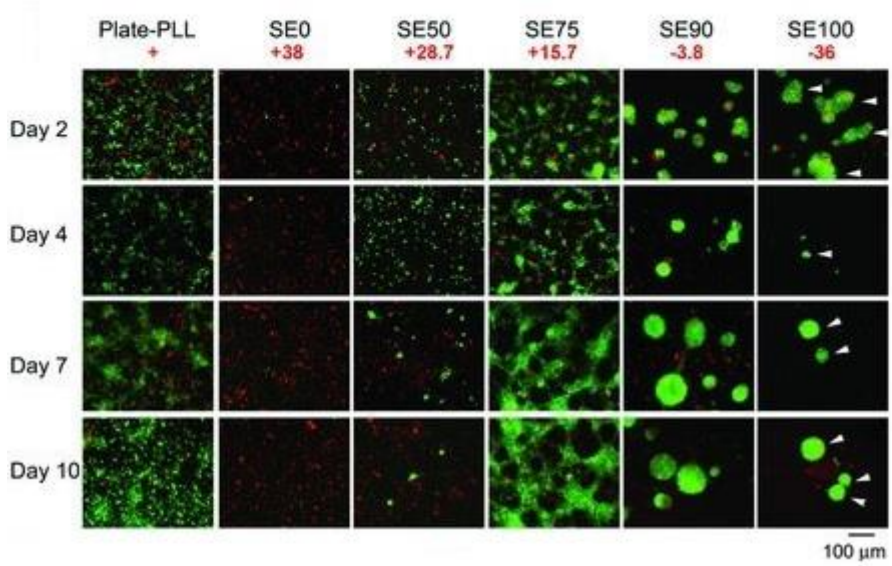

Figure 3. Fluorescence image of live dead (green) and dead cells (red) of primary cortical neuronal cultures on silk-tropoelastin alloy films at different ratios and control (plate coated with poly L-lysine) over different days. Partially reproduced from the work of Hu, X., et al. [50].

The modification of silk surfaces by these methods can provide a way to tune the hydrophilicity of SF surfaces and obtain control over cell adhesion [2]. Dhyani et al. have grafted poly(acrylic acid) (pAAc) or poly(ethylene glycol) (PEG) to the surface of regenerated silk films to obtain hydrophilic surface which then were seeded with HeLa and L6 cells. The pAAc-SF surfaces proved to be hydrophilic and have high cell adhesion, whereas the PEG-SF surfaces were still hydrophilic but had lower cell adhesion. This way they could tune the cell adhesion from low to high and back to low as can be seen in Figure 4.

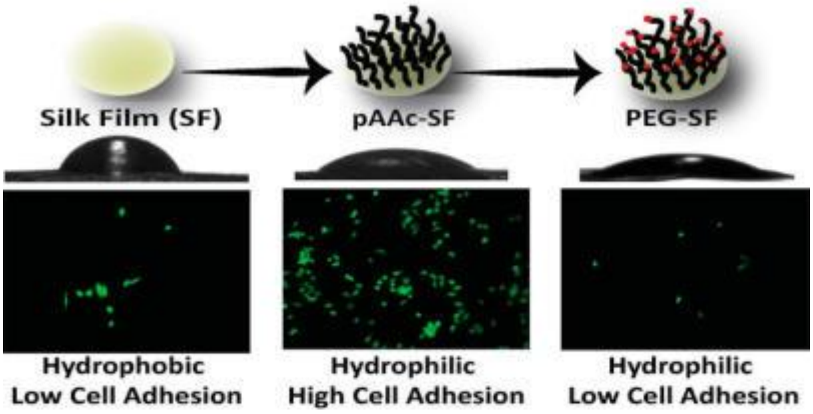

Figure 4. Tuneable cell adhesion on silk films via grafting pAAc on silk or PEG on pAAc. Reproduced from the work of Dhyani, V. and N. Singh [2]

1.1.3. Morphology of different silk biomaterials

Aqueous solutions of silk fibroin can be obtained by dissolving silk fibroin after the removal of the sericin, also known as degumming. Then, silk fibroin can be re-dissolved by either using lithium bromide (LiBr) [51] or Ajisawa's reactant [52]. Once SF is in aqueous solution, which is called regenerated silk fibroin (RSF), different materials such as hydrogels, fibres, films, etc. can be obtained as it is shown in Figure 5.

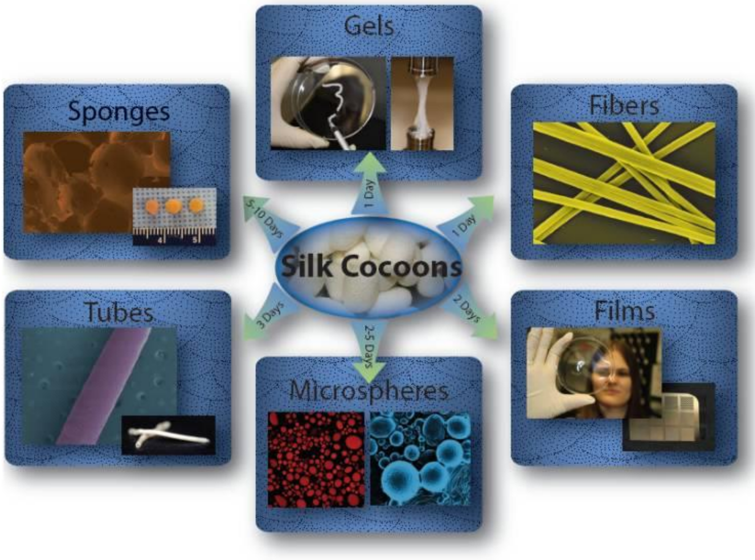

Figure 5. Schematic of different materials made from silk fibroin. The arrows indicate the time needed to make the materials from the aqueous silk solution. Reproduced from the work of Rockwood, D.N., et al. [12].

For example, different methods can be used to make SF hydrogels. Sonication of the SF solution will induce the change from random coil to β-sheet, forming a gel [53]. On the other hand, Yucel et al. proved that gelation could be achieved by a vortex mixer that would promote the same change to β-sheet [54]. The formation of SF hydrogels can be affected by pH, fibroin concentration, temperature, and time of processing. SF hydrogels have been used for soft tissues applications such as cartilage and skin [55] due to its similar nature. Improving the mechanical properties of such hydrogels would allow their use in load-bearing applications such as bone tissue engineering [56].

On the other hand, the most common method to make silk films is by casting the aqueous solution onto different substrates. Both patterned and non-patterned silk films can be obtained using different methods [12]. According to Rockwood et al., drying the silk solution directly in a petri dish would give non-patterned films but a pattern can be obtained using, for example, PDMS (polydimethylsiloxane) moulds [12]. Methods like alcohol immersion are usually used to improve the crystallinity of these silk films [29]. These silk films are usually transparent which makes them good materials for cornea tissue engineering applications [57].

More advanced methods to control surface properties of the films are for example lithography or inkjet printing. These techniques allow more accurate patterns to be obtained. For example, a highly cell adhesive pattern can be printed on top of a non-adhesive background to control the attachment of cells [58]. Moreover, cells can be printed with a specific pattern using an inkjet printer without showing a reduction in cell viability [59]. All in all, inkjet printing can be a good technology for creating more advanced scaffolds.

1.2. Silk functionalisation

As described before, SF materials can have issues with low cell-adhesive activity, loss f mechanical properties after processing and variability in biodegradation and bioactivity. For these reasons the functionalisation of SF materials is widely studied. There are different approached to functionalise silk. For example, chemical modification, the use of transgenic worms, and physical modification. All of these approaches can resolve some of the issues with SF biomaterials.

For example, Tamura et al. [60] used *piggyBac* transposons to modify the gene expression of *B. mori* silkworms that can then produce recombinant proteins without the need for further modifications. This opened the field to multitude of applications. In particular, Kambe et al. [61] genetically introduced the Arg-Gly-Asp-Ser (RGDS) sequence into the light chain of silk fibroin. The effect of this was investigated on chondrocyte adhesion and, while properties such as wettability were not changed, cell adhesion was improved by this modification. However, these approached depends on the ability of the transgenic silkworms to express the recombinant protein which in some cases can be poor [62].

SF surface modification depends largely on the ability to link such ligands to the SF protein. The heavy chain of silk proteins can contain more than five thousand amino acids, of these only around 20 mol% are considered chemically active amino acids with functional side chains [63]. The presence of active amino acids is even less in the SF light chain. This is important, when considering different crosslinking strategies such as chemical modification, seen in Figure 6.

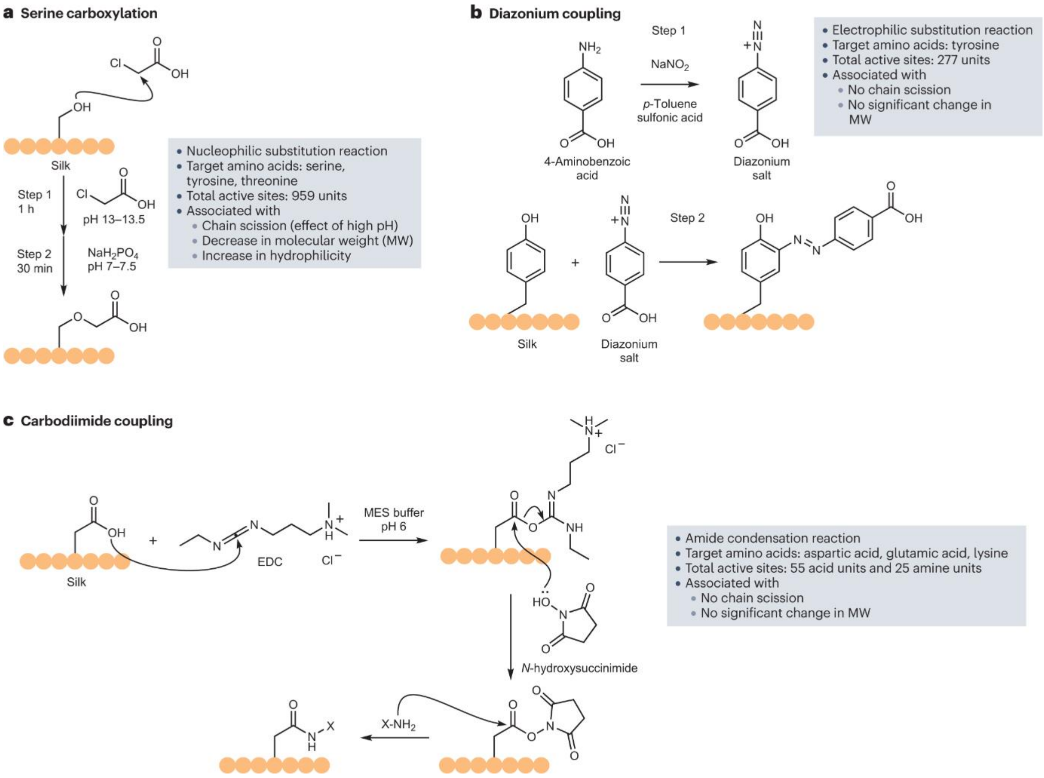

Figure 6. Summary of chemical modifications of silk proteins: a) carboxylation, b) diazonium coupling and c) carbodiimide coupling. This graph includes main reactions, catalysts, target amino acids and some outcomes for each reaction such as chain scission and change in molecular weight. Reproduced from the work of Sahoo et al. [63]

The most commonly used chemical modification of silk is carboxylation chemistry. In this case, hydroxyl groups are deprotonated in serine, tyrosine or threonine amino acids in high alkaline conditions [64-66]. Using this method, properties such as polymer charge and hydrophilicity can be tailored to specific applications. Another approach is using diazonium coupling [65-67] during which multiple functional groups such as carboxylic acid, amines or ketones can be added to the tyrosine units of the silk heavy chain, modifying the wettability of silk materials. For example, Murphy et al. [67] used diazonium coupling chemistry to increase the hydrophilicity of SF proteins. In this case, growth and morphology of hMSCs (Human Mesenchymal Stem Cells) were affected by the degree of hydrophilicity of the SF material.

However, one of the most used reactions involved in silk modification is carbodiimide coupling. This occurs in the presence of 1-ethyl-3-(3-dimethylaminopropyl)-carbodiimide

(EDC) and *N*-hydroxysuccinimide (NHS) in aqueous solution at around pH 6. Using this method, multiple of different ligands have been incorporated into silk: vitamins [68], peptides [69-71], sugars [66] and proteins [72]. Although this coupling is favoured due to the abundance of acid and amine residues in silk molecules, this can also lead to intra and interchain crosslinking [65].

All of this highlights the challenges of silk chemistry: lack of readily available reactive residues which results in low degrees of functionalisation, intrachain and interchain crosslinking; external stimuli such as changes in temperature or pH, sonication, vortexing can induce gelation and β-sheet formation decreasing solubility and forming silk aggregates. In addition, chemical modifications of silk are limited to aqueous solutions to avoid phase separation and precipitation of the SF proteins.

All of these approaches above involve covalent interactions to incorporate the bioactive motifs into the SF proteins. However, there is another approach which involves using supramolecular crosslinking such as non-covalent interactions to obtain dynamic and reversible links. In this case, highly ordered structures known as self-assembly are being used in the fabrication of synthetic biomaterials. Synthetic peptides have played a key role in the field of self-assembled biomaterials [73]. These are of particular interest due to their high biocompatibility and biodegradability. In addition, their synthesis is a highly scalable and cost-effective process.

1.3. Silk in tissue engineering

Trauma, injuries, or disease can cause the deterioration or atrophy of different tissues or organs of the human body. One of the most typical treatments is using tissue, organs or cells from one person (donor) to another (recipient), this is called an allograft or allotransplantation [74]. Problems associated with this can be infection and rejection by the patient's immune system since the transplanted part is recognized as a foreign material and, as such, is attacked by the immune system, taking immunosuppressant drugs can lower the chances of rejection. On the other hand, tissue and cells can be transplanted from one part of the body to another in the same person. This is called an autograft or auto transplant [74]. This process reduces the possibility of rejection since the body does not identify the transplanted part as a foreign material. However, harvesting the required body part can be painful and difficult to reach. This method is also associated with site morbidity due to infection and hematoma.

Tissue engineering uses a combination of cells, materials, and biological active molecules to grow functional tissue that can repair or improve damaged tissue and organs. The aim of tissue engineering is to provide the appropriate environment for the tissue or organ to regenerate, which is achieved with the use of scaffolds.

The good mechanical properties and biocompatibility of silk materials and their versatility to be adapted into a wide range of morphologies make silk a great material to use in tissue engineering applications such as bone, skin, or nerve.

1.3.1. Bone tissue engineering

Good mechanical properties are needed to ensure the success of bone scaffolds, for that reason silk makes a good choice for this application. The use of silk for bone regeneration is one of the most used applications of silk.

Different morphologies can be used. For example, Ribeiro et. al. developed a silk fibroin and nanohydroxyapatite (nanoHA) hydrogel suitable for bone regeneration [56]. Including the nanoHA in the hydrogels improved the mechanical properties and cellular metabolic activity. On the other hand, electrospun fibres with nanoHA and/or bone morphogenetic protein were seeded with human bone marrow-derived mesenchymal stem cells and used for in vitro studies [75] which showed enhanced bone formation. Reinforcing scaffolds with other components can sometimes prove difficult due to poor interaction between the components. For this reason, silk-silk composites are being developed. For example, silk particles were incorporated into silk sponges improving the compressive modulus of the sponges and slowing degradation [76]. These structures could be useful for bone regeneration and other load-bearing applications.

1.3.2. Skin tissue engineering

Human skin consists of a complex structure composed of three layers: epidermis, dermis, and hypodermis. Each layer has a different composition, e.g., the dermis is rich in collagen while the epidermis has keratin. Also, the dermis contains hair follicles, glands, blood vessels and nerve endings. For these reasons, scaffolds for skin regeneration are difficult to design.

Silk can be combined with different biomaterials like collagen-I or fibronectin to mimic the structure of the skin. For example, silk fibroin coated with fibronectin supports adhesion and dispersion of both keratinocytes and fibroblasts cells while collagen-I only supports keratinocytes and no fibroblasts [29]. Other composites of silk were successfully used in skin regeneration like silk-chitin [77] and silk-alginate [78]. Furthermore, Jeong et al. treated silk nanofibers with plasma in presence of oxygen which increased its hydrophilicity [45]. This resulted in increased cell activity compared to the untreated nanofibers.

1.3.3. Nerve tissue engineering

Nerve regeneration is often challenging. While small gaps (<5 mm) in nerves can be solved by suturing (also known as neurorrhaphy), larger gaps between nerves require the use of other techniques such as autografts [79, 80]. These autografts are harvested from another part of the body which can lead to site morbidity or deformities.

Recently, polymers such as poly(lactic acid) [81] have been used to create artificial nerve grafts or channels that can help with nerve regeneration but also, natural polymers such as silk fibroin have been studied for this application [82]. Moreover, the biocompatibility of SF with nerve tissues has already been evaluated, proving that SF is cytocompatible and a good candidate for this type of tissue engineering applications [36, 79, 83].

Different silk fibroin biomaterials such as electrospun fibres, hydrogels or films can be used for nerve regeneration. For example, Sun et al. prepared silk hydrogels with covalently linked IKVAV by sonication for brain tissue regeneration [48], the silk-IKVAV hydrogel showed higher proliferation and differentiation of neural cells than the unmodified silk hydrogels.

On the other hand, the use of different growth factors such as Ciliary Neurotrophic Factor (CNTF) and Brain Derived Neurotrophic Factor (BDNF) can increase the growth of neurites by almost three times when using both factors compared to non-functionalised fibers [84]. Combination of electrospun poly(lactic acid) (PLA) and SF nanofibres with Nerve Growth Factor (NGF) supported cell adhesion and differentiation of PC12 cells [85].

However, in the field of peripheral nerve regeneration, aligned and oriented microchannels are important cues to guide the growth and development of neurites. Dinis et al. [82] developed a bi-functionalised silk electrospun conduit comprising of CNTF and NGF bioactive motifs. Moreover, these were designed with longitudinally oriented channels to mimic the architecture found in native nerve tissue. They found that the addition of growth factors did not affect the secondary structure of the SF material, which displayed similar mechanical properties to that of native sciatic nerve in rats.

1.3. Overview of project

Silk is proposed as a good biomaterial with good mechanical properties, biocompatibility, and biodegradation. However, the interaction between silk biomaterials and cells is, in general, poor. The need to combine silk with other materials, such as natural or synthetic polymers, proteins, or peptides, is of great relevance to obtain a successful scaffold for its application in tissue engineering.

In this project, it is proposed to use silk as a biomaterial for peripheral nerve regeneration and combine it with synthetic peptides. Some examples of these peptides are I_3K, I_3KVAV (where “I” represents amino acid isoleucine, “K” lysine, “V” valine and “A” alanine) or I_3RGDS (where “I” represents amino acid isoleucine, “R” is arginine, “G” is glycine, “D” is aspartic acid and “S” is serine). I_3KVAV is the primary domain for bioactivity of the protein laminin and has also been used effectively to improve adherence of neuronal cells [46, 86, 87]. On the other hand, I_3RGDS corresponds to the cell attachment site of fibronectin and has been widely used to improve cell attachment of scaffolds [49, 88-91]. Both laminin and fibronectin can be found naturally in the extracellular matrix (ECM), and synthetic scaffolds try to mimic this ECM to obtain a successful scaffold [92]. Other novel peptides, like I_3K (where “I” represents amino acid isoleucine and “K” lysine) or I_3QGK (where “I” represents amino acid isoleucine, “Q” glutamine, “G” glycine and “K” lysine), which to our knowledge have not been used in tissue engineering before excluding this research group, will also be used to improve silk scaffolds. However, these peptides alone cannot provide a substrate with the good mechanical properties needed for scaffolds. In this case, silk will provide a good substrate with good mechanical properties while the synthetic peptides will provide the required cell interaction to fulfil the purpose of the scaffold.

On the other hand, the morphology of the scaffolds has a great impact in its performance as good substrates for tissue growth. Properties such as topographical cues and spatially controlled patterns will affect the way the cells interact with the scaffolds. These need to be small enough that they recognisable cues for the cells to promote adhesion, proliferation and even differentiation. For this reason, the use of different methods like inkjet printing or spin coating will provide further understanding of the effect of different morphologies in the use of peptide coated silk scaffolds for the culture and differentiation of neuronal cells.

Chapter 2. Materials and methods

2.1. Materials

Raw silk cocoons were obtained from State key lab of silkworm genome biology, Southwest University, China. Synthetic peptide I_3K was obtained from GL Biotech Co Ltd, Shanghai, China. PC12-Adh immortalised cell line was kindly given by the biomaterials and tissue engineering group at The University of Sheffield. All other chemicals were obtained commercially at analytical grade from Sigma Aldrich unless stated otherwise.

2.2. Preparation of regenerated silk fibroin solution

Natural silk is composed of two main proteins: silk sericin and silk fibroin. The sericin is usually removed via a process called degumming and discarded. The silk fibroin obtained this way can then be redissolved to form an aqueous solution called regenerated silk fibroin (RSF) solution which can be used for different applications. The overall process can be seen in Figure 7.

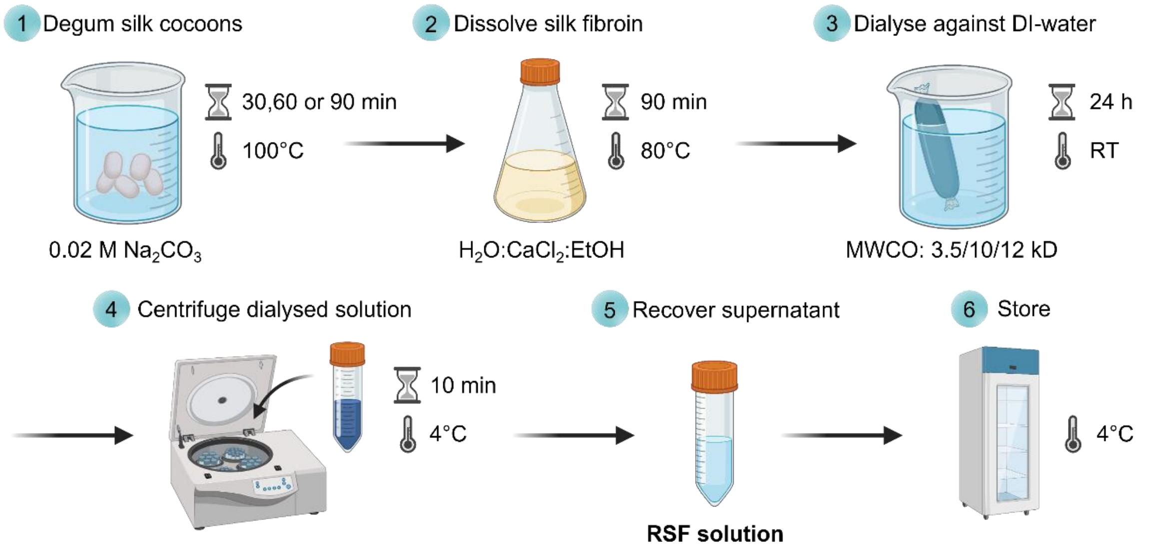

Figure 7. Schematic of the whole process to obtain a regenerated silk fibroin RSF solution from raw cocoons. Created with BioRender [93].

2.2.1. Silk degumming

Raw silk produced by *Bombyx mori* (*B. mori*), a domesticated type of silkworm, is a composite material of silk fibroin (70-75%), sericin (25-30%) [12]. Silk degumming is the process where the sericin is removed to obtain clean individual silk fibroin fibres. This process can be done using different methods or agents such as alkali, acid, high pressure or enzyme [94-96] In this case, an alkali such as sodium carbonate (Na_2CO_3) is used as described below.

Degumming via Na_2C0_3 solution

Briefly, 5 g of raw silk cocoons from *B. mori* were cut into small pieces (~0.25 cm^2) and cleaned in warm deionised water. A beaker containing 2 L of deionised water was placed on a hotplate and brought to a boil at 100°C. Then, 4.24 g of Na_2CO_3 were added to make a 0.02 M solution. Once the sodium carbonate had completely dissolved with the help of a rotating magnetic stir bar, the silk cocoon is added and left for the specified amount of time, e.g., 30, 60 or 90 min. The beaker was partially covered with aluminium foil to prevent excess evaporation of the solution, and pre-heated deionised water was added if the volume was lower than 2 L.

After the specified amount of time, the silk fibroin (SF) fibres can be recovered using a Buchner funnel equipped with a miracloth discarding the solution. SF fibres were then rinsed 5 - 6 times with clean deionised water to remove any sericin or Na_2CO_3 that may have remained. Fibres were then spread out in a crystallisation disk and dried at room temperature or in an oven set at 60°C until completely dried. Then, they can be stored in a hermetically sealed bag for long-term storage at room temperature.

2.2.2. Weight loss due to degumming

As stated before, 25 - 30% of the raw silk cocoon is made of the protein sericin. During degumming this protein is removed and therefore, by calculating the weight lost during the process we can estimate if the sericin has been successfully removed. Briefly, the raw cocoons were weighed before degumming and the silk fibroin fibres were also weighed after drying. The difference between these, as seen in Equation 1, gave an estimation of the sericin lost during the process

$$\text{weight loss\%} = \frac{\text{mass of raw cocoon (mg)} - \text{mass of silk fibroin (mg)}}{\text{mass of raw cocoon (mg)}} \times 100$$

Equation 1. Equation used to calculate the weight loss (%) due to the removal of silk sericin during the degumming process

A weight loss of 25 to 30 percent was considered as a successful degummed silk fibroin.

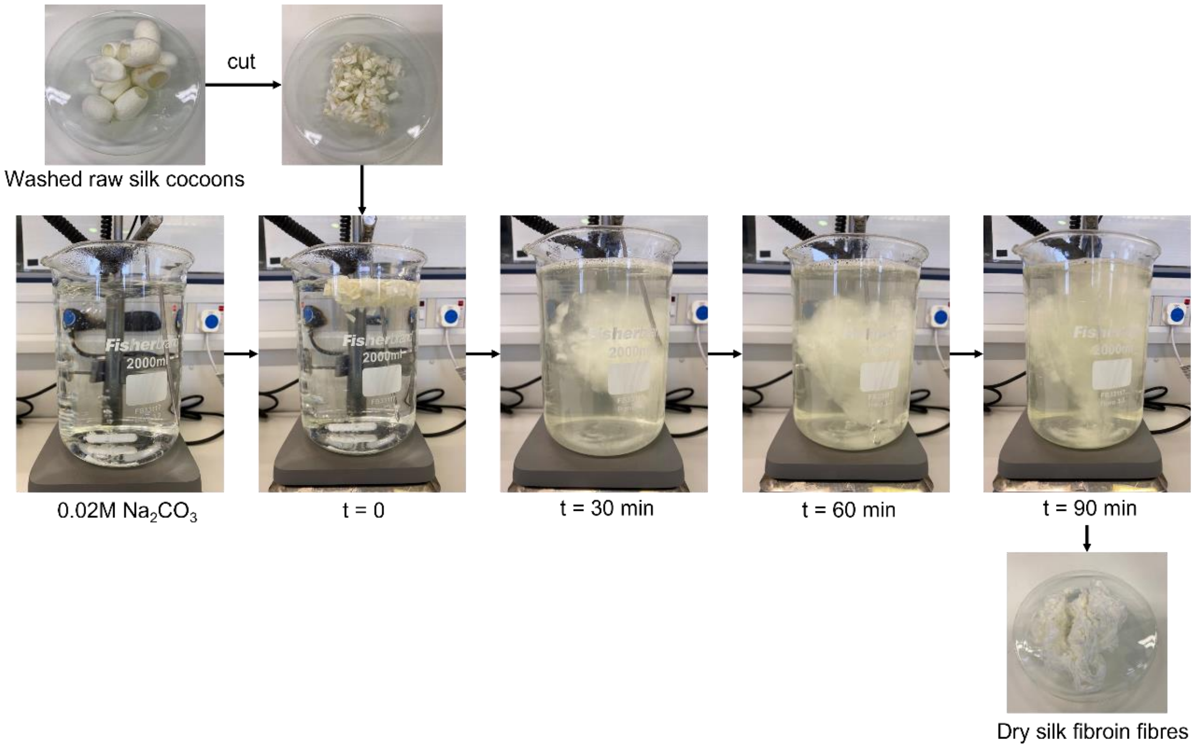

Figure 8. Images of the degumming process at different time points.

2.2.3. Dissolution of silk fibroin

After removing the sericin protein, silk fibroin proteins are in the form of fibres. Although this material is useful for the textile industry for example, the final objective is to obtain a solution of SF proteins denominated regenerated silk fibroin (RSF) solution that can be further used for different applications. This solution can be obtained using different solvents such as lithium bromide (LiBr) solution, a ternary solution composed of calcium chloride:ethanol:water (also known as Ajisawa's reagent [52]) and, more recently, ionic liquids such as 1-butyl-3-methylimidazolium chloride (BMIM Cl), 1-butyl-2,3-dimethylimidazolium chloride (DMBIM Cl) and 1-ethyl-3-methylimidazolium chloride (EMIM Cl) [97]. In this study, Ajisawa's reagent was used, and the method used is described below.

Dissolution of silk fibroin via Ajisawa's reagent

Degummed silk fibroin fibres were dissolved using Ajisawa's ternary reagent composed of a mixture of calcium chloride:ethanol:water ($CaCl_2$:EtOH:H_2O) in a molar ratio of 1:2:8 [52]. To make the reagent, 9.3 g of $CaCl_2$ were dissolved in 14.4 of filtered (0.2 µm PTFE filter, Fisherbrand) deionised water under continuous stirring. Once dissolved, the solution was again filtered (0.7 µm PTFE (polytetrafluoroethylene) filter, Fisherbrand) and then added to 11.1 g of filtered (0.2 µm PTFE filter, Fisherbrand) ethanol. This ternary solution is then poured into a two-neck round bottom flask placed inside a water bath that is heated on a hotplate. This flask is equipped with a thermometer to check and control the solution's temperature. Once the ternary solution is heated to 80°C, 3 g of degummed silk fibroin is added and left to be dissolved for 90 min under continuous stirring with a small magnetic bar.

2.2.4. Dialysis of regenerated silk fibroin solution (RSF)

Since the dissolution process is a salt-based method, this salt needs to be removed from the solution to obtain the final RSF solution so it can be used for future applications. Three different dialysis tubes are used for this with a different molecular weight cut-off (MWCO): cellulose tube with MWCO 12,000 (Sigma-Aldrich) and SnakeSkin tube with MWCO of 10,000 and 3,500 (ThermoFisher).

Briefly, the solution was cooled down, divided in three and poured into the three dialysis tubes which are tightly closed on one end. After the tubes are filled, the open end is closed with a clip and equipped with an empty plastic tube to make it float. Then, each tube is placed in a beaker with 2 L deionised water and equipped with a magnetic stirrer. The water was changed at specific intervals of time, e.g., 0.5 h, 1 h, 2 h, 4 h, 20 h and 24 h, to promote the removal of salts from the solution. The conductivity of the water is measured in each change to follow the dialysis process. The dialysis is considered finished when the conductivity of the water is less than 10 µS/cm.

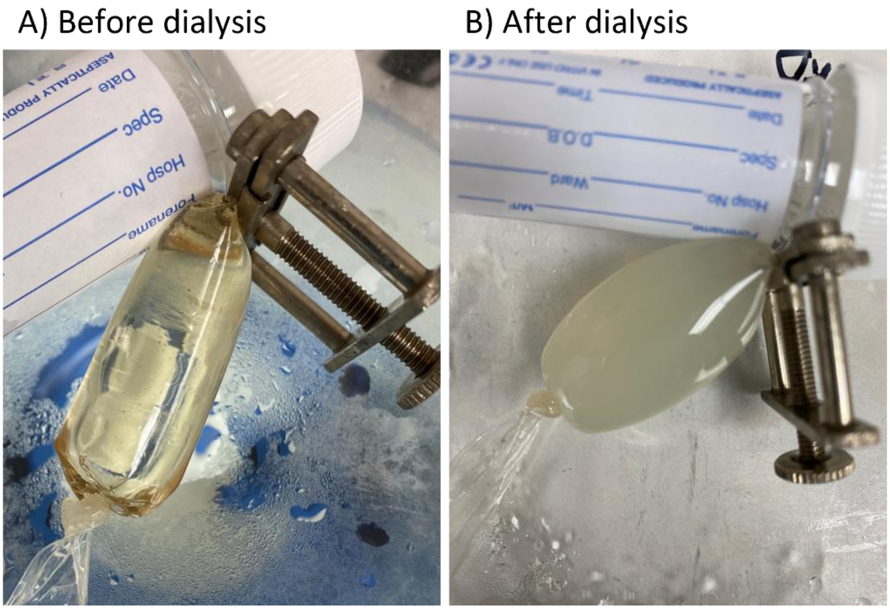

A) Before dialysis

B) After dialysis

Figure 9. Images of RSF solution inside the dialysis tube before and after the dialysis process.

2.2.5. Centrifugation, measure of concentration and storage

When removing the salts through dialysis, the solubility of the silk fibroin decreases, and some might precipitate. This can cause gelation of the solution and therefore, centrifugation is required to remove any debris. The solution is split in 1.5 mL Eppendorf tubes and centrifuged at 13,000 rpm for 15 min at 4°C using a Heraeus Biofuge Fresco refrigerated centrifuge. The supernatant is recovered and stored at 4°C.

Briefly, approximately 200 mg of RSF solution are deposited on a pre-weighed glass slide. The exact weight of the solution is calculated by subtracting the weight of the glass slide, W_1, to total weight (solution and glass-slide) W_2. After drying in an oven at 60°C for 24 h, the glass slide is weighed again (W_3), and the dry sample mass can be calculated by subtracting the weight of the glass slide, W_1, to the total dry weight, W_3. The concentration of the RSF solution expressed as weight percent wt% is calculated with the following Equation 2,

$$\mathrm{wt\%} = \frac{\text{mass of solute (mg)}}{\text{mass of solution}} \times 100 = \frac{\mathrm{W}_2 - \mathrm{W}_1}{\mathrm{W}_3 - \mathrm{W}_1} \times 100$$

Equation 2. Equation used to calculate the gravimetric concentration (wt%) of the RSF solution.

W_1 is the mass of a clean glass slide in mg

W_2 is the mass of the solution added and the glass slide in mg

W_3 is the mass of the dried solution and glass slide

Figure 10. Example of RSF solution after dialysis and centrifugation.

2.3. Characterisation of Silk Fibroin Fibres

2.3.1. Scanning electron microscopy (SEM)

Scanning electron microscopy (SEM) is a type of microscopy where a beam of focused electrons is used to scan the surface of a sample. The electrons are absorbed or scattered by the topography of the sample, and this can be detected to produce a high-resolution image at a very high magnification.

Briefly, dried degummed SF fibres were placed onto carbon adhesive pads (Agar Scientific, United Kingdom) that were mounted on aluminium stubs (Agar Scientific, United Kingdom). To improve the quality of the final image, samples were gold coated (Q150R S, Quorum Technologies, UK). After this, the sample stubs are loaded into the SEM (Sorby Centre, FEI Inspect F) and imaged under vacuum at 3 kV with a spot size of 3. Low acceleration voltage was required to avoid damaging the samples. Magnifications of 1,000x and 10,000x were used.

2.3.2. Differential scanning calorimetry (DSC)

Differential scanning calorimetry (DSC) is a thermoanalytical technique that evaluates the change in a material's heat capacity (Cp) as a function of the temperature (T). The sample's Cp is compared to that of a reference chamber. This can give information about the material such as glass transition temperature and changes in phases such as melting point.

In this case, approximately 3 mg of degummed SF fibres were placed in an aluminium pan and tightly closed. The pan was, then, placed in a DSC4000 (PerkinElmer, United Kingdom) and subjected to a temperature profile that can include different steps such as heating, cooling, and constant temperature. This is done under nitrogen atmosphere with a gas flow of 20 mL/min. An optimisation of these steps was carried out to find the profile that gave more relevant information. A baseline for each profile is needed for post-processing calculations, this is achieved by running the same temperature profile with an empty aluminium pan.

2.3.3. Thermal gravimetric analysis (TGA)

Thermal gravimetric analysis (TGA) is a thermoanalytical technique that evaluates the change in a material's mass as a function of the temperature (T) with a constant heating rate. This measurement can give information about the transitions and phase changes of a sample, as well as chemical information such as decomposition or reactions.

Briefly, approximately 3 mg of degummed SF fibres were placed in a pre-zeroed chamber inside of a Pyris 1 TGA Thermogravimetric Analyzer (PerkinElmer, United Kingdom) and heated to a maximum of 1000°C with a heating rate of 10°C/min under a flow of N_2 gas (20 mL/min).

2.4. Characterisation of RSF solution

2.4.1. Sodium Dodecyl Sulphate Polyacrylamide Gel electrophoresis (SDS-PAGE)

SDS-PAGE was carried out with samples of RSF prepared using different degumming times (30 or 90 min and dried in the oven at 60°C), dissolved using Ajisawa's method and dialysed using different MWCO (3.5, 10 or 12 kD). Precast gels of 10% Tris-glycine were used and loaded with 10 µg of denatured proteins. Separation was carried out under constant electric current of 20 mA during 30 min. Separated protein bands were stained with Colloidal Coomassie blue so they can be detected.

2.5. Dissolution of amphiphilic peptide

The synthetic peptide Ac-I_3K-NH_2 (purity >98% w/w), named I_3K, was purchased from GL Biochem Ltd. (Shanghai, China) as a lyophilised powder. On the other hand, an aqueous buffer solution is prepared by dissolving HEPES (N-2-hydroxyethylpiperazine-N-2-ethane sulfonic acid) in deionised water with a final concentration of 20 mM. The pH is adjusted to 6.0 using a 1 M solution of NaOH (sodium hydroxide) or HCl (hydrochloric acid) as needed. This is then filtered sterile and stored at 4°C for up to 1 month.

Finally, I_3K peptide is dissolved in the HEPES (20 mM, pH 6.0) solution at a concentration of 5 mg/mL. Because solubility is low due to the bigger hydrophobic block of the peptide, the dissolution process is carried out with the help of an ultrasonicator bath. Once all the peptide was dissolved, the pH was checked and adjusted back to 6.0 if needed with the help of 1 M solution of NaOH or HCl. I_3K solution was then incubated under ambient conditions for the required amount of time, i.e., 0, 1, 3, 5 and 7 days before using.

2.6. Preparation of spin coated samples

Samples for cell culture, atomic force microscopy (AFM) and as substrate for inkjet printing were prepared by spin coating. RSF monolayer samples or RSF:I_3K bilayer samples were spin coated (WS-650-23NPP, Laurell Technologies Corporation, USA) onto 13 mm round cover glasses with a thickness of 1.5 mm (Avantor VWR, UK) for cell culture and AFM or onto 10x10 mm square cover glasses 1.5 mm thickness (Agar Scientific, UK) for inkjet printing and subsequent cell culture.

Briefly, to make the RSF monolayer samples, a solution of 70% ethanol (300 µL) was spun first to clean the surface at 8,000 rpm for 20 seconds. Then, the RSF solution (40 mg/mL) is spun at 8,000 rpm for another 20 seconds and lastly, a 95% ethanol solution is spun at 4,000 rpm for 20 seconds to change the conformation of the SF from silk I (random coil, soluble state in the RSF solution) to silk II (β-sheet, insoluble state). On the other hand, to prepare the RSF:I_3K bilayer sample, an additional step is needed, 50 µL of I_3K solution (5 mg/mL, left to self-assemble for 0, 1, 3, 5 or 7 days under ambient conditions) are spun on top of the RSF monolayer.

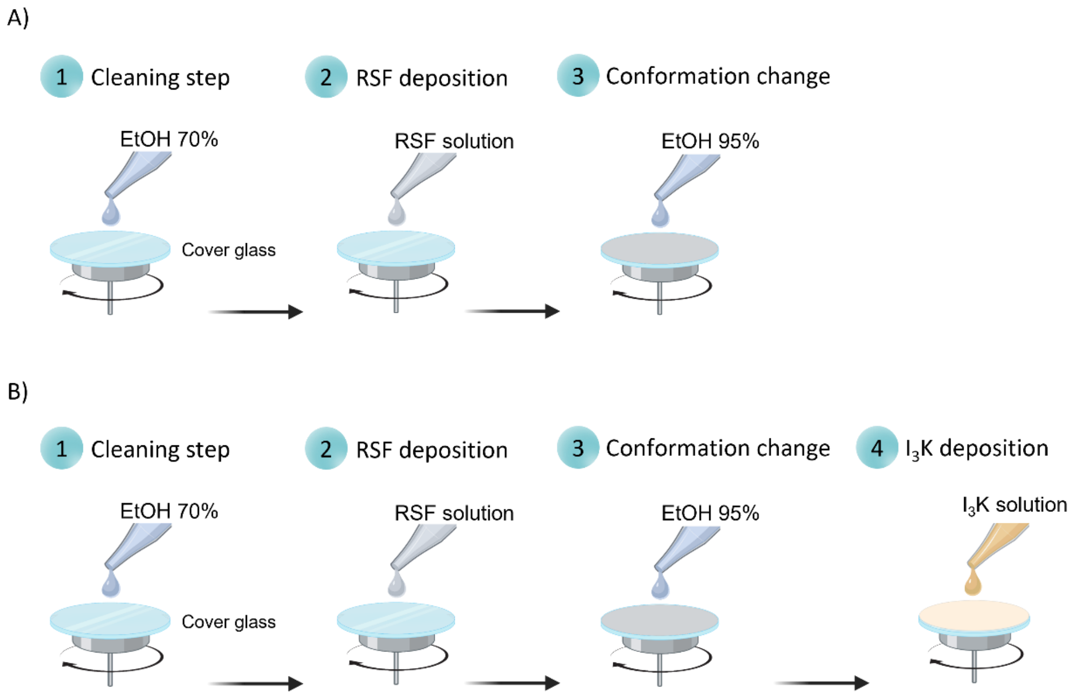

Figure 11. Schematic of the preparation of A) RSF monolayer samples and B) RSF:I_3K bilayer samples. Created with BioRender [93].

2.7. Characterisation of spin coated samples

2.7.1. Atomic Force Microscopy (AFM)

AFM was carried out using a Bruker Dimension Icon instrument to characterise the topography of the samples with SCANASYST-AIR probes at room temperature. Samples were prepared by spin coating as mentioned above and the cover glass was stuck to an AFM support disc. Tapping mode was used to scan the samples and Brucker NanoScope Analysis software (Version2.0) was used for analysis.

2.7.2. Contact angle

The water contact angle was measured using a Krüss GmbH drop shape analyzer-100 (DSA100), this is equipped with a 20-gauge blunt syringe to place 5 µL of deionised water on top of the surface of the sample. Then, the contact angle is calculated by the DSA100 software using the sessile drop method.

2.8. Micropatterning via inkjet printing

Micropatterning of the RSF surfaces, previously prepared by spin coating as explained above, was carried out via drop-on-demand (DoD) inkjet printing. A custom-built inkjet printer equipped with 40 µm nozzle piezoelectric jetting devices (MicroFab Technologies Inc., USA). When a voltage differential is applied to the piezoelectric actuator that surrounds a glass capillary, it produces a pressure wave in the fluid causing a droplet to be jetted [98]. An example of this can be seen in Figure 12, a droplet is formed and ejected to be deposited in the printing surfaces creating the pattern. The droplet formation can also be seen in Figure 13D. A custom-made software is used to control the voltage pulse applied and to move the printing stand, it also controls the number of droplets that can be generated and its spatial position. This program was made on the LabView platform (National Instruments Corporation, USA) (Figure 13B). The micropatterning spatial positions are determined as X-Y-Z coordinates in Microsoft Excel and then read by the software [99-103].

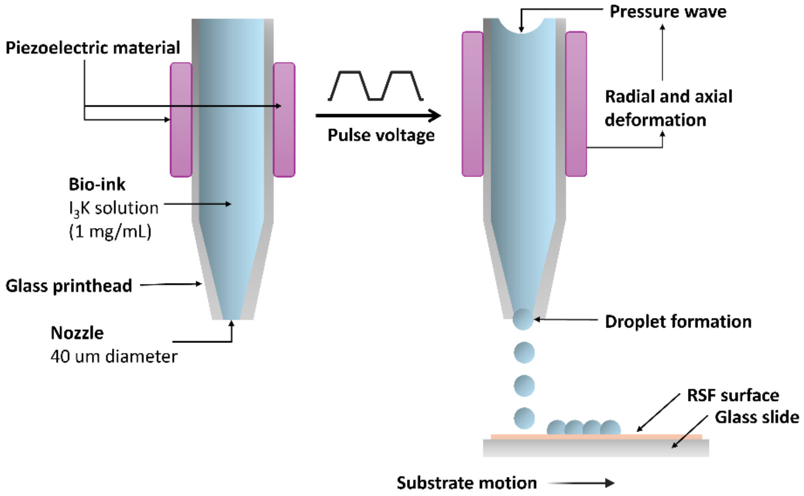

Figure 12. Schematic of the micropatterning of I_3K solution on RSF surfaces via inkjet printing.

Briefly, previously spin coated cover glasses with RSF (as mentioned before) are used as a substrate for inkjet printing. The bio-ink is made of I_3K solution diluted to 0.5 mg/mL using 20 mM HEPES buffer solution with a pH of 6. This bio-ink was left to self-assemble for 3 days at room temperature prior being used for printing. An optimisation step of the voltage waveform was done so the smaller stable droplet can be obtained. Then, the micropattern was printed with different number of layers, i.e., 1, 3 or 5 layers. The distance between the nozzle and the RSF substrate was approximately 2 mm.

2.9. In vitro studies with PC12-Adh neuronal-like cell line

2.9.1 General cell culture

A PC12-Adh neuronal cell line (rat pheochromocytoma, cancerous, ATCC, USA) was used as an *in vitro* model for neuronal cells.

These cells are considered an immortalised cell line since they have been mutated to evade cellular senescence and are able to keep undergoing cell division indefinitely. However, this does not mean that the same cells can be used for cell culture forever, each time that cells reach 80-90% confluence in a flask, cells need to be divided in different flasks to be able to keep growing. This is known as a subculture, and the number of times this step has been done is called a passage. Sometimes the number of passages, or “how old the cells are”, can affect the results of the experiment. As a result, the number of passages is decided prior to experiments. For this study, all cells were between passage 4 and 8 (P4-P8).

General culture medium is prepared adding 1% glutamine, 0.5% amphotericin B, 1% penicillin/streptomycin and 10% foetal calf serum (FCS) to Dulbecco's Modified Eagle Medium (DMEM).

PC12-Adh were kindly given by the tissue engineering and biomaterials group at the University of Sheffield. Cells are grown in a T75 flask in growth media in a humidified atmosphere with 5% CO_2 at 37°C. After reaching 80% -90% confluent in the T75 flask, cells were used for experiments or split for continuous growth.

2.9.2. Cell attachment assay: crystal violet

When PC12-Adh cells reached 80-90% confluency, cells were dissociated with 5 mL of trypsin-ethylenediaminetetraacetic acid (Trypsin /EDTA) for 3-5 min, obtaining a monodisperse solution of cells. The concentration of cells is calculated manually with the help of a haemocytometer and then, 64 $\times 10^4$ cells were seeded on top of the RSF samples, controls (TCP+, TCP- and cover glass) or RSF:I_3K samples, depending on the experiment, previously sterilised under UV for 30 min. These cells were kept for 24 h in a humidified atmosphere with

5% CO_2 at 37°C. After that, cells were washed with PBS (phosphate buffer saline). Apoptosis was induced in the negative control by incubating for 10 min in 1% Triton X-100. Then, cells were fixed for 10 min using a 3.7% FA (formaldehyde) solution, immediately after that they were wash again with PBS. Then, 250 µL of crystal violet in 70% ethanol and incubate for 10 min. Crystal violet solution was removed and samples were washed 3 times with 1 mL PBS to remove unbound crystal violet. Then, 600 µL of acetic acid was used per sample to redissolve the bound crystal violet, 100 µL of this was transferred in triplicate to a 96-well plate and the absorbance at 630 nm was read using a plate reader.

2.9.3. Metabolic activity assay: resazurin assay

Resazurin solution was made from resazurin powder dissolved in PBS at a concentration of 1 mM and was sterilised by filtration. This can be stored protected with aluminium foil at 4°C until use for no more than 1 month. Then, the stock is diluted to prepare a 10% resazurin solution in full DMEM media.

Direct method

Similarly, after cells growing in the T-75 reached 80-90% confluency, they were trypsinized to obtain a monodisperse solution, then counted with a haemocytometer. Then 32 $\times 10^4$ cells were seeded on top of the RSF samples, controls (TCP+, TCP- and cover glass) or RSF:I_3K samples, depending on the experiment, previously sterilised under UV for 30 min. Cells were left to grow and expand for 24 h at 37°C in a humidified atmosphere with 5% CO_2. At this point, cells in the negative control (TCP-) were killed in 1% Triton X-100 for 10 min. Then, all samples were incubated for 24 h more. After a total of 48 h, old media was removed and 500 µL of resazurin solution in fresh media was added to each well. Plates were wrapped in aluminium foil to protect the solution from light and incubate for 4 h at 37°C in a humidified atmosphere with 5% CO_2. Then, from each well 100 µL were transferred in triplicate to a 96-well plate and fluorescence intensity was obtained using a plate reader ($\lambda_{Ex}/\lambda_{Em}$ of 530-560/590 nm).

Indirect method

For the indirect method, PC12-Adh were all seeded in TCP with 32 x 10^4 cells, while samples were submerged in growth media. All were incubated for 24 h at 37°C in a humidified atmosphere with 5% CO_2. After this, cells in negative control (TCP-) were induced apoptosis with 1% Triton X-100 for 10 min, and media used to submerge each sample was transferred to its equivalent well with cells. Then, these were incubated 24 h more. The following steps were the same as mentioned in the direct method above.

2.9.4. Differentiation of PC12-Adh

Differentiation of PC12-Adh can be induced by adding a nerve growth factor (NGF, Recombinant Rat beta-NGF Protein, R&D systems). The concentration used for differentiation can vary from 20 ng/mL to 100 ng/mL [104-107]. In this case, NGF is dissolved in full media at 50 ng/mL and cells are incubated for 7 days. Media ± NGF was replaced every 48 h.

2.10. Fluorescence Microscopy and analysis of cells

2.10.1. Fixing and staining of PC12-Adh cells

After PC12-Adh neuronal cells were cultured for the required amount of time. Old culture medium was removed. Then, samples were fixed with 3.7% FA for 10 min and permeabilized with 0.1% Triton X-100 for 10 min at room temperature. Samples were washed with PBS once. Then DAPI (4’,6-diamidino-2-phenylindole) and Phalloidin-FITC (Fluorescein Isothiocyanate (FITC) labelled Phalloidin) were used at a 1:1000 dilution in PBS to stain the nuclei and the F-actin, respectively. Samples are incubated for 1 h in the staining solution protected from the light. Then, this solution is removed and washed with PBS. Finally, samples are kept submerged in PBS ready to be imaged.

2.10.2. Fixing and immunolabeling of PC12-Adh cells for βIII tubulin

After PC12-Adh neuronal cells were cultured for the required amount of time. Immunolabeling of β-III tubulin was carried out to identify differentiated cells. After discarding culture media, cells were fixed in 3.7% FA for 10 minutes at room temperature. Then, FA was discarded, and cells were permeabilised with 0.1% Triton X-100 for 10 minutes at room temperature. This will allow the antibodies to have better access to the inside of the cells, resulting in higher immunofluorescence intensity. Then, cells were blocked using either a 3% bovine serum albumin (BSA) or 3% horse serum (HS) solution in PBS for 1 hour at room temperature. This is an essential step to reduce nonspecific binding of the antibodies and improve image quality. This solution was discarded, and samples were washed with PBS. Then, the primary antibody, mouse anti-βIII-Tubulin mAb (Promega, UK), was dissolved in either a 1% BSA or 1% HS solution in PBS with a 1:1000 dilution factor. This was added to the samples and incubated overnight at 4°C. The following day, the solution with the primary antibody is removed and samples are washed with PBS once. Then, the secondary antibody, Texas Red conjugated horse anti-mouse IgG was dissolved in either 1% BSA or 1% HS with a 1:250 dilution. This was added to the samples and incubated for 4 hours at room temperature and protected from the light. Samples were then washed once with PBS. Finally, a solution with DAPI (1:1000) and FITC-phalloidin (1:1000) in PBS was added to the samples and incubated for 1 hour so the nuclei and the F-actin can be stained. This solution was then discarded, samples were washed with PBS once and stored submerged in PBS at 4°C until imaging.

2.10.3. Epifluorescence microscopy

Images were obtained by using an Inverted Olympus IX73 epifluorescent microscope combined with the software Micro-Manager (University of California, USA). The following wavelengths were used: $\lambda_{ex}/\lambda_{em}$ 405/450 nm for DAPI, $\lambda_{ex}/\lambda_{em}$ 496/516 nm for Phalloidin-FITC and $\lambda_{ex}/\lambda_{em}$ 595/615 nm for Texas Red (sulforhodamine 101). Three images of each condition were taken and analysed with ImageJ 1.53t (National Institutes of Health, USA).

2.11. Statistical analysis

Data were presented as mean ± standard deviation (N = 3 or otherwise mentioned). One-way or two-way factor analysis of variance (ANOVA) was performed for all multiple group experiments. P values of $*P < 0.05$, $**P < 0.01$, $***P < 0.001$ and $****P < 0.0001$ were considered as significant. The statistical analysis was performed using Prism GraphPad software. Equality was confirmed by Tukey's multiple comparison test.

2.12. Acknowledgments

All AFM scans and part of the SEM images were carried out by Dr David Alexander Gregory, University of Sheffield. Gel electrophoresis was carried out with help from Dr Caroline Evans, University of Sheffield. DSC and TGA scans were carried out partially with the help of technicians at the Basic Characterisation laboratory, Royce Centre, University of Sheffield.

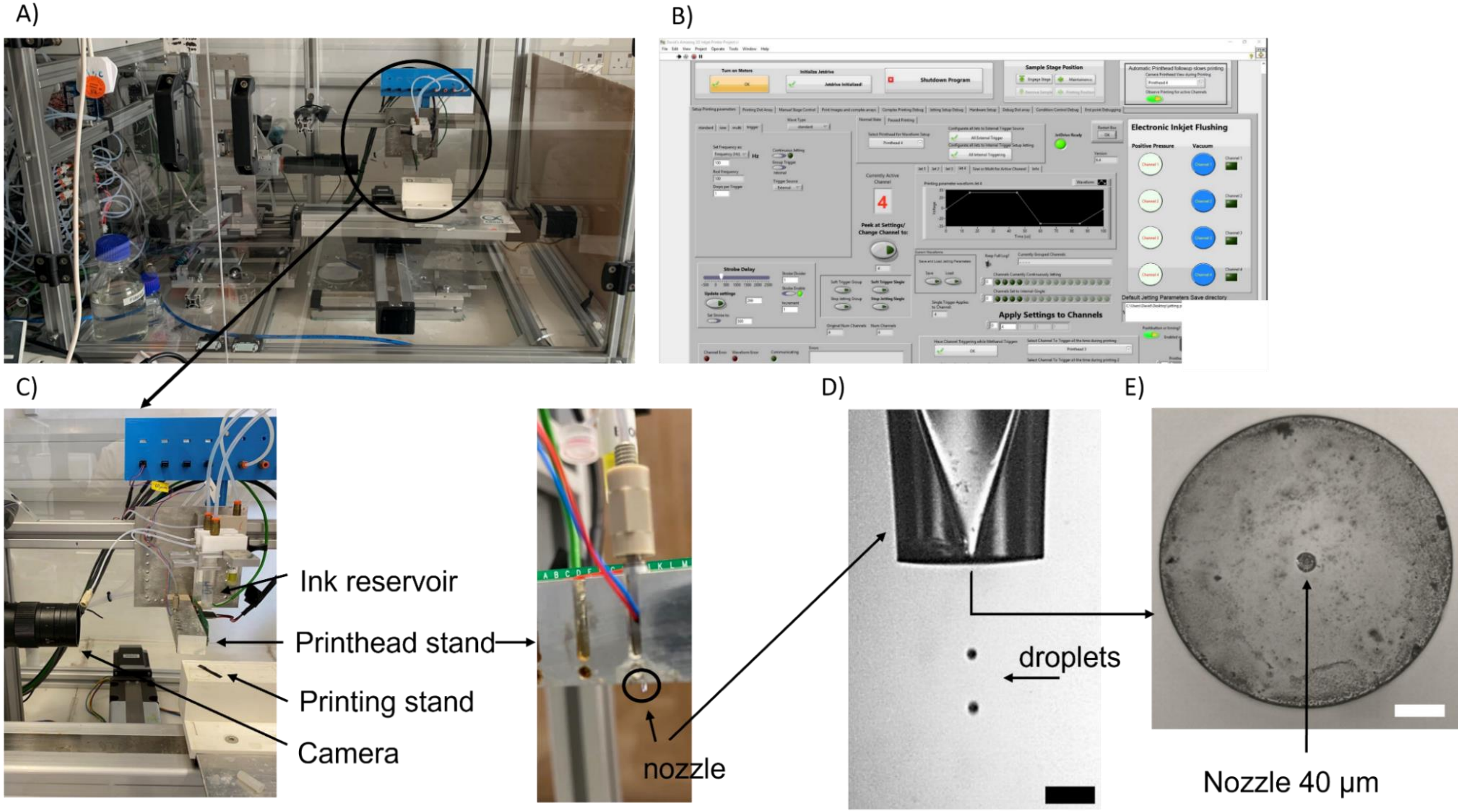

Figure 13. Images of A) inkjet printer, B) printer software, C) zoom of the printing area of the inkjet printer, including a close-up image of the printhead stand, D) stroboscopic image of the nozzle taken from the printer camera while printing, scale bar is 200 µm, and E) microscope image of the nozzle of the printhead, scale bar is 100 µm.

Chapter 3. Effects of silk processing on cell attachment and proliferation

3.1. Introduction

Silk fibroin biomaterials have been used for a long time in biomedical applications. Their first use was as sutures but more recently, other applications have also been studied such as in tissue engineering scaffolds. Regenerated silk fibroin (RSF) is very versatile and can be processed into different morphologies such as sponges, spun fibres and hydrogels [12]. Silk is a natural material composed of two main proteins: sericin and fibroin. However, successful removal of the sericin protein is crucial to obtain a pure silk fibroin material and to avoid immunological responses [14, 15]. Moreover, successful dissolution of the SF fibres is important for its subsequent processing into different biomaterials such as hydrogels, fibres or films as highlighted in section 1.1.3.

3.1.1 Influence of removal of sericin protein on silk fibroin properties

This removal can be achieved by different methods or agents such as alkali, acid, high pressure, and enzymes [94-96]. There have been previous studies about how the degumming process can affect the properties of the regenerated silk fibroin [108-110]. For example, Kim et al. [108] investigated how five different methods of degumming such as the urea method, high temperature high pressure (HTHP) method, citric acid method, sodium oleate/sodium carbonate mix method and sodium carbonate method affected the final properties of the RSF. They concluded that both the degumming method strongly affected the mechanical properties, molecular weight (MW) and viscosity of the RSF solution and RSF films and although the sodium carbonate solution is the most widely used, other methods can be equally suitable to remove sericin and improve the RSF properties. On the other hand, Wang et.al [110], also compared the sodium carbonate and urea methods for degumming and how this affected the formation of SF nanoparticles.

Although viability and cytocompatibility of different degumming methods have been previously studied [111, 112]. The correlation between one degumming method and cell attachment in the final RSF material has not been properly investigated previously. RSF is a cytocompatible material widely used in tissue engineering. However, there are reports about its low bioactivity and overall poor cell attachment [2, 27]. The addition of other materials such as laminin [46], fibronectin [27], collagen [47] or peptides [49] are needed to improve cell adhesion and proliferation on RSF materials.

3.1.2. Influence of silk fibroin dissolution and alcohol treatment on silk fibroin properties

SF fibres obtained after the degumming process have a high molecular weight and they are usually difficult to dissolve. Lithium bromide (LiBr) solution (9.3 M) [51] or Ajisawa's ternary reagent [52] are the most commonly used solvents to obtain a RSF solution.

Molecular weight and protein structure of the RSF solution can vary based on the dissolution method used affecting the mechanical properties, biodegradability and biocompatibility of the final RSF material [43, 113-116]. For example, Zhang et al. [116] compared the biocompatibility and effect on proliferation of mouse embryonic fibroblasts from SF films prepared by LiBr or Ajisawa's solvent, showing that LiBr had the best biocompatibility. Another study, carried out by Aznar-Cervantes et al. [115] showed that there are different levels of degradation in RSF obtained by different solvents and this affected the properties of the electrospun mats.

On the other hand, Cheng et al. [117] showed that while traditionally LiBr has been mostly used to obtain RSF materials, the use of Ajisawa's ternary reagent did not cause significant differences in morphology and amino acid composition of the RSF. However, small amounts of residual calcium, main component of Ajisawa's ternary reagent, can still be found even after extensive dialysis. Nevertheless, this did not seem to affect biocompatibility of the RSF. The use of LiBr has many disadvantages such as cost, toxicity and it is overall, environmentally unfriendly. The use of Ajisawa's ternary reagent is a cost-effective and environmentally friendly alternative for silk solubilisation that shows no difference in the final RSF material [117].

After the dissolution process, RSF are converted into multitude of different biomaterials, ranging from films to electrospun and hydrogels. However, untreated RSF biomaterials show a high percentage of amorphous structures that causes the material to be water soluble and limits its applications in that state. This is also known as silk I structure and it is mainly formed of random coils and α-helix [1]. To increase the crystalline structure within these RSF materials, several methods can be used such as heat or mechanical strain, but also treatment with solvents such as methanol or ethanol [118-121]. This causes the conformational change from random coils and α-helix into β-sheets (also known as silk II), increasing crystallinity in the RSF material and decreasing its water solubility. Controlling the amount of β-sheets allows the tuning of the RSF properties including cell-adhesion.

For example, Li at al. [118] studied the conformation change of silk from α-helix and random coils into β-sheets using aqueous ethanol, and concluded that a 40-60% (w/w) ethanol solution was the most effective. However, the relation between this and its properties as biomaterial were not studied.

On the other hand, Terada et al. [120] investigated the effect of ethanol concentration on the surface properties of SF films. They concluded that if the SF was treated with <80% ethanol, the material resulted in a hydrated surface where fibroblast preferred to aggregate rather than individually attach and elongate. On the other hand, treatment with >90% ethanol promoted individual cells to adhere to the surface and obtain an elongated morphology which is characteristic of fibroblasts.

Moreover, treatment with ethanol can also affect other properties of RSF materials such as mechanical and optical properties. Kaewpirom et al. [122] studied how alcohol treated RSF films exhibited different levels of optical transparency and how this was related to the total content of β-sheets. Moreover, alcohol treated films had a higher tensile strength and Young's modulus with a lower strain at break than untreated RSF films.

3.2. Aims and objectives

This chapter explores how sodium carbonate as a degumming agent can affect the biological properties of RSF surfaces. Silk cocoons are degummed using the same degumming ratio but changing the degumming time. The RS fibres obtained are then dried in two different ways to assess the importance of this step. In addition, the SF fibres are all dissolved via the Ajisawa's method and dialysed using three different molecular weight cut-offs (MWCO) to obtain different RSF solutions. Finally, these RSF solutions are then spun coated on a cover glass to create a highly reproducible thin layer that can be used as a surface to assess cell attachment and biocompatibility.

The aims of this chapter were:

1. Fabrication and characterisation of SF fibres obtained from different degumming times after drying at room temperature or at 60°C.
2. Fabrication of RSF coated cover glasses after dissolution of the different SF fibres using Ajiwasa's method.
3. Assess the cell attachment and cytocompatibility of the different RSF surfaces

The objectives of this chapter were:

1. Degumming the silk cocoons with a Na_2CO_3 solution for three different times, e.g., 30, 60 and 90 min. Dry the obtained SF fibres at room temperature or at 60°C.
2. Verify that the removal of sericin via degumming has been complete via weight loss and scanning electron microscopy.
3. Dissolve the SF fibres via Ajisawa's method and dialysed the RSF solution using three MWCO dialysis tubes.
4. Spin coating the different RSF solution onto cover glasses.
5. Assessment of cell attachment on those surfaces via crystal violet assay
6. Direct and indirect assessment of cytocompatibility via resazurin-resorufin assay.
7. Imaging and assessment cell morphology via fluorescent staining

3.3. Materials and methods

3.3.1. Materials

Details of the materials used were described in Chapter 2 Section 2.1.

3.3.2. Silk degumming and characterisation of SF fibres

The silk degumming process was described in Chapter 2 Section 2.2.1. Degumming times used were 30, 60 and 90 min, then SF fibres were either air-dried at room temperature or oven-dried at 60°C.

Weight loss due to degumming

Details to calculate the weight loss were described in Chapter 2 Section 2.2.2.

SEM

The SEM analysis was described in Chapter 2 Section 2.3.1.

DSC

The SEM analysis was described in Chapter 2 Section 2.3.2.

TGA

The SEM analysis was described in Chapter 2 Section 2.3.3.

3.3.3. Dissolution of silk fibroin to obtain regenerated silk fibroin solution (RSF)

The dissolution of SF fibres via Ajisawa’s method was described in Chapter 2 Section 2.2.3, dialysis process was described in Chapter 2 Section 2.2.4 and the final centrifugation and calculation of RSF concentration was described in Chapter 2 Section 2.2.5.

3.3.4. Preparation of RSF surfaces

Spin coating

The spin coating process was described in Chapter 2 Section 2.8. RSF solution was diluted to a concentration of 40 mg/mL.

3.3.5. *In vitro* studies with PC12-Adh neuronal-like cell line

General cell culture

General cell culture procedure as well as general culture media preparation were described in Chapter 2 Section 2.5.1.

Cell attachment assay: crystal violet

Crystal violet assay was described in Chapter 2 Section 2.5.2.

Metabolic activity assay: resazurin assay

Metabolic activity assay carried out directly or indirectly was described in Chapter 2 Section 2.5.3.

3.3.6. Fluorescence Microscopy and analysis of cells

Staining and fluorescence imaging procedures were described in Chapter 2 Section 2.6.1. and Chapter 2 Section 2.6.3.

3.3.7. Statistical analysis

Data were presented as mean ± standard deviation (N = 3 or otherwise mentioned). One-way or two-way factor analysis of variance (ANOVA) was performed for all multiple group experiments. P values of $^{*}P < 0.05$, $^{**}P < 0.01$, $^{***}P < 0.001$ and $^{****}P < 0.0001$ were considered as significant. The statistical analysis was performed using Prism GraphPad software. Equality was confirmed by Tukey's multiple comparison test.

3.4. Results and Discussion

3.4.1. Silk degumming and characterisation of SF fibres

Weight loss due to degumming

As described before in Chapter 1 Section 1.1.1., silk from *B. mori* is composed of two different proteins: sericin and fibroin. To be able to use the SF in tissue engineering applications, the SS needs to be removed. Removal of SS, also called degumming, can be achieved by different methods or agents. These include agents such as alkali, acid, high pressure, or enzymes [94, 95]. However, the more commonly used degumming agent is Na_2CO_3 due to its effectiveness and low cost. The carbonate hydrolyses the peptide bond of the SS protein chain releasing it to the solution where it is highly soluble [123]. Dou et al. [123] investigated the effect of sodium carbonate concentration on the degumming and regeneration process of SF. They concluded that the concentration of the carbonate highly affected the molecular weight, rheology, physical and mechanical products of the RSF, and therefore, it can be used to tune the final RSF material for different applications.

Here, the silk cocoons were degummed using a 0.02 M Na_2CO_3 solution for 30 min, 60 min and 90 min. Then, the obtained SF fibres were either dried at room temperature or in a temperature-controlled oven set to 60°C. The results can be seen in Figure 14 where the weight loss is on average 30.7% ± 0.6 and there is no significant difference between any of the groups. These results suggest that a weight loss of around 30% is enough to conclude that the degumming process has been completed. However, the weight loss might be related to loss of SF that has been degraded and lost during the same process and, therefore, further analysis is needed to corroborate these results.

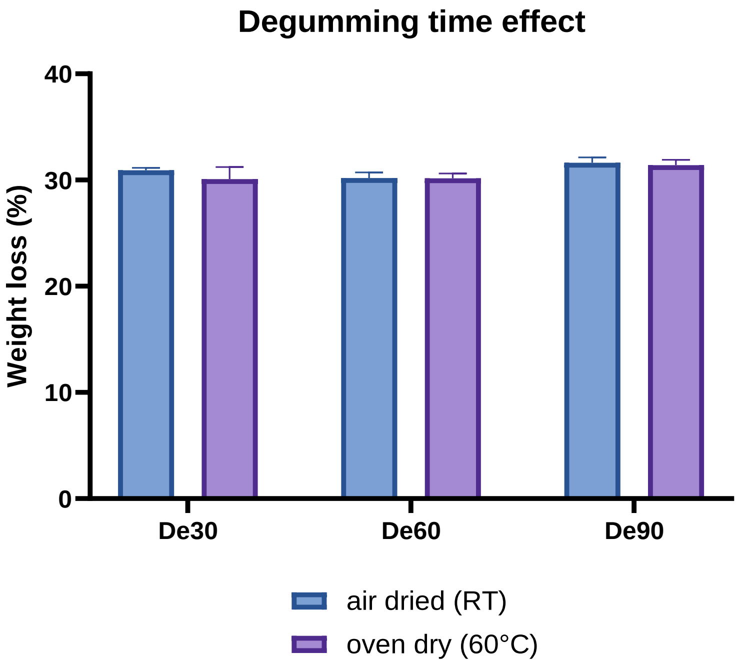

Figure 14. Effect of degumming time (30, 60 and 90 min) and drying method (air dry or oven dry) on weight loss. All degumming was carried out with a 0.02 M Na_2C0_3 solution. N=3 in every group. Error bars represent the standard deviation. Two-way factor analysis of variance (ANOVA) was performed. P values of *P < 0.05, **P < 0.01, ***P < 0.001 and ****P < 0.0001 were considered as significant.

SEM

As discussed before, the weight loss alone fails to provide sufficient evidence to prove the completion of the degumming process. Therefore, a different type of analysis is needed to corroborate the removal of sericin.

Raw silk fibres have a specific hierarchical structure as proposed before by Wang et al. [124]. One raw silk fibre is composed of two SF strands that are coated and glued together by a SS coating as can be seen in Figure 15A. This structure can be further seen using scanning electron microscopy (SEM) as seen in Figure 15B. In this SEM image, silk strands are woven to produce layers of the silk cocoon. In Figure 15C, the SS coating can be seen wrapping the SF fibres with a soft texture and joining two SF to form the proposed hierarchical structure shown in Figure 15A. Because SS can be clearly observed in these SEM images, the lack of it in the individual SF fibres obtained with different degumming times can provide an insight into the success of the degumming process.

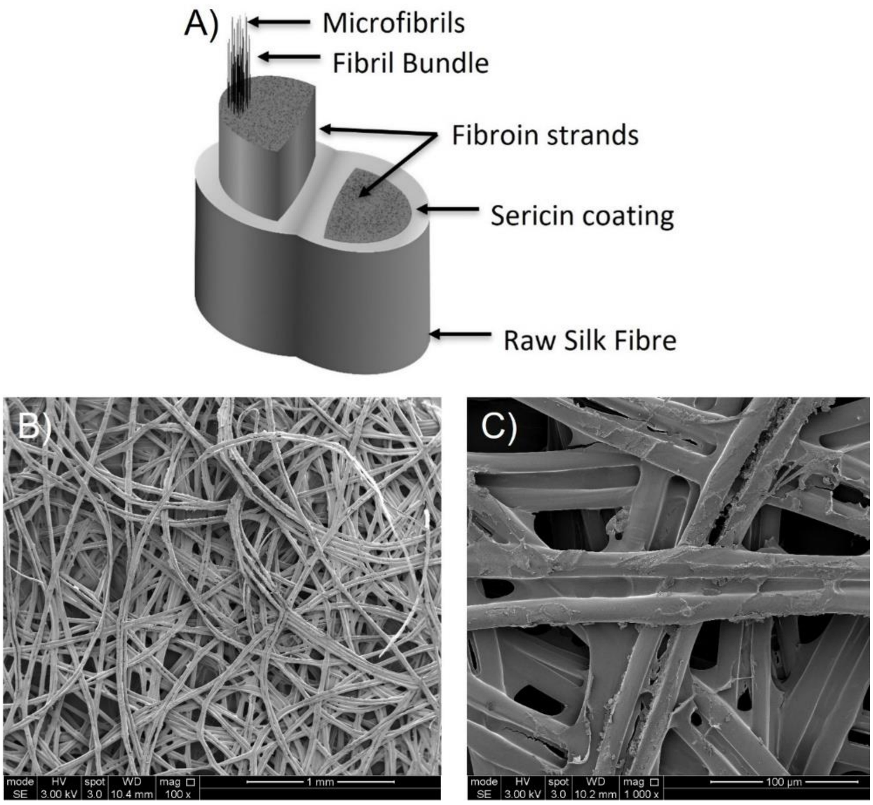

Figure 15. A) Proposed hierarchical structure of raw silk fibres from *B. mori* cocoons. Reproduced from the work of Wang, Q., et al. [124]. B) SEM image of a layer of raw silk cocoon from *B. mori*. Magnification is 100x and the scale bar represents 1 mm. C) SEM image of a layer of raw silk cocoon from *B. mori*. Magnification is 1,000x and the scale bar represents 100 µm.

Figure 16 B1 and B2 show images of SF fibres obtained after 30 min of degumming. These show almost complete removal of the sericin coating except for a few remaining residues depicted by white arrows in the figures. Similarly, Figure 16 C1 and C2, corresponding to 60 min of degumming, present traces of the same residue. However, the overall surfaces of all these images (Figure 16 B1, B2, C1, C2) can be considered fully degummed with only traces of sericin coating present.

However, Figure 16 D1 and D2, corresponding to 90 min of degumming, present a very degraded surface where the SF fibril bundles have started to detach from the main body of the SF strand. This is consistent with data found in the literature which shows that the longer the silk cocoons are degummed the more degraded the SF becomes [12].

DSC

To determine if the degumming process has had some effect on the physical properties of the SF fibres, differential scanning calorimetry (DSC) was performed. DSC can give information about the response of a polymer to heating and its thermal transitions (melting point, glass transition, crystallisation, degradation).

Typically, polymers are heated twice during a DSC scan. The first heating ramp shows the thermal history of the polymer up to the melting point. After cooling it down, it is heated a second time to evaluate the inherent properties of the material. However, this two-heating ramp method needs to be optimised for each individual material and evaluate if it is needed.

Figure 17 shows the optimisation of DSC protocol for degummed SF fibres. Here, four different methods have been used in the same sample to see which provided better information. As stated before, usually two heating ramps are needed, first to remove the thermal history and then to see the inherent transitions of the materials. However, proteins can be easily degraded and denatured by heat and Figure 17 shows that the more the SF fibres were heated in the first ramp, less information was obtained in the second ramp. Another observation is that after heating the fibres once, the second ramp does not show the peak around 80 - 90°C. This peak corresponds to a hydration peak, water is bound to the SF fibres and raw silk cocoon naturally and during the degumming process. After the SF is heated once, this water is removed, and the peak does not show in the second heating ramp. Overall, the use of two heating ramps in this case does not provide any additional information and therefore, only one heating ramp was used in the following analysis.

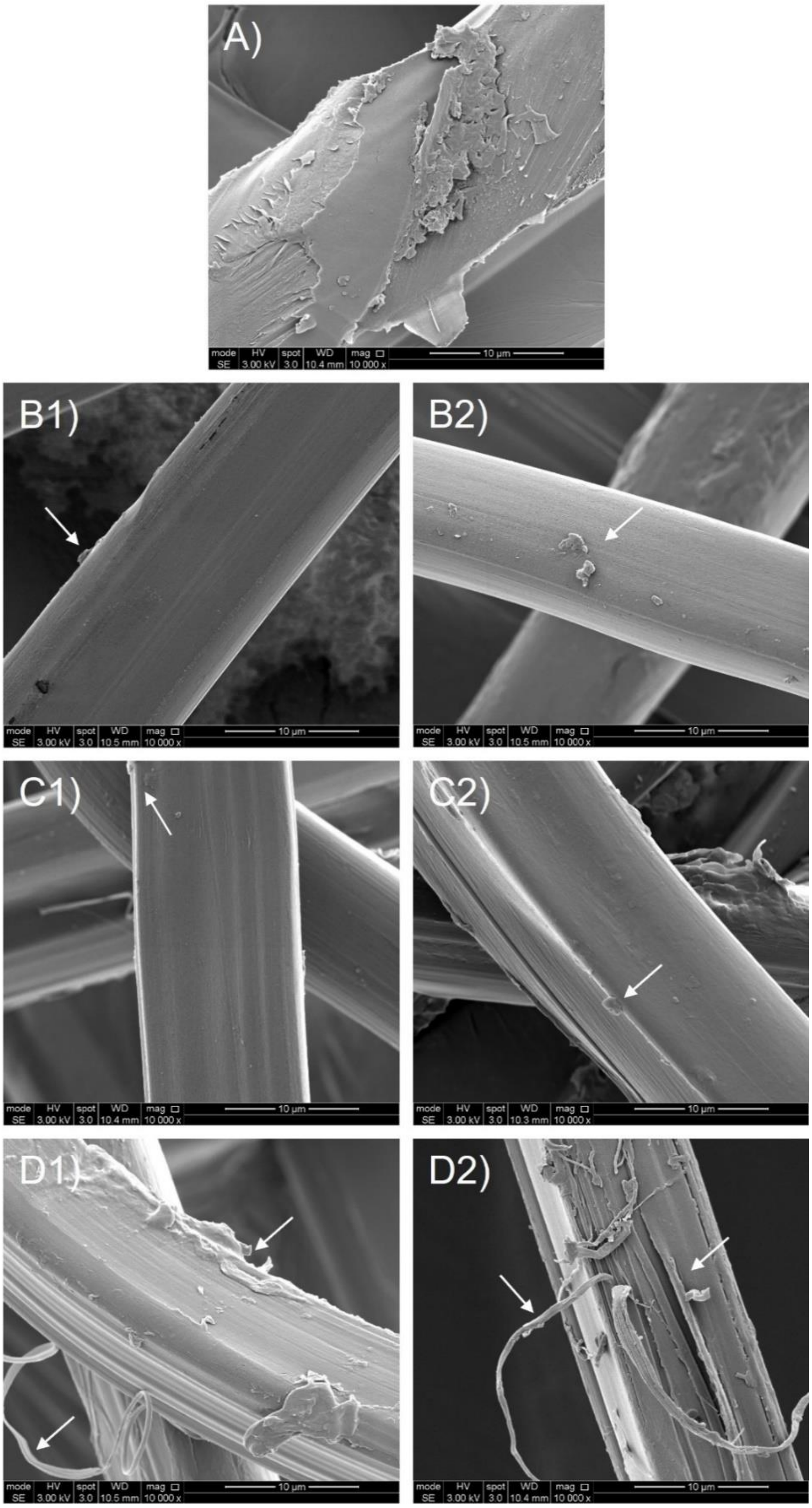

Figure 16. A) SEM image of raw silk strand. B1) SEM image of SF fibre after degumming 30 min, air dry (De30 air dry). B2) SEM image of SF fibre after degumming 30 min, oven dry (De30 oven dry). C1) SEM image of SF fibre after degumming 60 min, air dry (De60 air dry). C2) SEM image of SF fibre after degumming 60 min, oven dry (De60 oven dry). D1) SEM image of SF fibre after degumming 90 min, air dry (De90 air dry). D2) SEM image of SF fibre after degumming 90 min, oven dry (De90 oven dry). Magnification is 10,000x and the scale bar represents 10 µm.

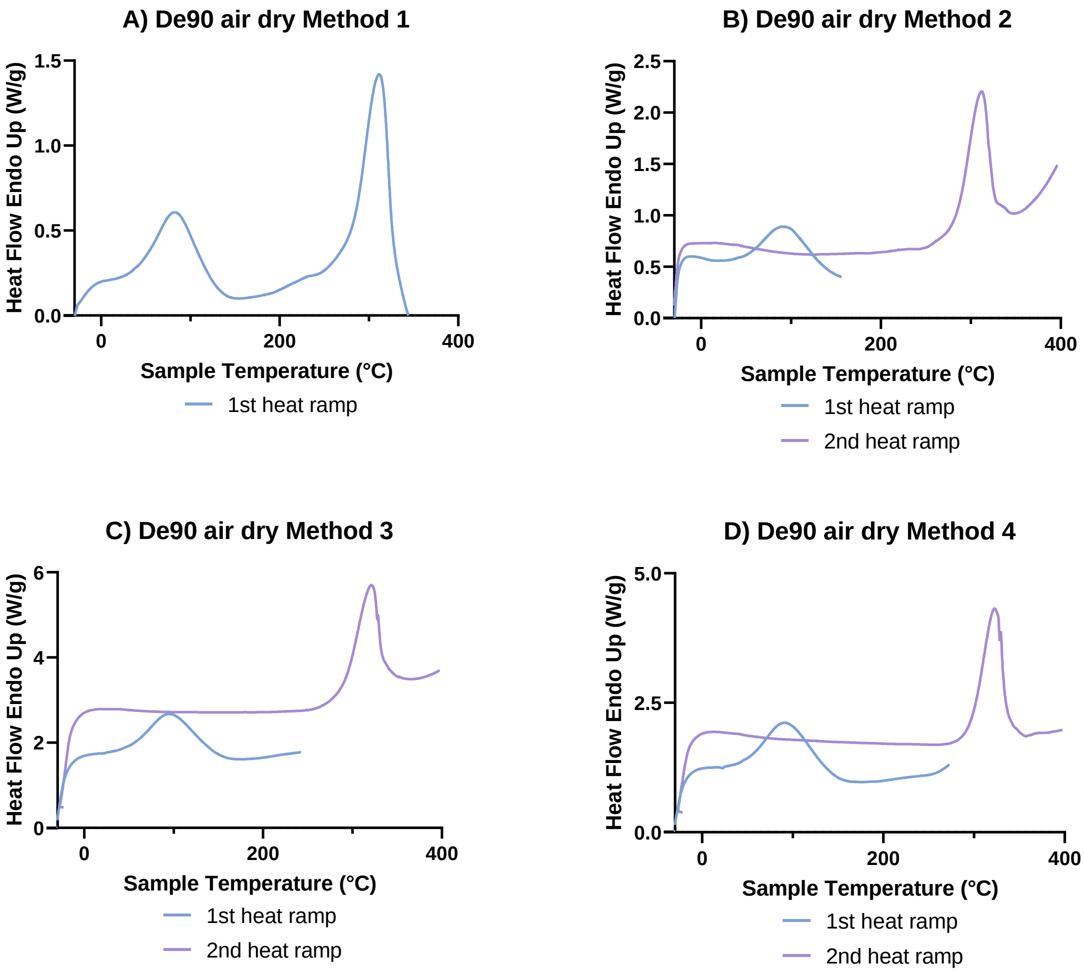

Figure 17. Optimisation of the DSC method used to analyse thermal transitions in degummed silk fibre (De90 air dry). A) Method 1 shows just one ramp from -30°C to 400°C. B) Method 2 shows a first heating ramp from -30°C to 160°C, followed up by a second heating ramp from -30°C to 400°C. C) Method 3 shows a first heating ramp from -30°C to 250°C, followed up by a second heating ramp from -30°C to 400°C. D) Method 4 shows a first heating ramp from -30°C to 280°C, followed up by a second heating ramp from -30°C to 400°C.

The focus of calorimetric analysis in silk materials has been focused on the native liquid state of silk [125, 126] or RSF films [127-131] which are not relevant in this context. Mazzi et al. [132] investigated the thermal behaviour of different silk cocoons and their degummed fibres, including *B. mori*. Figure 18 represents the standard DSC scans for the raw cocoon and all the different degummed fibres. Two endothermic peaks were clearly visible, the first one around 70 - 90°C that corresponded to the water bound to the material, while the second endothermic peak corresponded to the degradation point of the material at around 310°C. Moreover, a shift in the baseline at around 200°C - 240°C indicated a glass transition occurred.

Both peaks and the glass transition were similar to that found in the literature [132]. All values can be seen in Table 3.

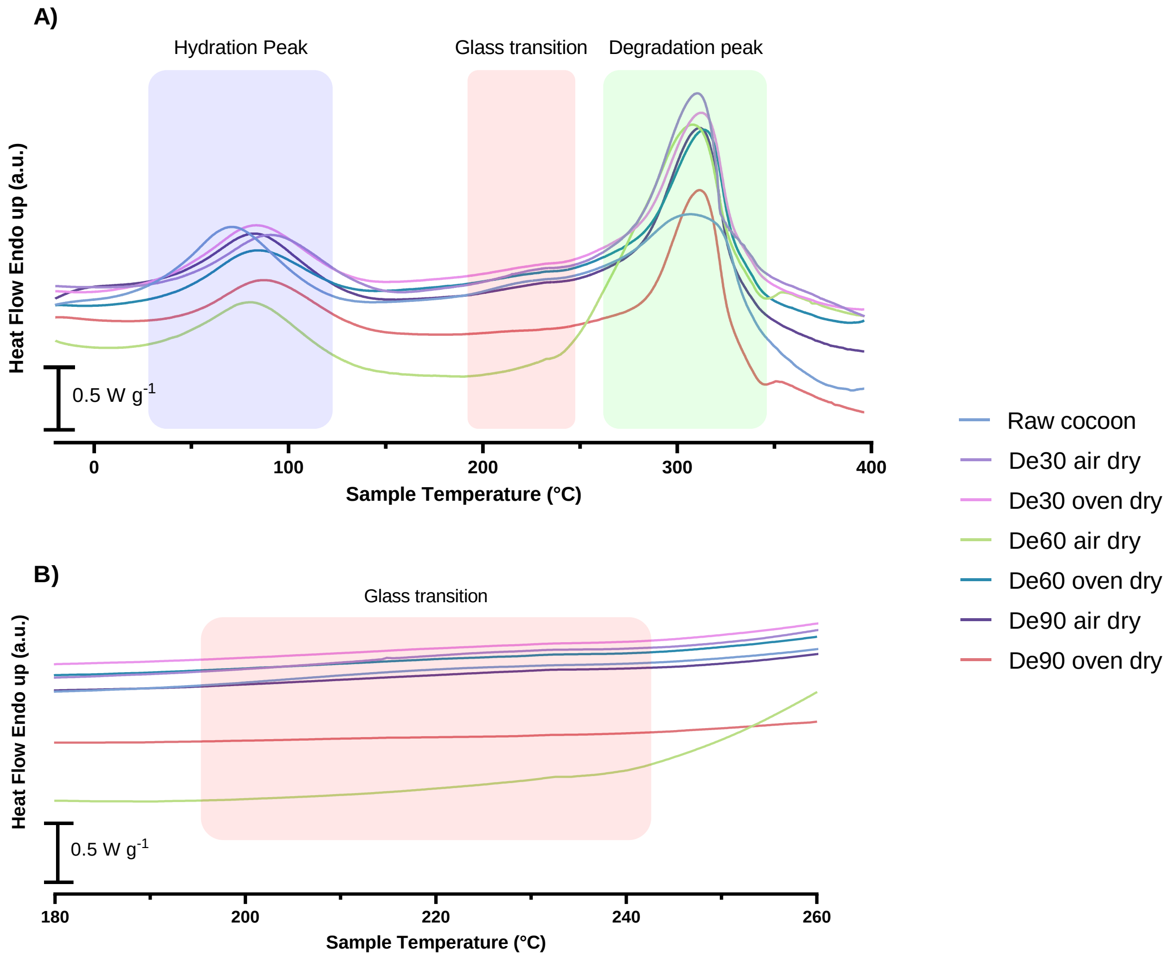

Figure 18. A) Standard DSC scans of *B. mori* raw cocoon and degummed fibre samples. The samples were heated at 10°C min^{-1} from -30°C to 400°C under nitrogen atmosphere with a gas flow of 20 mL/min, with regions related to bound water evaporation shown as blue, glass transition shown red, and degradation shown green. B) Detailed DSC scan of the glass transition region.

Wang et al. [133] studied the the impact of degumming process on the thermal properties of SF. The degradation peak shifted from 329°C when degumming was carried out using 8.0 M urea to 322°C when using Na_2CO_3. This reduced thermal stability is correlated with lower crystallinity and higher protein chain degradation obtained when degumming is carried out with Na_2CO_3 solution.

Although Mazzi et al. [132] only considered one degummed condition, cocoons were boiled in 0.02 M $NaHCO_3$ for 2 hours, they found a water bound peak around 70°C for the raw cocoon which tend to increase for the degummed fibres. In Figure 19, the hydration peak for the raw cocoon was shown to be 71°C while the hydration peak of the degummed fibres increased to 80-90°C. On the other hand, there was no significant difference in the degradation temperature between the raw cocoon and the fibres which ranged from 307°C to 314°C. Mazzi et al. found that the degradation temperature for the raw cocoon was higher than the degummed fibres due to the protective coating of the sericin. However, this coating can be affected by the quantity of sericin present in the raw cocoon which can be affected by the type of silkworm and their diet [134]. Moreover, the temperature at which thermal degradation occurs is also dependent on the content of crystalline β-sheet in the SF fibres. Nultsch et al. [135] observed that there is no relevant change in β-sheet content when different degumming times were used. This can explain why there was no difference in the Td as seen in Figure 19.

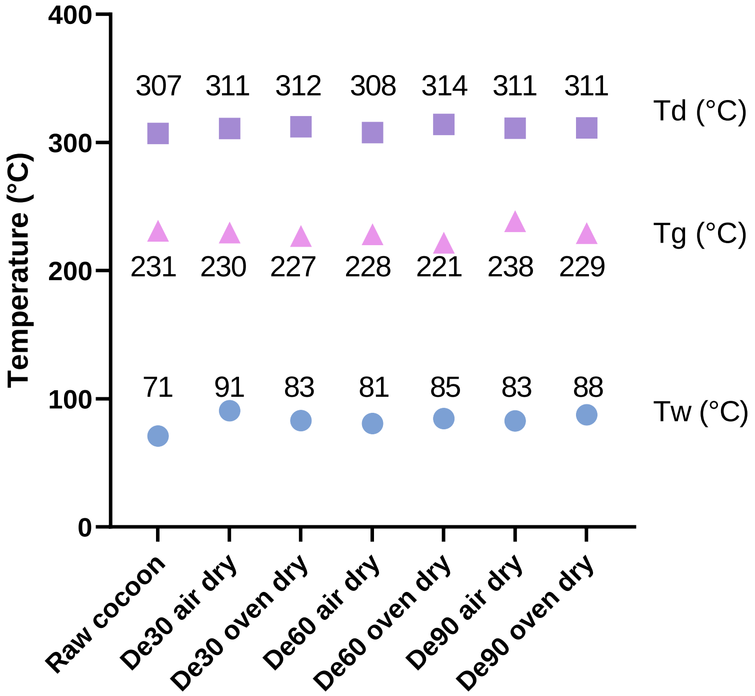

Figure 19. Graphical representation of the temperature of hydration (Tw), glass transition temperature (Tg) and degradation (Td) for the raw cocoon and all the different degummed SF fibres obtained from DSC analysis expressed in °C.

TGA

Similar to DSC analysis, thermogravimetric analysis (TGA) of silk materials has been largely focused on RSF films [130, 131] rather than in the SF fibres obtained after degumming. Therefore, there is limited literature about the thermal behaviour of the SF fibres. However, Mazzi et al. [132] performed thermogravimetric analysis of the raw silk cocoon and its degummed fibres.

TGA can help identify the water bound to the material and its degradation process by showing how the mass changes when the sample is heated. This is a result of thermal degradation or the loss of volatiles, for example. However, in a pure polymer, there is no mass change as a result of the glass transition and therefore, TGA cannot be expected to detect the glass transition temperature (Tg).

On the other hand, Figure 20A shows the percent of mass remaining as the material is heated. During the initial heating from 30°C to 100°C, water bound to the silk was removed as was also demonstrated by the DSC analysis. The water content of the raw silk cocoon was 6 - 7%, while the degummed fibres had a lower content that can range from 4 - 5%. This is consistent with data found in the literature, where Mazzi et al. [132] found that degummed SF fibres from the domesticated *B. mori* were drier than the raw cocoons. Moreover, when comparing the samples that were air-dried to those that were oven-dried at 60°C, there was a higher water content in the air-dried samples, as shown in Table 3.

In addition, Figure 20A shows that above 220°C, the main degradation of the silk started. However, once the temperature reached 950°C only around 24-25% of mass remained. Both the water-bound and the degradation regions were confirmed by the presence of peaks in the first derivative curve shown in Figure 20B.

A summary of all the thermal analysis data can be seen in Table 3.

Table 3. Summary thermal analysis data of raw silk cocoon and different degummed SF fibres measured by DSC and TGA. Tw, Tg and Td were determined by DSC, the rest were determined by TGA.

Silk sample	**Tw (°C)**	**Tg (°C)**	**Td (°C)**	**Water content (%)**	**Remaining mass at 950°C (%)**
Raw cocoon	71.0	231	307.0	5.9	25.5
De30 air dry	90.8	229.6	310.8	5.1	25.3
De30 oven dry	83.0	226.8	312.3	4.9	24.9
De60 air dry	80.6	228.3	307.8	5.1	25.7
De60 oven dry	84.5	221.7	314.0	5.6	23.9
De90 air dry	82.7	238.4	311.1	3.7	21.6
De90 oven dry	87.5	229.2	311.3	4.4	25.4

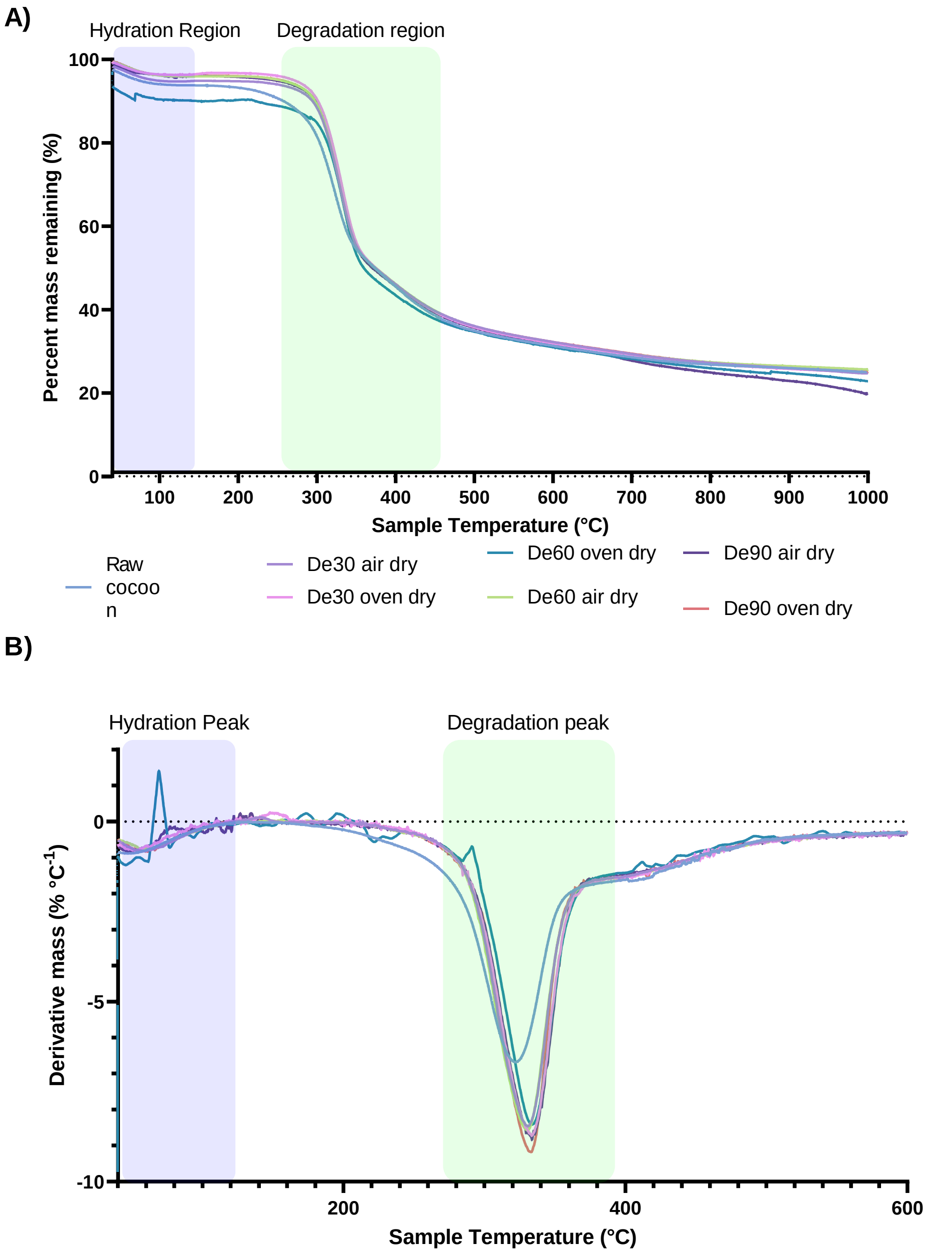

Figure 20. A) Percent of the mass remaining of the raw silk cocoon and degummed SF fibres measured by TGA heating from 30°C to 1,000°C at 10°C/min under nitrogen atmosphere with a gas flow of 20 mL/min. B) First derivative of the percent mass remaining. Regions related to bound water evaporation shown as blue and degradation shown green.

3.4.2. Dissolution of silk fibroin to obtain regenerated silk fibroin (RSF) solution

After obtaining the degummed SF fibres, four of those conditions were selected to be dissolved and used for future cell applications. These were: De30 air dry, De30 oven dry, De90 air dry and De90 oven dry.

To completely dissolve the SF fibres, a salt with high ionic strength is needed such as calcium chloride/formic acid [136], lithium salt solutions such as lithium bromide (LiBr) [137] or the mixture consisting of calcium chloride/water/ethanol ($CaCl_2/H_2O/C_2H_5OH$) also called Ajisawa's reagent [52, 137]. Recently, Cheng et al. [117] investigated the difference in cytocompatibility of RSF when using LiBr or Ajisawa's reagent. They concluded that both RSF materials had similar cytocompatibility even though when using Ajisawa's reagent a small amount of calcium was still present even after dialysis. However, this did not affect the performance of the RSF and using the ternary Ajisawa's reagent is a cheaper, non-toxic, and environmentally friendly alternative to LiBr.

One of the key components when using Ajisawa's reagent is the removal of the calcium salts. This is done via dialysis against deionised water. Since calcium is responsible for the solvation and stabilisation of the SF in the solution, its removal rate is very important [138]. If the salt is not removed successfully, RSF-materials are difficult to be produced due to the salt solvation, on the other hand, the more salt is removed the quicker the gelation or precipitation of RSF occurs [138].

Here, a 24-hour dialysis was proposed to remove the calcium salts under constant stirring. First, the deionised water was changed every half an hour to promote the diffusion of the salt, then water was changed once every hour and once every two hours. After this, the solution was left unchanged overnight with a further change after 20 hours. Finally, once the conductivity of the deionised water was less than 10 µS/cm, dialysis was considered finished. This was usually achieved after 24 hours. The profile of the dialysis can be seen in Figure 21.

Another important parameter to take into consideration when dialysing is the molecular weight cut-off (MWCO) of the dialysis tubes used. Here, three different MWCOs were used, i.e., 3.5 kD, 10 kD and 12 kD. To estimate the MW of the RSF solution, two samples, i.e., De30 oven dry and De90 oven dry, were analysed using SDS-PAGE as shown in Figure 22. The

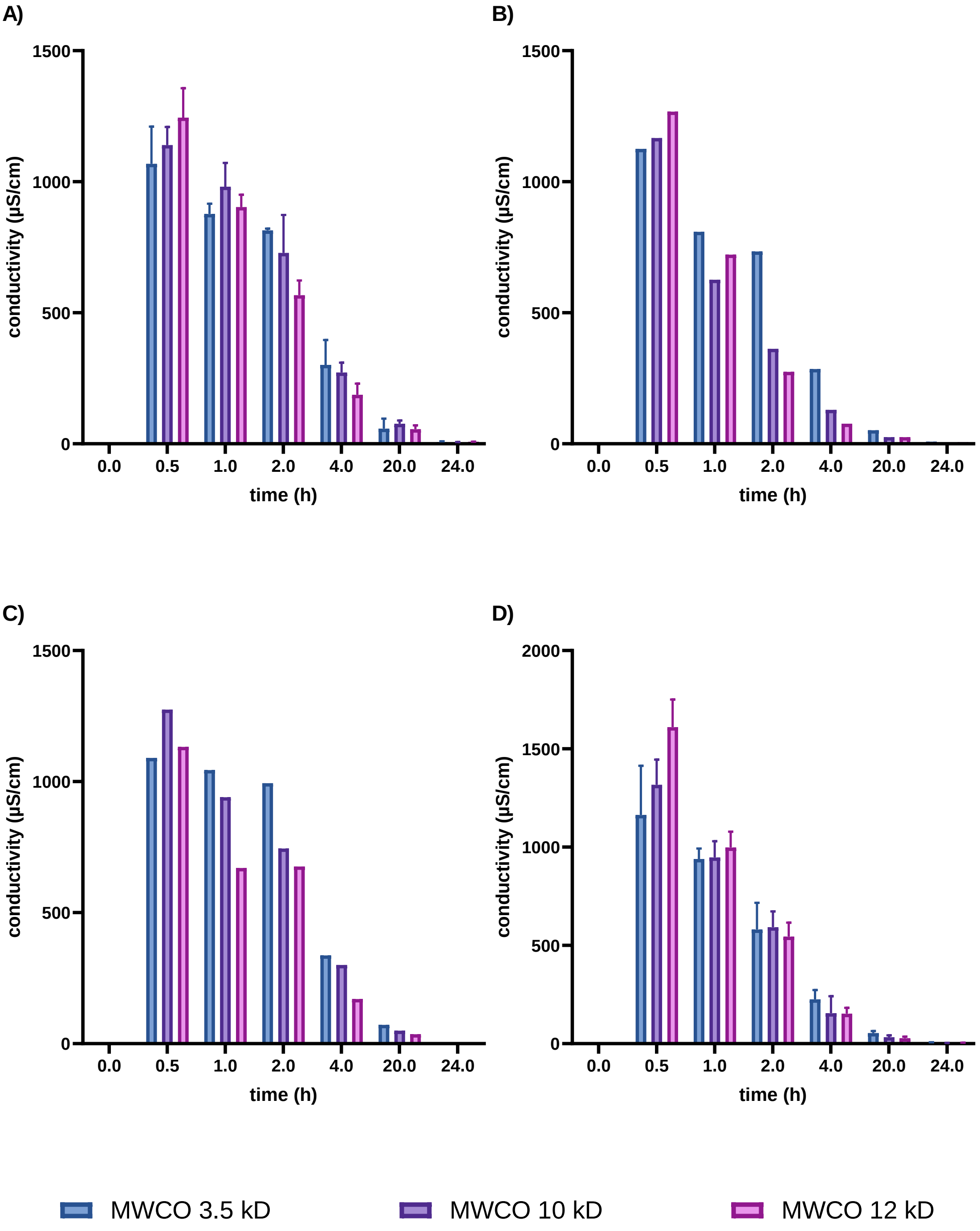

Figure 21. After dissolution of the SF fibres, the salts used in the Ajisawa's reagent are removed via dialysis. To follow the removal of the salts, the conductivity of the water is measure at specific time intervals, before every water change. These graphs represent the conductivity vs. time of A) De30 air dry, B) De30 oven dry, C) De90 air dry and D) De90 oven dry samples after dissolution. In this case, N=3 for A and D, while N=1 for B and C and, thus, no error bars are present for B and C.

intensity of the lanes corresponding to De30 oven dry was much higher than the intensity of the De90 oven dry samples. Moreover, RSF protein appeared as a smear in the SDS-PAGE and not as a band, meaning the protein had polydispersity. In addition, when the degumming time increased the smear looked less intense meaning that the protein was more degraded. This was consistent with data found in the literature [111].

However, even though the aim of the SDS-PAGE was to analyse the RSF protein at the MWCO (3.5 kD to 12 kD), it can be seen in Figure 22 that the bands for all RSF samples do not go lower than 85 - 50 kD. More optimisation of the SDS-PAGE protocol is needed to see the 3.5 - 12 kD bands.

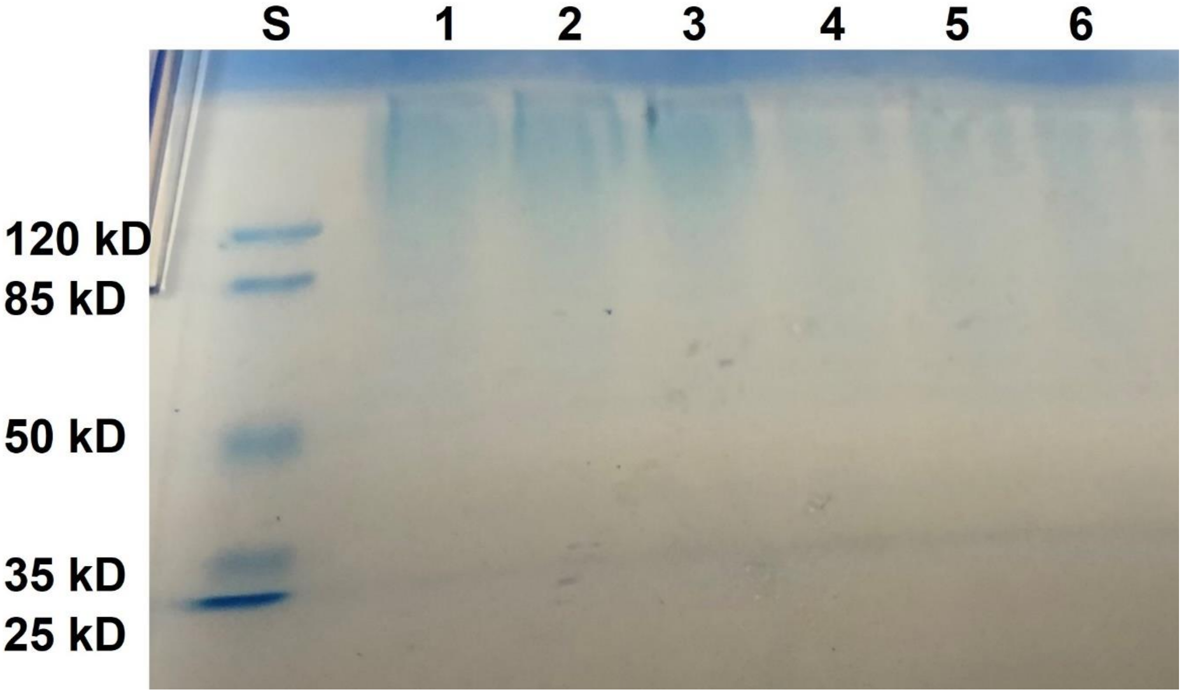

Figure 22. SDS-PAGE analysis of RSF dissolved from different degumming times and dialysed with different MWCO. Protein was stained with colloidal blue. This analysis was only repeated once (N=1). Lane S: standards; Lane 1: RSF from De30 oven MWCO 3.5 kD; Lane 2: RSF from De30 oven MWCO 10 kD; Lane 3: RSF from De30 oven MWCO 12 kD; Lane 4: RSF from De90 oven MWCO 3.5 kD; Lane 5: RSF from De90 oven MWCO 10 kD; Lane 6: RSF from De90 oven MWCO 12 kD.

Gravimetric concentration of RSF solution

After dialysis, the RSF solution was centrifuged to remove any insoluble particles that may have precipitated. When removing the calcium salt, the solvation of the RSF diminishes and precipitation can occur [138]. After centrifugation, the supernatant was recovered and the concentration of the RSF solution was obtained gravimetrically after evaporation of water at 60°C overnight. This is the standard procedure found in the literature [12, 131, 135, 139].

The final gravimetric concentration obtained depended on the ratio of SF fibres to Ajisawa’s reagent used. In this case, the mass ratio was 1 g of degummed SF fibre to approximately 10 g of Ajisawa’s reagent. The gravimetric concentration obtained for all the different degummed SF fibres can be observed in Figure 23. These ranged from 4.4 - 6.6 wt% but, there was no significant difference between the concentration obtained from different degummed SF fibres or between the different MWCO dialysis tubes used. A concentration of 4 wt% was chosen to be used for future application of the RSF solutions. Moreover, this value is comparable to the gravimetric concentration found in the literature [140]. Here, Zhang et al. obtained a 5 wt% RSF solution using the ternary solution $CaCl_2$/ethanol/H_2O, while the LiBr method can yield RSF solution with a concentration of up to 8 wt%.

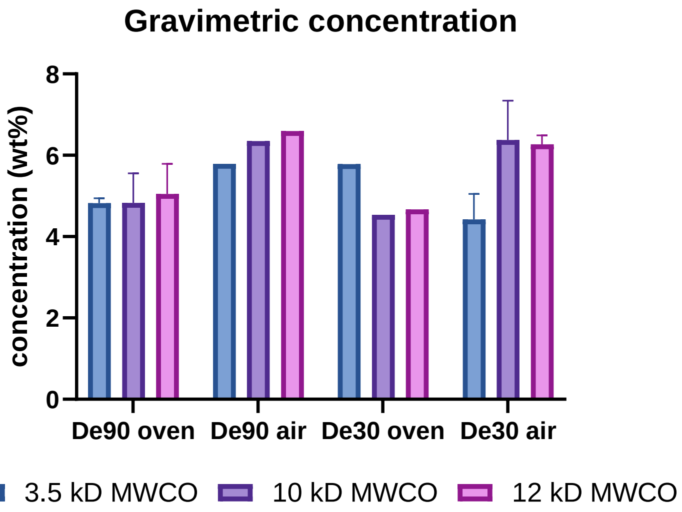

Figure 23. Different gravimetric concentration of the RSFA solution after dialysis obtained for A) De30 air dry, B) De30 oven dry, C) De90 air dry and D) De90 oven dry SF fibres. In this case, N=3 for A and D, while N=1 for B and C and thus, no error bars are present for B and C. Two-way factor analysis of variance (ANOVA) was performed. P values of *P < 0.05, **P < 0.01, ***P < 0.001 and ****P < 0.0001 were considered as significant.

3.4.3. *In vitro* studies with PC12-Adh neuronal-like cell line

The immortalised cell line, PC12 is derived from a rat pheochromocytoma. It is commonly used in neuroscience research and it has two variants: PC12 that grow in suspension and PC12 that have an adherent phenotype [105]. In this work, the PC12-Adherent (PC12-Adh) variant was the preferred one. This cell line can be differentiated into morphological and functional nerve cells when cultured in the presence of nerve growth factor (NGF), by Rho kinase (ROCK) inhibition or brain-derived neurotrophic factor (BDNF) [105, 107, 141]. This made them an ideal candidate for nerve models and studies where the final aim was to induce differentiation with other means [142]. Figure 24 shows the typical morphology of undifferentiated PC12-Adh, showing a polygonal shape and growth in tight clusters.

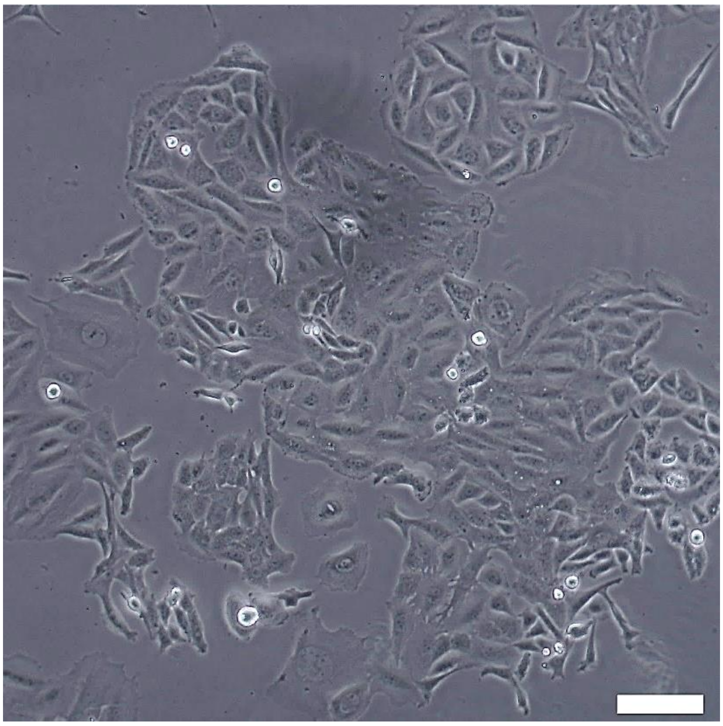

Figure 24. Brightfield images of undifferentiated PC12-Adh growing in tissue culture plastic (TCP) in growth media, i.e., 1% glutamine, 0.5% amphotericin B, 1% penicillin/streptomycin and 10% foetal calf serum (FBS) in Dulbecco's Modified Eagle Medium (DMEM), in a humidified atmosphere with 5% CO_2 at 37°C. Scale bar is 100 µm.

In this study, SF fibres were obtained from different degumming times and different drying methods. In addition, these fibres were dissolved to obtain the final RSF solution with different MWCO. Therefore, the following materials conditions were selected for the next experiments, De30 air, De30 oven, De90 air and De90 oven, and all the MWCOs for each of them.

Cell attachment and metabolic activity was analysed. To do this, al the RSF solutions at a concentration of 40 mg/mL were spun coated onto 13 mm diameter cover glasses and then, their conformation was changed from random coil (soluble state found in RSF solution) to β-sheet, insoluble state, using a 95% ethanol solution. This was done to prevent the RSF from redissolving into the media during cell culture. Studies carried out by other authors have proven that ethanol treatment can induce this conformational change [121, 143, 144]. Moreover, Terada et al. [120] investigated how ethanol treatment can affect the surface properties of RSF films. They concluded that increasing the concentration of ethanol used to induce the conformational change, increased the rigidity of the RSF surfaces.

Another important step is the sterilisation procedure of the RSF surfaces prior to cell culture. Different methods of sterilisation can cause protein-based materials such as silk to have different responses to what was expected from other materials. The effects of autoclaving, ultraviolet (UV) exposure, γ irradiation or immersion in ethanol or methanol have been previously studied [145-148].

Gil et al. [147] studied how autoclaving and ethanol immersion affected RSF materials. They concluded that while autoclaving resulted in structural modification that caused changes in degradation and mechanical properties, immersion in ethanol caused minor crystalline (changes in β-sheet content) adjustment without affecting degradation or mechanical properties. On the other hand, De Moraes et al. [148] concluded that sterilisation methods such as immersion in ethanol, autoclaving or ethylene oxide, can induce changes in RSF membranes, while membranes sterilised by UV or γ irradiation maintained similar properties to the non-sterilised materials. However, there is no such thing as a standard method for sterilisation and at the end, the selected method depends on the final application and the most important material properties that need to be preserved [146].

In our study, keeping constant the β-sheet content and surface morphology was important and, thus, UV irradiation was chosen as the technique chosen for the sterilisation step. This method causes the scrambling of DNA/RNA molecules, preventing microorganisms such as bacteria and virus from multiplying.

Cell attachment studies – crystal violet assay

Cell attachment to RSF scaffolds is generally poor [2]. This has previously been related to the high content of non-polar amino acids [13] and the crystalline hydrophobic structure of silk II [1]. However, this can also occur partly because of the processing conditions the silk was exposed to, from raw silk cocoon to the final RSF scaffold that can be used in specific applications.

Therefore, cell attachment on different RSF surfaces was studied via crystal violet assay. This assay is mostly used to indirectly quantify cell density. Crystal violet binds to DNA and proteins in the nucleus and cytoplasm of the cells that are attached to the RSF surface. This method relies on the assumption that all live cells remain attached to the surface while dead cells will be washed away. Then, unbound crystal violet was washed off, and bound crystal violet was redissolved and its absorbance was measured [149]. There is a linear relationship between the concentration of cells and the absorbance, more cells mean absorbance will be higher. In this case, cell attachment was measured as a percentage relative to the positive control (TCP+) as seen in Figure 25. Here, there can also be seen a negative control (TCP-) which shows that even when apoptosis was induced in cells growing on TCP, some staining occurred due to remaining DNA or proteins after cell detachment.

In Figure 25A, SF fibres were originally obtained by 30 min of degumming and air-dried prior to dissolution. Cell attachment (%) was significantly different between TCP+ and RSF 10 kD, while RSF 3.5 kD and RSF 12 kD have a similar attachment to that of the positive control. In the same way, there were significant differences between the cell attachment of RSF 10 kD compared to that of RSF 3.5 kD and RSF 12 kD, but overall cells appeared to be attaching to all RSF surfaces. However, when the drying method was changed to oven, the cell attachment for all three RSF surfaces i.e., 3.5 kD, 10 kD and 12 kD, drastically decreased compared to the positive control as seen in Figure 25B. Similarly, this happened with RSF obtained by degumming 90 minutes. All RSF surfaces including those air-dried and oven-dried and all MW exhibited decreased cell attachment compared to the positive control as seen in Figure 25C and Figure 25D.

Previous reports associated the lack of cell attachment to the crystalline hydrophobic structure of silk [1, 13] and, while this is still of relevance, the lack of cell adhesion can also be related to the over processing of the silk materials as seen in Figure 25. Rockwood et al. [12] stated that boiling time during degumming longer than 30 min will degrade the silk fibroin. Similarly, Wang et al. [150] reported that using temperatures above 100°C can seriously damage the SF peptide chain. All this is consistent with the results obtained in this study and represented in Figure 25.

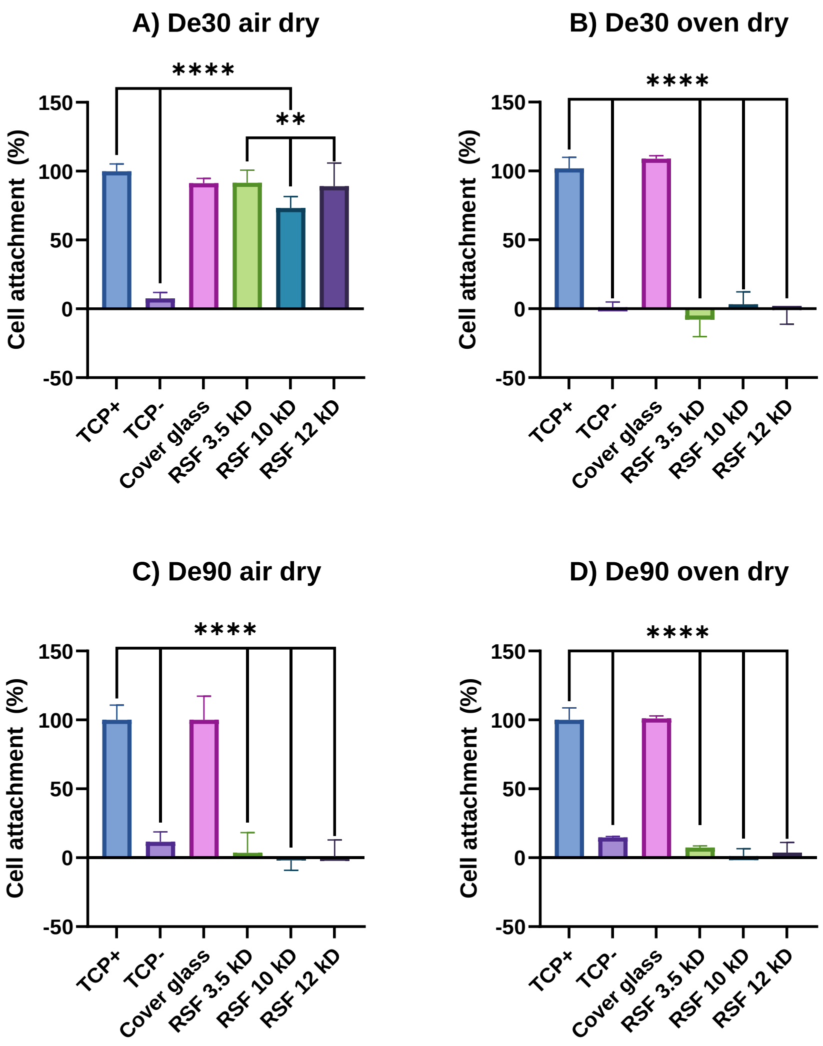

Figure 25. Graphical representation of cell attachment (%) relative to the positive control (TCP+) obtained with crystal violet assay. Results from silk A) De30 air dry, B) De30 oven dry, C) De90 air dry and D) De90 oven dry are shown. RSF 3.5 kD, RSF 10 kD and RSF 12 kD refer to RSF obtained with different MWCO tubes during dialysis. One-way factor analysis of variance (ANOVA) was performed. P values of $*P < 0.05$, $**P < 0.01$, $***P < 0.001$ and $****P < 0.0001$ were considered as significant.

Fluorescence imaging of cell seeded on RSF surfaces

After quantitatively analysing the relative cell attachment on different RSF surfaces, cells can be stained to qualitatively analyse attachment and morphology. PC12 cell nuclei were stained with DAPI (colour blue), the F-actin present in the cytoplasm is stained with FITC-Phalloidin (colour green) as seen in Figure 26. Cells were present on the surfaces of RSF De30 air dry (Figure 26 A, B and C) showing a mixture of fully spread cell and round cells attached lightly by electrostatic interaction. On the other hand, positive controls (Figure 26 M and N) show a layer of adhered cells. The rest of the RSF samples, De 30 oven dry (Figure 26 D, E and F) De90 air dry (Figure 26 G, H and I) and De90 oven dry (Figure 26 J, K and L) exhibited a very limited number of cells on the surfaces. Moreover, the overall morphology of these groups exhibited round cells with almost no flattening or spreading, indicating the adhesion was poor. This further confirmed the results obtained by crystal violet shown in Figure 25.

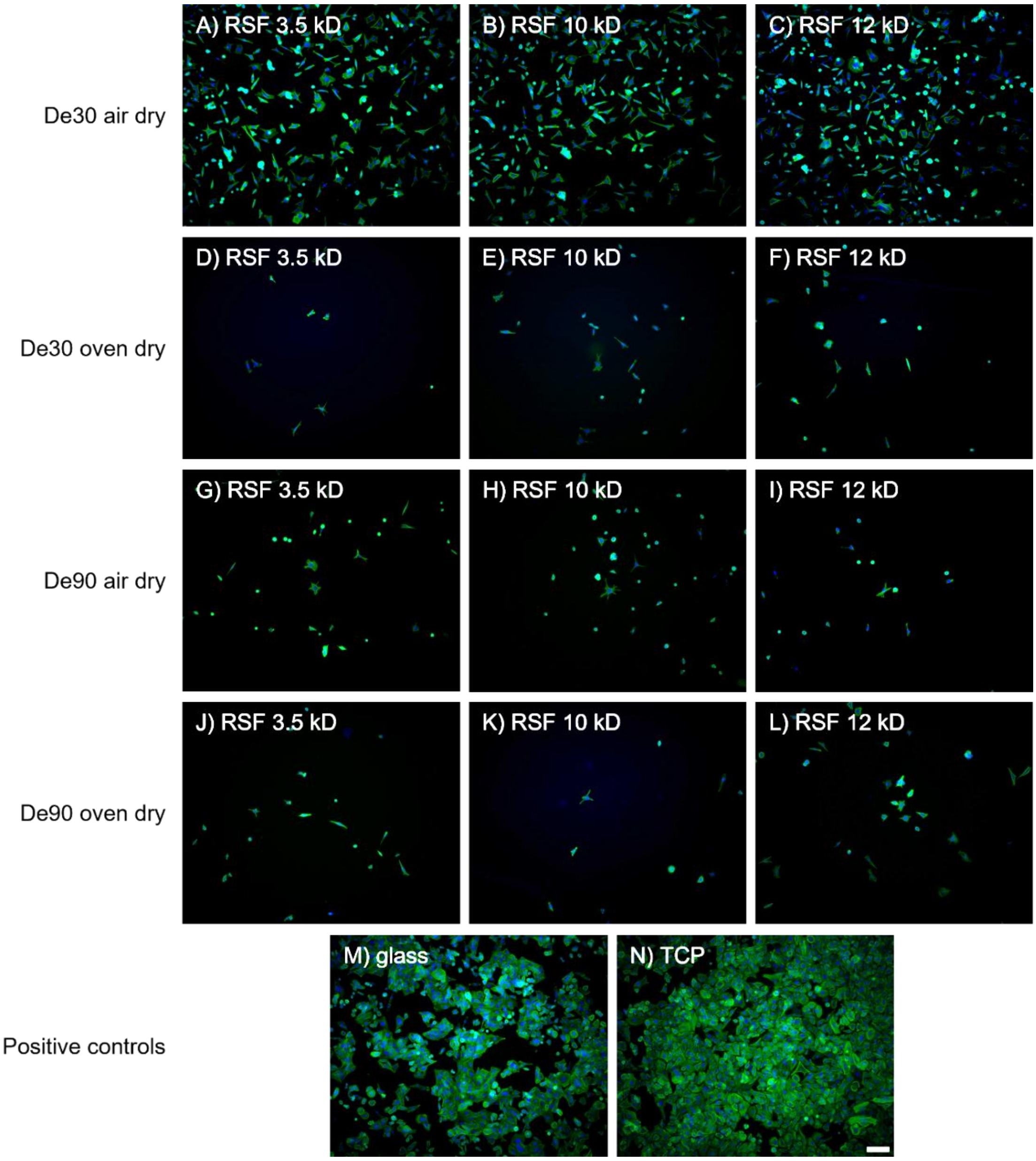

Figure 26. Fluorescent image of PC12-Adh cells on different RSF surfaces and positive controls. Samples are: De30 air dry – A) RSF 3.5 kD, B) RSF 10 kD, C) RSF 12 kD; De30 oven dry – D) RSF 3.5 kD, E) RSF 10 kD, F) RSF 12 KD; De00 air dry – G) RSF 3.5 kD, H) RSF 10 kD, I) RSF 12 kD; De90 oven dry – J) RSF 3.5 kD, K) RSF 10 kD, L) RSF 12 kD; and positives controls are M) uncoated 13 mm round cover glass, N) tissue culture plastic (TCP). Scale bar is 100 µm.

Cytocompatibility studies – resazurin/resorufin assay

Cytocompatibility is one of the most important properties of biomaterials, this means the biomaterial does not cause any undesired effect while performing its desired function. Silk is a natural derived polymer composed of protein chains that are considered highly cytocompatible. However, although native silk possesses excellent mechanical properties and cytocompatibility, this material is rarely used in its native state. As mentioned before, to obtain a regenerated silk fibroin (RSF) solution that can be used for different applications, native silk has to be processed and therefore, its properties do not remain the same and need to be checked again.

In this case a direct approach to measure metabolic activity of the cells is used. The irreversible reduction of resazurin, a nontoxic (blue) dye, to resorufin, another nontoxic fluorescent (pink) dye is mediated by metabolically active cells and so, it can be used as a cell viability indicator (Figure 27). Specifically, resazurin is reduced by aerobic respiration in the mitochondria of viable cells in the presence of NADH, NADPH or other biological reductive species [151, 152].

In this study, cells were seeded directly on each of the RSF surfaces. Then, metabolic activity of PC12-Adh cells was evaluated after 48 h in culture. Results are shown in Figure 28. For RSF surfaces made from De30 air dried silk (Figure 28A), metabolic activity was half of that of the positive control (TCP+). However, the rest of the RSF groups (Figure 28B, C and D) showed no metabolic activity compared to the positive control (TCP+). This was consistent with crystal violet assay results, where De30 air dried RSF was the only group that showed cell attachment. However, even though for this group cells adhered to the surface and proliferated they do not do so at the same rate as the positive control and therefore, improvement is needed.

Moreover, in the literature, Wray et al. [111] showed that when the duration of the degumming process was increased, cell viability decreased. In this case, MTT (3-(4,5-dimethylthiazol-2-yl)-2,5-diphenyl tetrazolium bromide) assays were carried out instead of resazurin/resorufin assays but the conclusion was the same. The longer the silk is subjected to the degumming process, or even heated to dry, the material became less adherent and viable for tissue engineering applications.

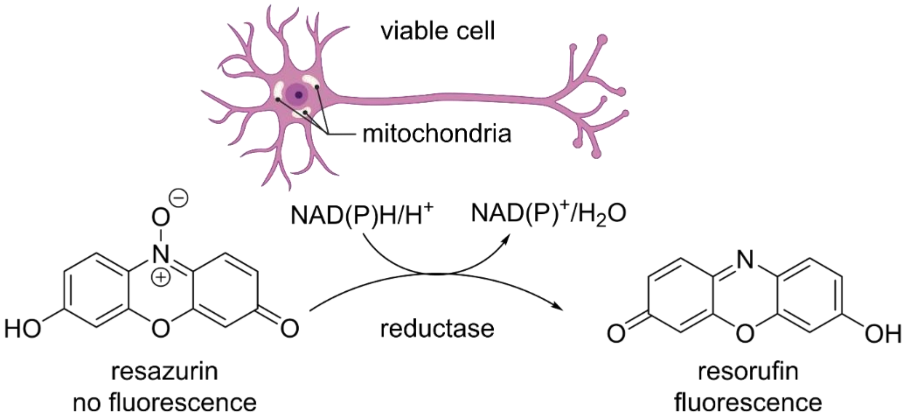

Figure 27. Schematic representation of the enzymatic reduction of resazurin to resorufin. Adapted from the work of Lavogina, D., et al. [151] and Silva, F.S.G., et al. [151, 152]

However, since cells did not attach to some of the RSF samples that were being evaluated, direct cytocompatibility cannot be studied. For this reason, an indirect approach, where the media was preconditioned with each sample before using it with cells, was also used to see if the lack of cells on the RSF surfaces was due to something leaching into the environment. This could explain why cells were not adhering to the surfaces.

In Figure 29A the metabolic activity of the positive control (TCP+) was not significantly different than that of the three RSF groups, which means that there was nothing leaching out that affected the overall metabolic activity of the cells growing. In the rest of the groups, all RSF samples had a significantly lower metabolic activity except for the group De90 oven dry RSF 12 kD which showed no significant difference with the positive control as seen in Figure 29D. This means that even though cells were not able to grow directly on that RSF surface, as proven with crystal violet and direct resazurin/resorufin assay, this surface was not releasing anything that reduced cell viability.

Having a non-cytotoxic non-fouling surface can be of advantage in the biomedical field. These types of surfaces can prevent unwanted cell adhesion when implanted for example in vascular applications [153]. For example, Sivkova et al. reported the use of hierarchical polymer brushes that had excellent cell adhesion but were resistant to fouling from blood cells [153]. Moreover, patterning and 2D spatial distribution can be of great interest to guide and control the growth of cells. Some strategies to achieve this are: immobilisation of poly(ethylene glycol) (PEG) and use of hydrophobic polymers, for example [154].

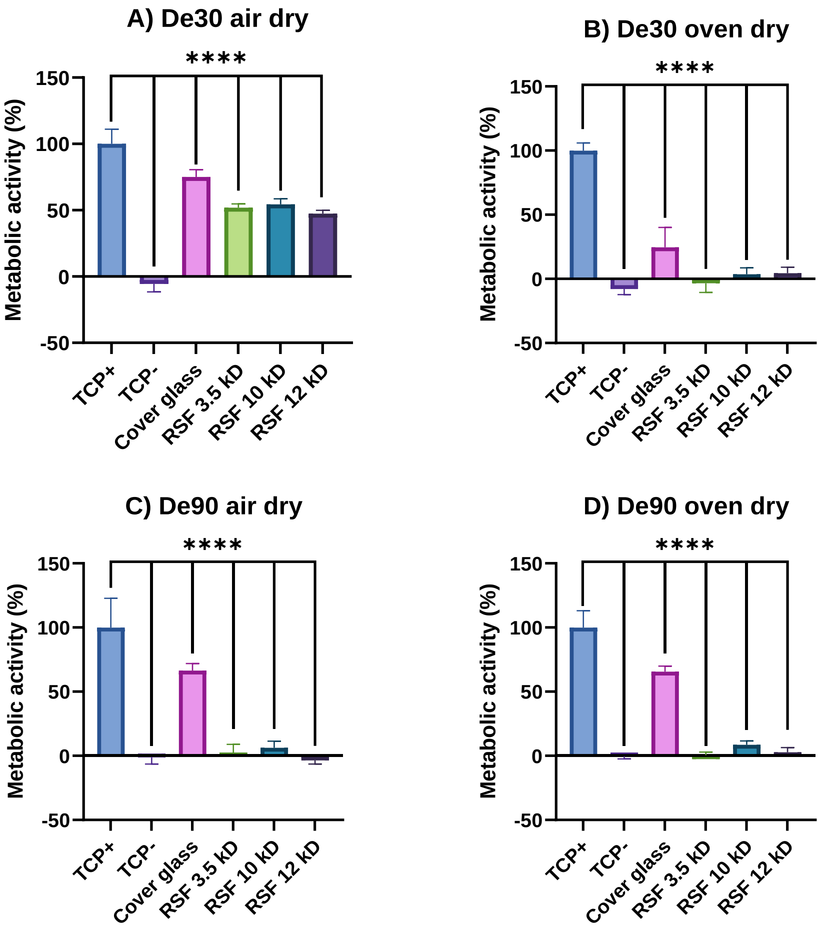

Figure 28. Graphical representation of direct metabolic activity (%) relative to the positive control (TCP+) obtained with resazurin/resorufin assay. Results from silk A) De30 air dry, B) De30 oven dry, C) De90 air dry and D) De90 oven dry are shown. RSF 3.5 kD, RSF 10 kD and RSF 12 kD refer to RSF obtained with different MWCO tubes during dialysis. One-way factor analysis of variance (ANOVA) was performed. P values of *P < 0.05, **P < 0.01, ***P < 0.001 and ****P < 0.0001 were considered as significant.

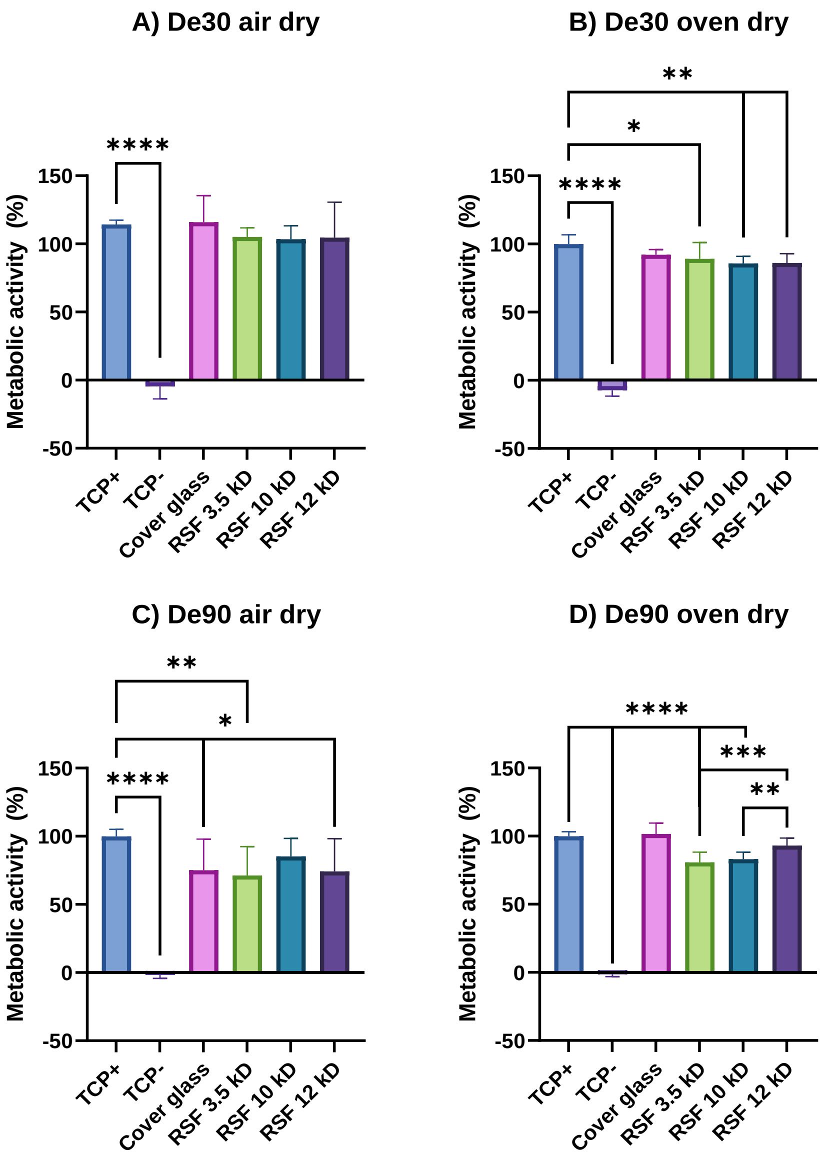

Figure 29. Graphical representation of indirect metabolic activity (%) relative to the positive control (TCP+) obtained with resazurin/resorufin assay. Results from silk A) De30 air dry, B) De30 oven dry, C) De90 air dry and D) De90 oven dry are shown. RSF 3.5 kD, RSF 10 kD and RSF 12 kD refer to RSF obtained with different MWCO tubes during dialysis. One-way factor analysis of variance (ANOVA) was performed. P values of *P < 0.05, **P < 0.01, ***P < 0.001 and ****P < 0.0001 were considered as significant.

3.5. Conclusion

In this chapter, a naturally derived silk polymer has been used that can be tuned to either promote cell attachment or act as a non-fouling material depending on the wanted final application by only modifying the material’s processing while retaining cytocompatibility. Since silk is a natural protein, its processing determines the final properties of the material.

While modifying the degumming times from 30 to 90 min showed clear evidence that the removal of sericin was complete as shown by the SEM images. It also leads to a clear degradation of the fibres. However, in the DSC analysis carried out no significant shift in the degradation temperatures was detected, but the overall degradation temperature found in the literature was higher overall [132, 133]. This is associated with a decrease in the crystalline content of the SF fibres and a subsequent degradation.

However, SF fibres after degumming still need to be processed so they can be transformed into the required biomaterial. Dissolution of SF fibres using Ajisawa's ternary reagent composed of a mixture of calcium chloride:ethanol:water ($CaCl_2$:EtOH:H_2O) was selected for this process since it is a more cost-effective and environmentally friendly alternative to using LiBr solutions. All SF fibres were dissolved following the same protocol, and dialysis was carried out to remove the $CaCl_2$ salts. Complete removal of the salts is challenging but these residual salts do not affect cytocompatibility according to Cheng et al. [117]. Different MWCO dialysis tubes were used during this process but no difference in MW was observed in the SDS-Page. This only showed a thicker band at higher MW for RSF solutions that were degummed for 30 minutes than the ones obtained for fibres degummed for 90 minutes, lower MW is again correlated with a more degraded SF fibre obtained during longer degumming times, but no difference was observed when using different MWCO tubes during dialysis.

Several of this samples, were converted into RSF films via spin coating and its conformation was changed from water soluble silk I to water insoluble silk II using 95% ethanol solution. Cell adhesion and cytocompatibility studies were conducted using PC12-Adh cell line showing a correlation between the degumming process and the cell adhesion properties. While lower degumming times allowed the cells to attach and elongate on the RSF surfaces, when the degumming time was 90 minutes, cells were unable to attach to the RSF surfaces. Moreover, even though the use of different MWCO dialysis tubes showed no difference in the MW during the SDS-Page, cells seemed to adhere to better to 12 kD MWCO showing no significant difference with the positive control as shown in the crystal violet assay. At the same time, cytocompatibilities studies such as resazurin/resorufin assay showed all RSF surfaces to be biocompatible.

In conclusion, when subjected to high temperatures for long periods of times, silk protein can be degraded, and its properties may vary. It has been found that RSF obtained from 90 min of degumming and using 12 kD MWCO during dialysis, provided a final RSF surface that had high cytocompatibility but prevented cell adhesion. The modification of silk surfaces by these methods can provide a way of tuning the hydrophilicity of SF surfaces and obtain control over cell adhesion [2].

For example, SF can be combined with polylysine for wound dressing [155, 156] or in neural tissue [157-159] applications, peptides such as RGD [160-162], IKVAV [48, 162]. In the following chapter, the use of a novel amphiphilic peptide composed of three units of isoleucine and one unit of lysine (I_3K) for cell attachment will be investigated.

Chapter 4. Use of novel amphiphilic peptide to improve cell attachment on non-fouling RSF surface

4.1. Introduction

The tissue engineering field relies heavily on the development of scaffolds that can support the growth of specific cells and tissues to regenerate or restore their main function. Several types of materials can be used for this purpose, a wider classification would be natural materials such as silk fibroin (SF), collagen or polyhydroxyalkanoates (PHAs) or synthetic such as polycaprolactone (PCL) or polylactic acid (PLA). The final objective of all these materials is to mimic the extracellular matrix (ECM) and to provide a cytocompatible, biodegradable environment to promote cell adhesion and proliferation [163].

Some materials derived from SF lack a bioactive surface that can support cell attachment and growth [2]. This can be due to its high content of non-polar amino acids [13], the crystalline hydrophobic structure of silk II [1] or the processing of these materials [12, 111, 150] as demonstrated in Chapter 3. Subsequently, this can be improved by coatings or further chemical modifications [27, 46, 47, 49, 50]. The combination of the protein SF with other natural or synthetic peptides is a promising tool to obtain a highly cytocompatible and biodegradable material.

4.1.1 Self-assembly peptides in peripheral nerve regeneration

Self-assembly peptides (SAP) are promising candidates in the tissue engineering field. These peptides are designed to self-assemble into well-defined structures and are engineered to mimic the extracellular matrix (ECM), providing a supportive environment for cell adhesion, proliferation, and differentiation [164, 165] . SAPs can form different nanostructures through non-covalent links such as nanofibres, nanoparticles and micelles [166-169]. This self-assembly can spontaneously occur because of pH, temperature or ionic strength changes [167] but can also be achieved by different building blocks, such as a hydrophobic tail combined with a hydrophilic head. These are named as amphiphile self-assembly peptides [170]. This type of self-assembly is carried out by dissolving the peptide in an aqueous solution where the hydrophobic and electrostatic interactions generate different structures such as micelles, nanovesicles or nanotubes [171]. In this case the hydrophilic head will be facing outwards in this structure and therefore, will be readily available. The hydrophobic residues usually are composed of amino acids such as alanine, valine, or leucine, while the hydrophilic residue can be made up of bioactive sequences such as RGD (where "R" is amino acid arginine, "G" glycine, "D" aspartic acid), IKVAV (where "I" represents amino acid isoleucine, "K" lysine, "V" valine and "A" alanine) or K (where "K" represents the amino acid lysine). These peptides have already been used to improve cell attachment and viability of neuronal cells [46, 86, 87].

One significant advantage of using SAP coatings lies in their inherent biocompatibility making them suitable for biomedical applications. For example, Sieminski et al. [172] showed that different peptide sequences can influence cell behaviour such as adhesion and morphology and thus, these SAP peptides can be tuned for different applications. Moreover, functionalizing peptide coatings with specific cell-binding motifs, such as the RGD sequence, has proven effective in enhancing cell attachment and guiding tissue regeneration processes.

SAP coatings are of special interest in the field of nerve regeneration. A significant contribution to this field is demonstrated by Yang et al. [173], who explored self-assembling peptide hydrogels functionalized with laminin and BDNF, finding they enhanced peripheral nerve regeneration. Their successful integration of these coatings within neural tissue scaffolds facilitated enhanced cell attachment and neurite outgrowth. Similarly, Lu et al. [174] reported that bioactive self-assembling peptide hydrogels functionalized with BDNF and NGF promoted peripheral nerve regeneration, highlighting their biocompatible and bioactive properties.

Moreover, self-assembling peptides, when designed with specific motifs such as IKVAV and KLT, can provide a dual-action mechanism. Research by Shen et al. [175] explored the combination of these motifs in peptide gels, demonstrating enhanced effects on Schwann cells, which play a vital role in peripheral nerve repair. This combination results in a hydrophilic environment that significantly helps proliferation and differentiation, both of which are necessary to achieve an effective nerve regeneration.

4.2. Aims and objectives

In this chapter, we focus on investigating the fabrication and characterisation of I_3K-RSF surfaces as well as their suitability for cell attachment and cytocompatibility. It details the coating process using an I_3K solution, followed by surface characterization through AFM and contact angle measurements. Furthermore, it explores the role of RSF in stabilizing the I_3K coating and optimises self-assembly conditions to enhance cell attachment and biocompatibility.

The aims of this chapter were:

1. Fabrication and characterisation of RSF:I_3K surfaces
2. Assess the cell attachment and cytocompatibility of RSF:I_3K surfaces

The objectives of this chapter were:

1. Coating of RSF surfaces using a solution of I_3K in 20mM HEPES buffer (pH 6.0)
2. Characterisation the RSF:I_3K surfaces via AFM and contact angle measurement
3. Assessment the need to use RSF to keep the I_3K coating on the surface
4. Assessment the optimal self-assembly time to improve cell attachment when comparing RSF to RSF:I_3K surfaces
5. Direct and indirect assessment of cytocompatibility via resazurin-resorufin assay
6. Imaging and assessment of cell morphology via fluorescent staining

4.3. Materials and methods

4.3.1. Materials

Details of the materials used were described in Chapter 2 Section 2.1.

4.3.2. Silk degumming and dissolution

The RSF solution preparation process was described in Chapter 2 Section 2.2.

B. mori silk cocoons were degummed for 90 min, dissolved using Ajisawa’s method and dialysed using a 12 kD MWCO dialysis tube. RSF solution was then diluted to 40 mg/mL when needed.

4.3.3. Dissolution of peptide I_3K

The dissolution of I_3K peptide was described in Chapter 2 Section 2.7. The peptide was dissolved at a concentration of 5 m/mL and left to self-assemble at room temperature.

4.3.4. Preparation of RSF and RSF:I_3K surfaces via spin coating

Spin coating procedure was described in Chapter 2 Section 2.8. RSF (De90 oven dry, 12 kD MWCO) and I_3K (left to self-assemble for 0, 1, 3, 5 and 7 days) were used at a concentration of 40 mg/mL and 5 m/mL. Here, 13 mm round cover glasses with a thickness of 1.5 mm (Avantor VWR, UK).

4.3.5. AFM

The AFM analysis was described in Chapter 2 Section 2.9.1.

4.3.6. Contact angle

The contact angle process was described in Chapter 2 Section 2.9.2.

4.3.7. *In vitro* studies with PC12-Adh neuronal-like cell line

General cell culture

General cell culture procedure as well as general culture media preparation were described in Chapter 2 Section 2.5.1.

Cell attachment assay: crystal violet

Crystal violet assay was described in Chapter 2 Section 2.5.2.

Metabolic activity assay: resazurin assay

Metabolic activity assay carried out directly or indirectly was described in Chapter 2 Section 2.5.3.

4.3.8. Fluorescence Microscopy and analysis of cells

Staining and fluorescence imaging procedures were described in Chapter 2 Section 2.6.1. and Chapter 2 Section 2.6.3.

4.3.9. Statistical analysis

Data were presented as mean ± standard deviation (N = 3 or otherwise mentioned). One-way or two-way factor analysis of variance (ANOVA) was performed for all multiple group experiments. P values of $*P < 0.05$, $**P < 0.01$, $***P < 0.001$ and $****P < 0.0001$ were considered as significant. The statistical analysis was performed using Prism GraphPad software. Equality was confirmed by Tukey's multiple comparison test.

4.4. Results and Discussion

4.4.1. Self-assembly of I_3K

The synthetic peptide Ac-I_3K-NH_2 (purity >98% w/w), referred to as I_3K, has three units of the hydrophobic amino acid isoleucine, I, and one unit of the hydrophilic amino acid lysine, K, which gives it amphiphilic properties. The N-terminus is capped with an acetyl group (Ac, CH_3-) while the N-Terminus is capped with an amide group (NH_2-) (Figure 30) during the synthesis of the peptide [176]. This is done to increase stability and reduce unwanted side reactions during synthesis [177].

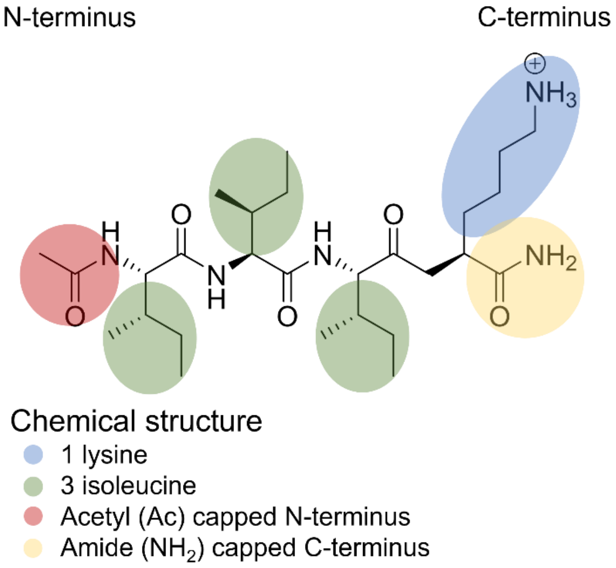

Figure 30. Chemical structure of the synthetic peptide Ac-I_3K-NH_2 (I_3K), where the lysine side chain is marked in blue and isoleucine side chains are marked in green. Done with help of ChemDraw.

The I_3K peptide was used in combination with RSF surfaces obtained from degumming 90 oven dry and a MWCO during dialysis of 12 kD, referred to as RSF from now on. In Chapter 3, it was proven that these RSF surfaces did not promote cell attachment but were cytocompatible, since it did not release anything toxic to the media. Therefore, it is a good candidate to be used as a non-fouling surface to test the effect of the I_3K peptide.

Due to this amphiphilic structure, when the peptide is dissolved in an aqueous solution such as 20 mM HEPES buffer, it rearranges itself with all the K groups facing outwards, while the I groups are facing inwards as illustrated in Figure 31, with time the I_3K self-assembled bilayer structures that aggregate to form nanotubes. This dynamic self-assembly behaviour has been previously investigated by Wang [178] and Xu [176].

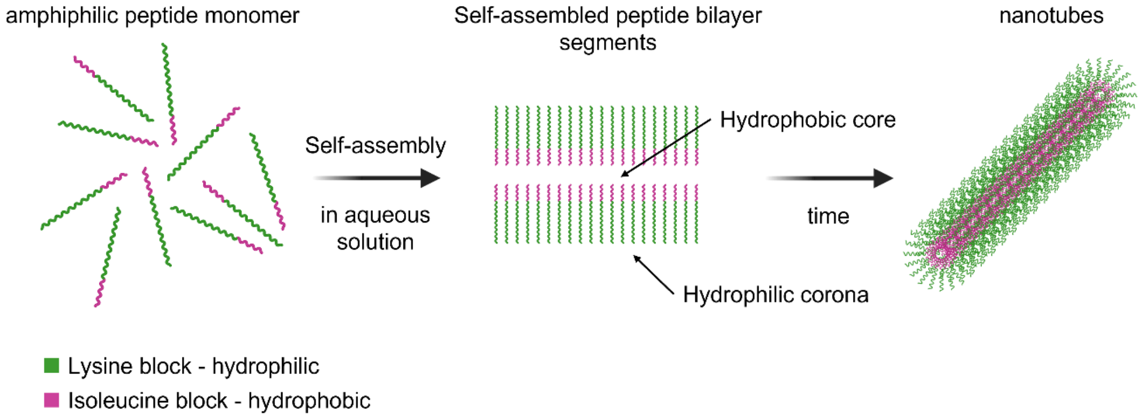

Figure 31. Schematic of how amphiphilic peptides self-assemble into bilayer segments that with incubation time developed into nanotubes. Adapted from the work of Wang, Q., et al. [178] and Deshmukh, S.A., et al. [178, 179]. Created with BioRender [93].

To study the self-assembly behaviour of I_3K at pH 6 in 20 mM HEPES buffer, AFM was carried out. For this, RSF and RSF:I_3K samples were spin coated on cover glasses after leaving the I_3K to self-assemble in aqueous solution for 0, 1, 3, 5 and 7 days. The resulting nanofibrils can be observed in Figure 32. At day 0 (Figure 32B), meaning the peptide was spun coated right after dissolution, the bilayer segments had started to form but had not fully developed into nanotubes. On the other hand, long nanotubes were found on the RSF surfaces from day 1. The length of these nanofibrils was difficult to analyse because they were larger than the field of view of the scan. However, it has been reported by Wang et al. [178] that the I_3K peptide nanostructure can reach lengths of several micrometres and 11.2 nm in width after 7 days. These dimensions however, increased with the incubation time.

4.4.1. Combination of RSF:I$_3$K

Moreover, using a tool to calculate the theoretical properties of the synthetic peptide I$_3$K such as PepCalc (Innovagen AB, Sweden), the approximate iso-electric point (IEP) of this synthetic peptide would be 13-14. This is the pH at which the peptide has no electric charge, and, therefore, below this pH it would have a positive charge in the lysine group as seen in Figure 30. On the other hand, RSF has an IEP of 4.6 leading to an overall negative charge at

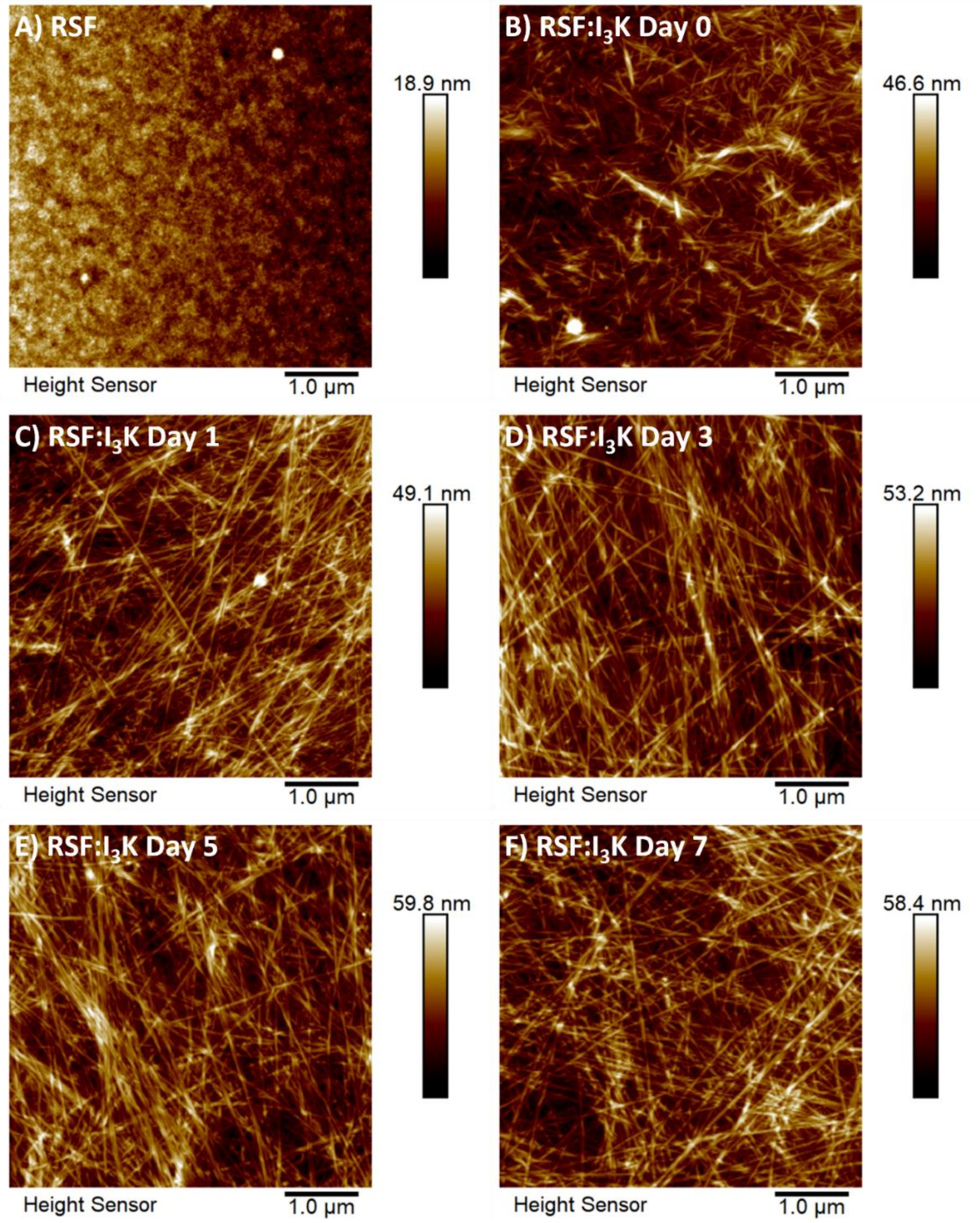

Figure 32. AFM surface topography micrographs of A) RSF surface, B) RSF:I$_3$K surface on day 0 of self-assembly, C) RSF:I$_3$K surface on day 1, D) RSF:I$_3$K surface on day 3, E) RSF:I$_3$K surface on day 5 and F) RSF:I$_3$K surface on day 7. The concentration of RSF was 40 mg/mL and I$_3$K was 5 mg/mL.

pH > 4.6 [135, 180]. This positive charge of I_3K at neutral pH was confirmed by Hu et al. [176] who attributed the origin of this positive charge in the lysine side group to the amidation of the C-terminus.

Since the I_3K peptide is dissolved at a pH of 6 when the RSF surface is coated with it, and then the RSF:I_3K surface is used as a scaffold submerged in culture media that is formulated to maintain a physiological pH of 7.4 (DMEM), it is theorised that I_3K and RSF are linked via

electrostatic interaction such as salt bridges. Electrostatic interaction between proteins such as SF and peptides have been studied before. Aye et. al [181] reported the use of a SF hydrogel electrostatically functionalised with a peptide for antimicrobial applications.

To prove that this electrostatic interaction between RSF and I_3K is enough to maintain the I_3K coating during cell culture, AFM was carried out on RSF, RSF:I_3K and I_3K surfaces before and after simulating cell culture conditions, i.e., surfaces were scanned before and after being incubated for 7 days at 37°C in a humidified atmosphere with 5% CO_2.

As seen in Figure 33 A1 and A2, the maximum height of the RSF surface increased after being submerged in deionised water for 7 days, from 26 nm to 39.8 nm. The swelling behaviour of RSF films has been studied before [182-184]. Ramachandran et. al compared the swelling of RSF films of different origin, i.e., *Hilosamia ricini*, *Antheraea assamensis*, and *Bombyx mori*, and concluded that RSF films from *B. mori* retained more water than its counterparts [183]. On the other hand, Lawrence et. al [184] reported that alcohol treated RSF films had a less ordered secondary structure that allowed it to retain more water. This can explain why the maximum height of the AFM scan had increased.

Similarly, when I_3K was coated on the RSF surface, the maximum height increased (Figure 33 A1 and B1). However, after submerging these samples in cell culture conditions the maximum height decreased. This can be explained as the outermost part of the I_3K coating does not have a strong enough electrostatic interaction with the other I_3K fibres or the RSF surface and, thus, they detach during cell culture conditions. However, there are still nanofibres coating the RSF surface as seen in Figure 33 B2.

Lastly, I_3K was coated directly on the surface of cover glasses. This surface then had a higher maximum height compared to the RSF (Figure 33 A1) and RSF:I_3K (Figure 33 B1) coated

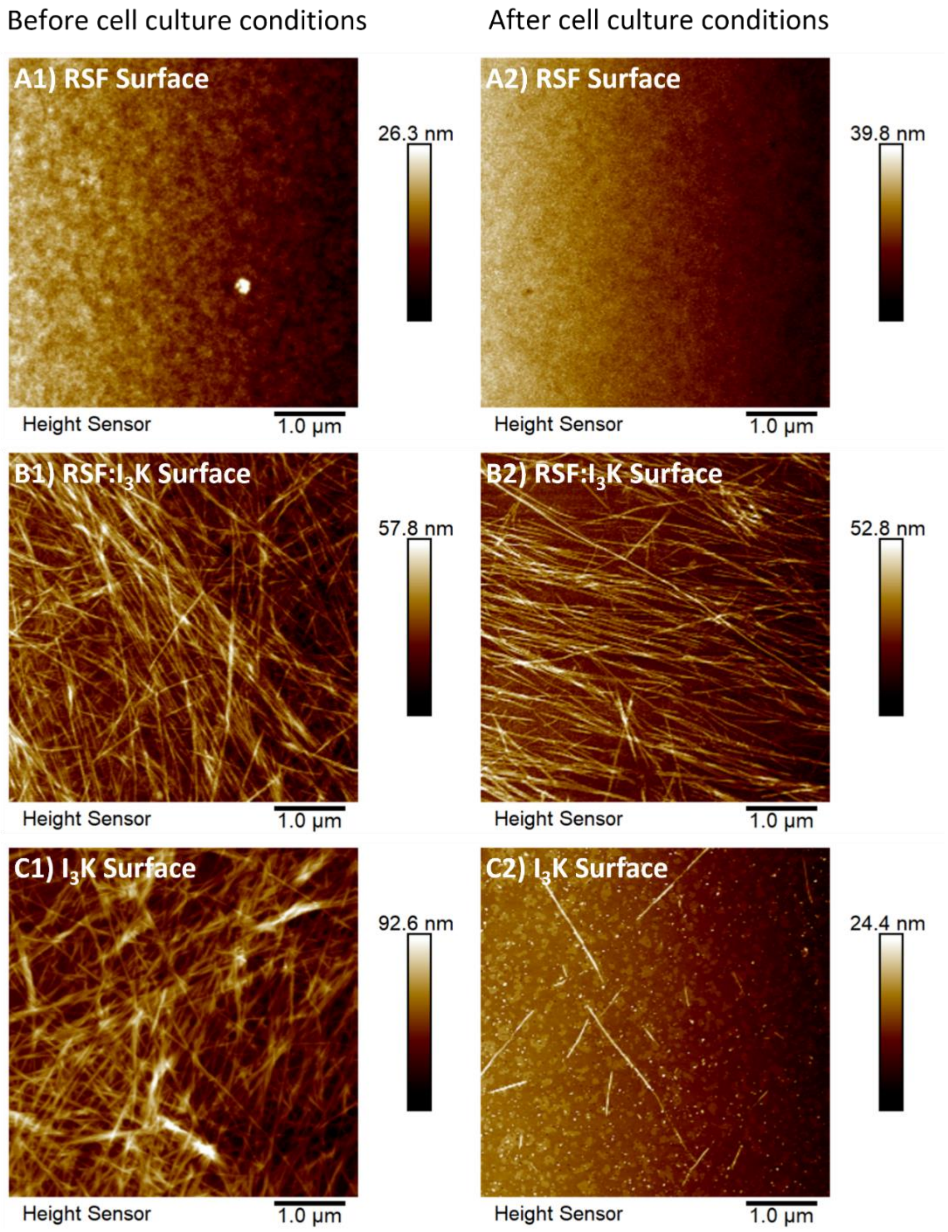

Figure 33. AFM surface topography micrographs of A1) RSF surface before cell culture conditions, A2) RSF surface after cell culture conditions; B1) RSF:I_3K surface before cell culture conditions, B2) RSF:I_3K surface after cell culture conditions; C1) I_3K surface before cell culture conditions, C2) I_3K surface after cell culture conditions. The concentration of RSF was 40 mg/mL and I_3K was 5 mg/mL, this was left to self-assemble for 7 days prior to coating.

cover glasses. The hydrophobicity and hydrophilicity of the different surfaces can affect how the I_3K spreads on the surface during the spin coating process. This will be analysed in the next section, but cover glass is more hydrophobic than the RSF surface and therefore, I_3K will be expected to spread less on cover glasses than on RSF surfaces [185] and the thickness, or height, of the coating will be higher as seen in Figure 33 C1. However, this decreases drastically after being in deionised water in cell culture conditions. Since there is no interaction between the cover glass and the I_3K nanofibres, these will detach from the cover glass and therefore the final maximum height is much lower (Figure 33 C2).

4.4.2. Contact angle

To evaluate how the I_3K coating affected the surfaces, water contact angle measurements were carried out. This measured the wettability of a surface, and it was related to the hydrophobicity/hydrophilicity of the surface as seen in Figure 34. Wettability is an important factor to determine how cells will behave and adhere on these surfaces [186, 187].

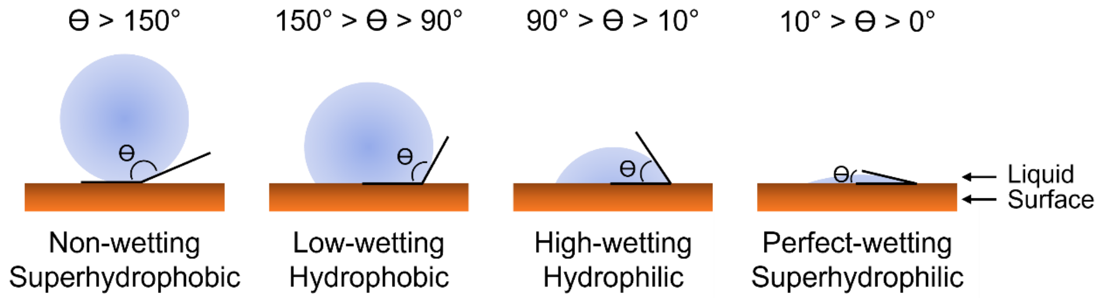

Figure 34. Schematic representation of different water contact angle, ϴ (°) and its classification of superhydrophobic, hydrophobic, hydrophilic and superhydrophilic. Adapted from the work of Zhang, B. and W. Xu [188].

In this case, the surface of a cover glass was coated with the RSF solution first, and this was then coated with the I_3K peptide solution. Therefore, a change in the water contact angle would indicate the surface modification has taken place.

First, the average contact angle of the cover glass was 80°, as shown in Figure 35A and B. Moreover, after the cover glass was exposed to air for 24 h, the contact angle remained constant at 80°, proving this surface was not affected by that. Then, the cover glass was coated with the I_3K solution at day 0, 1,3, 5, and 7 of self-assembly time to check the average contact angle of the peptide coating. In this case, the average contact angle decreased significantly from that of the non-coated cover glass (80°) to 6-7° when coated with the I_3K solution as seen in Figure 35A. This can be considered as a superhydrophilic surface [188] since the contact angle is less than 10°. This was as expected considering how the I_3K peptide self-assembled with all the lysine side chains, hydrophilic groups, facing outwards from the nanotubes [176, 178]. However, there was no significant difference between any of the I_3K groups meaning the hydrophilic groups were readily available since day 0.

However, the main interest was on the RSF and RSF:I_3K coated cover glasses, as these are the samples that would be used as scaffold for cell culture. The contact angle of the cover glass decreased from 80° to 59° when it was coated with the RSF solution as seen in Figure 35B. It is worth mentioning that all RSF surfaces were treated in the last step of the coating procedure with a 95% ethanol solution to change the conformation of the RSF from silk I (random coil, soluble state) to silk II (β-sheets, insoluble state). On the other hand, when the silk surface was left exposed to air for 24 h the contact angle was maintained at 59° as seen in Figure 35C, suggesting no change to the surface. Mohd et al. [131] measured the contact angle of different SF samples: SF, methanol-treated SF, ethanol-treated SF and water annealed SF. They concluded that the post-treated films had an increased water contact angle due to the increase in β-sheet content. This made the treated SF more hydrophobic (ϴ was 52-57°) compared to the untreated SF (ϴ was 21°). Recent studies are looking into the possibility of tuning the hydrophobicity/hydrophilicity of SF through covalent links to be used in different applications [189].

On the other hand, when I_3K was used to coat the RSF surfaces, the contact angle decreased from 59° to 12 - 16°. This means that overall, the hydrophilicity of the RSF:I_3K surfaces increased compared to the RSF or to the cover glass. However, when these surfaces were left exposed to air for 24 h, the surfaces became more hydrophobic increasing their contact angle from 12 - 16° to 37 - 40° (Figure 35C), meaning that the peptide might be degrading. Therefore, it is important to use these surfaces as quickly as possible after coating. Moreover, no difference was found amongst the different self-assembled I_3K coatings (0, 1, 3, 5 and 7 days incubation time) when analysed immediately after coating or 24 h after (Figure 35 B and C). Finally, the morphology and spreading of the water contact angle droplet on all surfaces can be seen in Figure 36.

A) I_3K surfaces

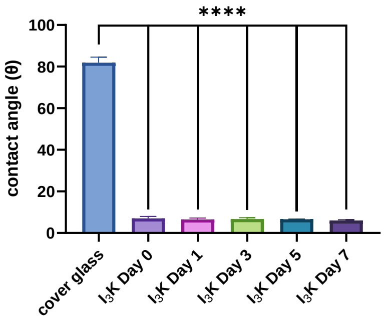

B) RSF:I_3K surfaces

C) RSF:I_3K surfaces after 24h

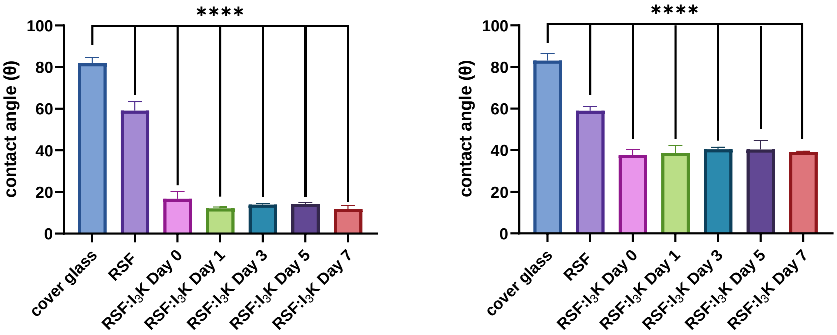

Figure 35. Water contact angle (Θ) for each surface: A) I_3K coated cover glasses, B) RSF:I_3K coated cover glasses and C) B) RSF:I_3K coated cover glasses after 24 h exposure to air. RSF was used at a concentration of 40 mg/mL and I_3K has a concentration of 5 mg/mL in 20 mM HEPES buffer (pH 6). I_3K solution was left to self-assemble for 0, 1, 3, 5 and 7 days prior to being spun coated. One-way factor analysis of variance (ANOVA) was performed. P values of *$P < 0.05$, **$P < 0.01$, ***$P < 0.001$ and ****$P < 0.0001$ were considered as significant.

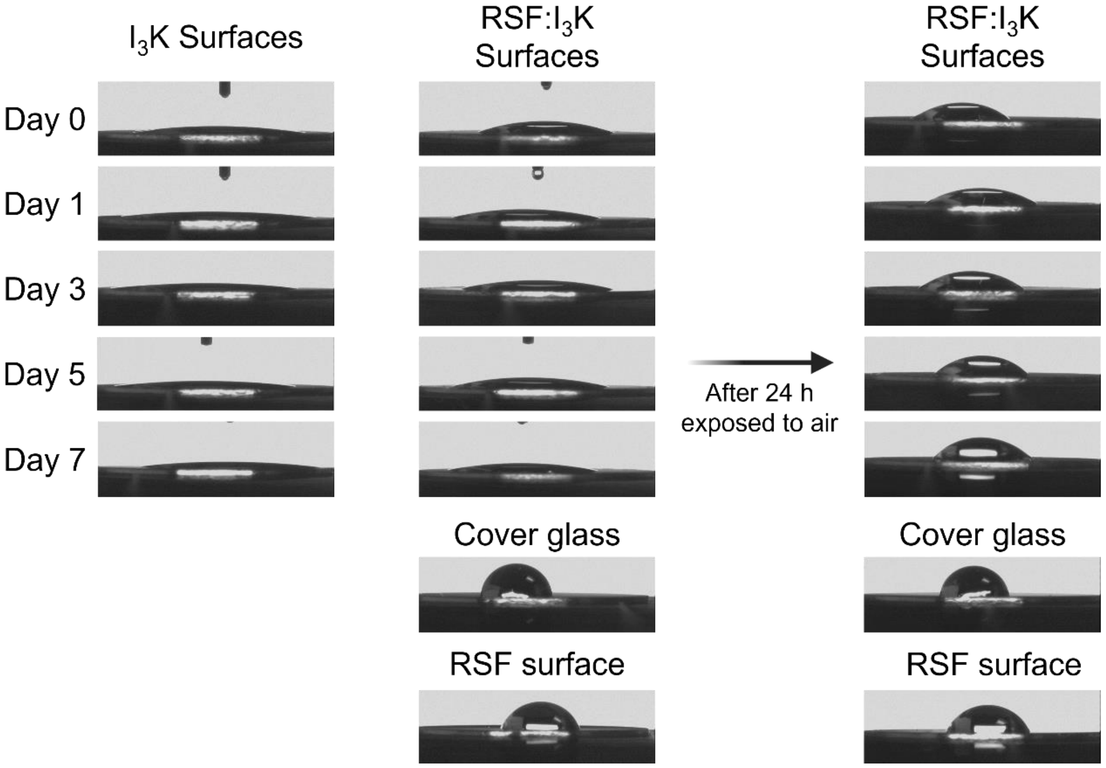

Figure 36. Water droplet shapes in all analysed surfaces: I₃K coated cover glasses, RSF:I₃K coated cover glass, cover glass, RSF coated cover glass. Surfaces of RSF:I₃K, RSF and cover glass were also analysed after 24 h to see how the surface changed. RSF was used at a concentration of 40 mg/mL and I₃K has a concentration of 5 mg/mL in 20 mM HEPES buffer (pH 6). I₃K solution was left to self-assemble for 0, 1, 3, 5 and 7 days prior to being spun coated.

4.4.3. *In vitro* studies with PC12-Adh neuronal-like cell line

In the same way that it was done in Chapter 3, cell attachment and metabolic activity of PC12-Adh cells was assessed on the RSF:I₃K coated cover glasses. To do this, RSF solution (40 mg/mL) was spun coated onto 13 mm diameter cover glasses and its conformation changed from soluble random coils to insoluble β-sheets. Then the RSF surface was coated with a 5 mg/mL I₃K solution in 20 mM HEPES buffer (pH 6) via spin coating as described before. These surfaces were sterilised via UV irradiation for 30 min and then used for the following assays. Previously, Wu et al. [86] explored the self-assembly properties of IKVAV peptides into nanofibers and their subsequent effects on PC12 cell behaviour. They demonstrated that the nanofibers not only provide a conducive environment for cell adhesion but also enhance the neurite outgrowth of PC12 cells, which are commonly used as a model for neuronal differentiation. Therefore, in this chapter PC12 cells were used to prove the potential application of RSF functionalised with I₃K as a suitable biomaterial for nerve regeration.

Cell attachment studies – crystal violet assay

Cell attachment on RSF obtained from degumming during 90 min, dissolved using Ajisawa's method and then, dialysed using 12 kD MWCO tubes proved to have poor cell attachment according to the results obtained in Chapter 3. To improve cell adhesion, RSF was coated with the self-assembled synthetic peptide I_3K. Crystal violet assay was used to assess cell attachment on these coated surfaces. The chemical used in this assay; crystal violet (empirical formula $C_{25}H_{30}ClN_3$), chemical structure can be seen in Figure 37A. The assumption that all cells attached to the surfaces are alive while all dead cells have detached is made. Therefore, this is proportionate to the overall number of cells present on the sample. However, since this chemical binds to proteins in the cells and our surfaces are made up of proteins/peptides, crystal violet would bind to this as well as seen in Figure 37B and C. For this reason, a blank with no cells was used.

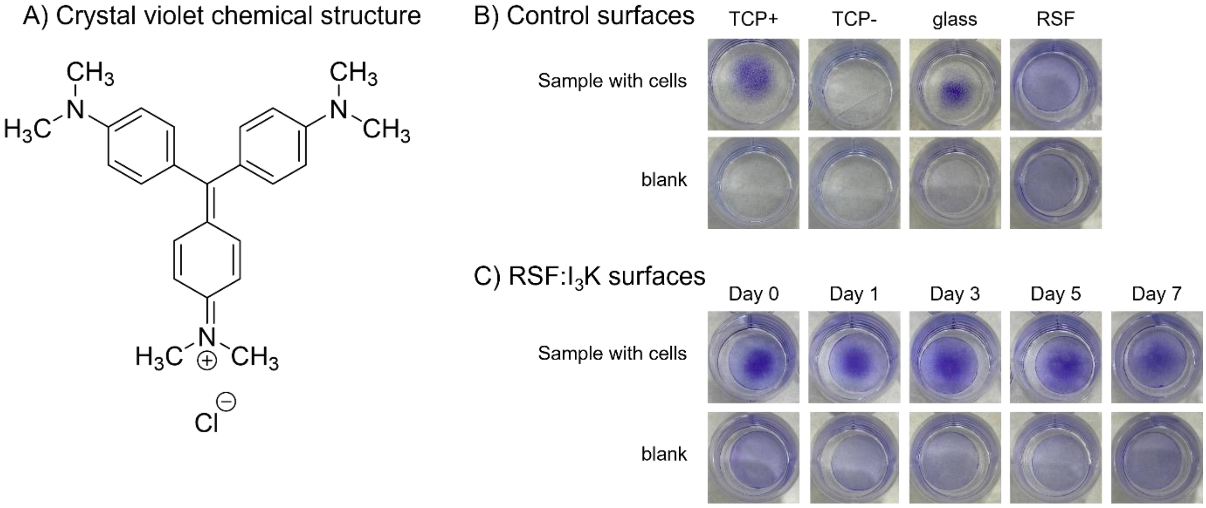

Figure 37. A) Chemical structure representation of crystal violet compound (made with ChemDraw); B) photographic images of controls (TCP+, TCP-, cover glass and RSF) with and without PC12-Adh cells, stained with crystal violet; C) photographic images of samples (RSF coated with I_3K after 0, 1, 3, 5 and 7 days of self-assembly) with and without PC12-Adh cells, stained with crystal violet.

The poor cell adhesion on RSF surfaces has also been proven elsewhere [2, 13]. Here, Dhyani et al., improved the cell adhesion on RSF using graft polymerization of poly (acrylic acid). Apart from synthetic polymers, natural proteins present in the extracellular matrix such as fibronectin, laminin or collagen have been also used with silk to improve cell attachment [27, 46, 47, 158, 190].

The glycoprotein fibronectin is naturally involved in adhesion, growth, and differentiation of cells within the body. It has been successfully used in combination with SF fibres improving cell adhesion and viability [27]. The principal integrin-binding domain present in the protein fibronectin is RGD, where "R" is amino acid arginine, "G" glycine, "D" aspartic acid. Its combination with RSF has improved the cell adhesion in tissues such as bone [49, 191], tendon [91] or corneal [90]. Similarly, the protein laminin and its primary domain for bioactivity IKVAV, where "I" represents amino acid isoleucine, "K" lysine, "V" valine and "A" alanine; has also being used effectively to improve adherence of neuronal cells [46, 86, 87].

However, polylysine remains one of the most used proteins used to improve cell attachment in cell culture [192-194] and, more specifically, in neural tissue [157-159, 195]. Polylysine is positively charged at pH 7.0, this creates cationic active sites that can interact with other negatively charged polymers, proteins, or cells. The small synthetic peptide, I_3K, can provide the same positive charge of the lysine groups to enhance cell attachment in the same way polylysine does. For this reason,I_3K cand be a good substitute for polylysine in cell culture.

In Figure 38, the cell attachment on RSF surfaces is significantly lower than on the positive control (TCP). This was already documented and explained in Chapter 3. On the other hand, cell attachment using I_3K self-assembled for 0 and 5 days is not significantly different from that of the positive control. On the other hand, when coating with I_3K self-assembled for 1 and 3 days, the attachment is higher than that of the positive control. Lastly, for the peptide self-assembled for 7 days, the cell attachment seems to go down compared to all the other I_3K groups and the positive control.

Studies carried out by this research group [196, 197] with the synthetic peptide I_3K and I_3QGK (Ac-I_3QGK-NH_2), a similar peptide amphiphile, have previously shown improvement on cell attachment. However, these studies only considered self-assembled peptides for 7 days and did not investigate the possibility of using less incubation time and how this could affect cell adhesion.

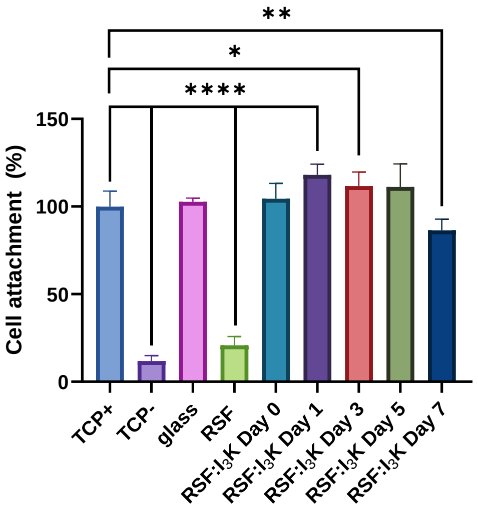

Figure 38. Graphical representation of cell attachment (%) relative to the positive control (TCP+) obtained with crystal violet assay. Results from positive control (TCP+), negative control (TCP-), uncoated cover glass, RSF coated cover glass and RSF:I_3K coated cover glass with I_3K self-assembled for 0, 1, 3, 5 and 7 days are shown. RSF was used at a concentration of 40 mg/mL and I_3K has a concentration of 5 mg/mL in 20 mM HEPES buffer (pH 6). One-way factor analysis of variance (ANOVA) was performed. P values of $*P < 0.05$, $**P < 0.01$, $***P < 0.001$ and $****P < 0.0001$ were considered as significant.

Fluorescence imaging of cell seeded on RSF:I_3K surfaces

Apart from quantitatively assessing cell attachment, it is also important to see the morphology of the cells that are attached to the surfaces. PC12-Adh cells were stained with DAPI (nuclei stain, blue) and FITC-Phalloidin (F-actin stain, green) as seen in Figure 40. Here, cells were present in all the samples except for the RSF coated cover glass. Moreover, in the RSF:I_3K day 5 and day 7 of self-assembly, there was evidence of more cells with a round morphology instead of spreading their cytoplasm to completely attach. Cells go through different adhesion phases as shown in Figure 39.

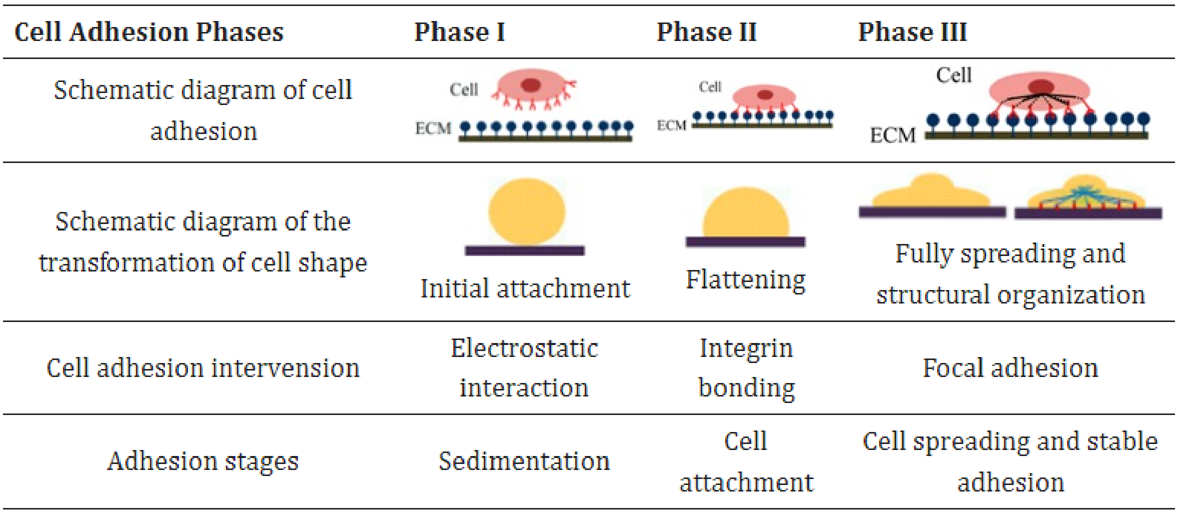

Cell Adhesion Phases	**Phase I**	**Phase II**	**Phase III**
Schematic diagram of cell adhesion			
Schematic diagram of the transformation of cell shape	Initial attachment	Flattening	Fully spreading and structural organization
Cell adhesion intervension	Electrostatic interaction	Integrin bonding	Focal adhesion
Adhesion stages	Sedimentation	Cell attachment	Cell spreading and stable adhesion

Figure 39. Different cell adhesion phases *in vitro*. Reproduced from the work of Khalili, A.A. and M.R. Ahmad [198].

Cells that remain in Phase I have not achieved integrin bonding and are considered as sedimented cells rather than truly attached cells. These round cells are more present when the self-assembled I_3K peptide has been incubated for longer periods of time , 5 days (Figure 40E) and 7 days (Figure 40F), meaning the type of cell adhesion is weaker. On the other hand, day 0 (Figure 40B) presents a mixture of fully adhered cells and round sedimented cells. Days 1 (Figure 40C) and 3 (Figure 40D), however, show that most of the cells are fully spread and only a few have a round morphology. Lastly, the controls (Figure 40G and H) show a monolayer of fully spread cells. However, while this may be optimal for cells such as fibroblasts or osteoblasts, amongst others, a full layer of nerve cells prevents them from differentiating properly, fully spread single nerve cells is the best arrangement for them.

While it has been theorised that cells attach better to surfaces that have a contact angle between 40 - 70° [186, 187], hydrophilic surfaces are better suited to promote differentiation in cells [199, 200].

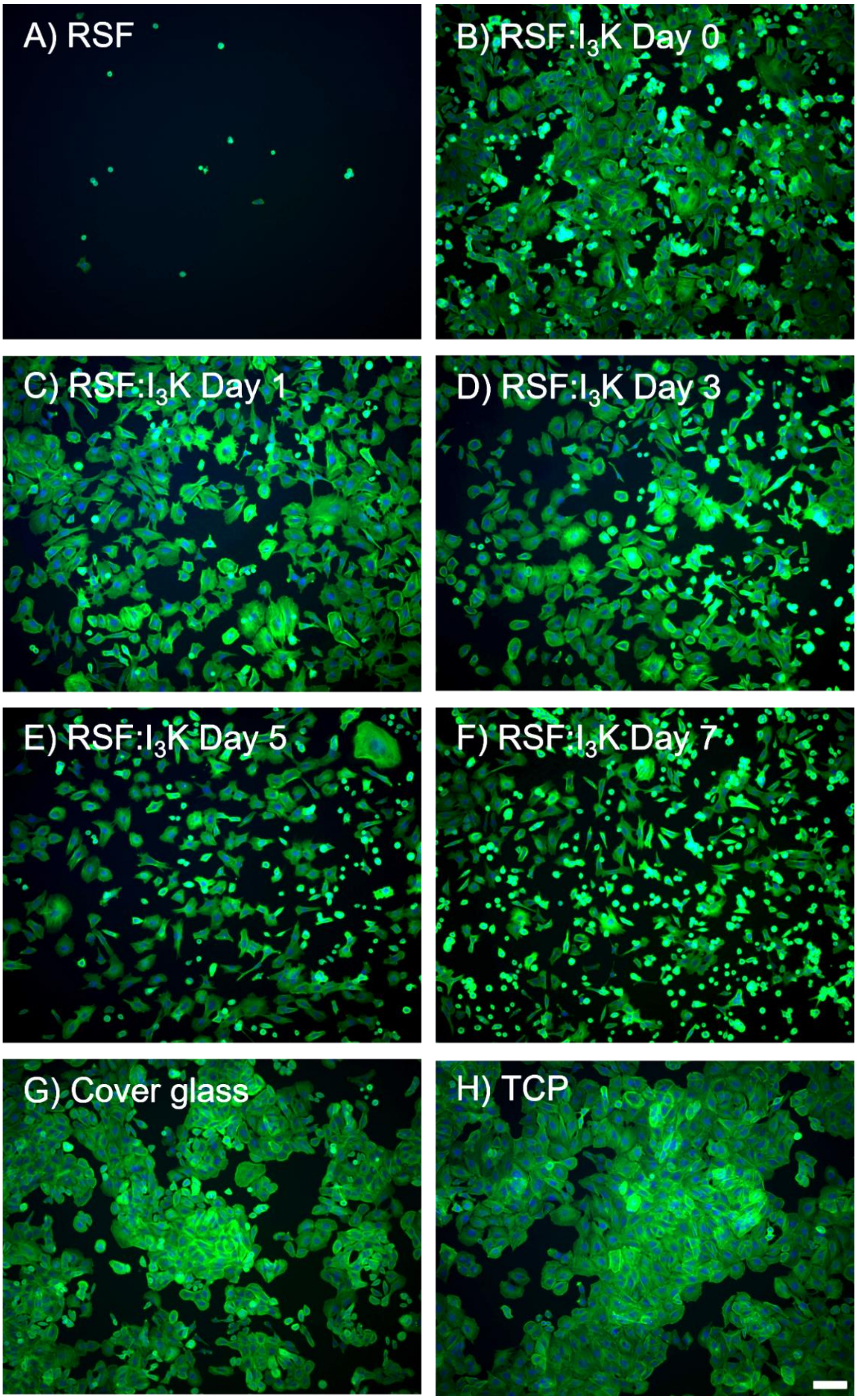

Figure 40. Fluorescent image of PC12-Adh cells on A) RSF coated cover glass, B) RSF:I_3K coated cover glass day 0 of self-assembly, C) RSF:I_3K coated cover glass day 1 of self-assembly, D) RSF:I_3K coated cover glass day 3 of self-assembly, E) RSF:I_3K coated cover glass day 5 of self-assembly, F) RSF:I_3K coated cover glass day 7 of self-assembly, G) uncoated cover glass and H) tissue culture plastic (TCP). Scale bar is 100 µm.

Cytocompatibility studies – resazurin/resorufin assay

Cytocompatibility of these RSF:I_3K coated cover glasses needs to be assessed. The metabolic activity of the cells can be evaluated via the resazurin/resorufin reduction reaction mediated by the aerobic respiration in the mitochondria of the cells. This gives an indication of the viability of cells and, therefore, of the cytocompatibility of the scaffolds. Two different approaches were used for this method. First, scaffolds were left submerged in media and then this media was used to grow cells attached to the tissue culture plastic, this helped determine if there was something leaching from the scaffolds that can be harmful to the cells. Second, to quantify the direct metabolic activity of cells growing directly on the surface of the scaffolds.

Figure 41 A shows the results for the indirect assay. The metabolic activity of cells from glass and RSF:I_3K day 0 was significantly lower than that of the positive control. Because I_3K was used right after dissolution (day 0), it had a smaller nanotube structure as seen in the AFM scans in Figure 32 B. Moreover, there may be electrostatic interaction between the nanotubes which makes them detach more easily from the RSF surface and leach to the media, therefore, where they may be toxic to cells. It was established that I_3K nanotubes had a similar structure to that of the cationic protein polylysine. This protein has been used to successfully improve cell attachment before [157-159, 192, 195]. However, it has also been proven that high concentrations of unbound polylysine can be toxic to the cells [201, 202]. On the other hand, I_3K self-assembled for 3 or more days did not show any decrease in metabolic activity. This means that even if some of the I_3K is leached into the media, it does not become toxic to the cells.

However, when assessing the direct metabolic activity of cells growing on the scaffolds, all samples present a significantly lower metabolic activity than the positive control (TCP+). As seen previously in the fluorescent images of Figure 40, not all the cells attached to the RSF:I_3K surfaces have fully spread and some of them are only slightly attached via electrostatic interaction. These would not be metabolically active.

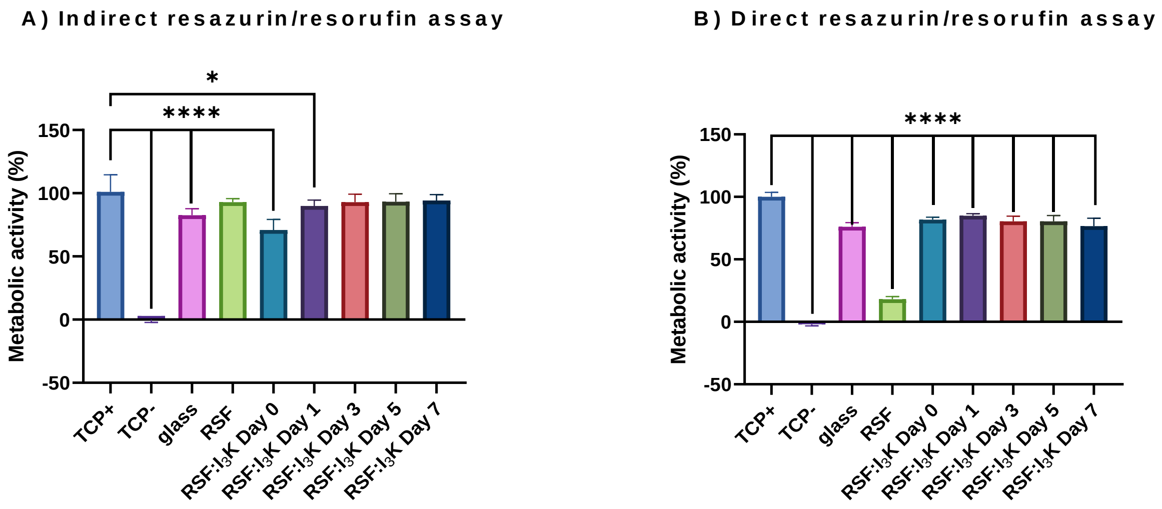

Figure 41. Graphical representation of metabolic activity (%) relative to the positive control (TCP+) obtained with A) indirect resazurin/resorufin assay, B) direct resazurin/resorufin assay. Results from positive control (TCP+), negative control (TCP-), uncoated cover glass, RSF coated cover glass and RSF:I_3K coated cover glass with I_3K self-assembled for 0, 1, 3, 5 and 7 days are shown. RSF was used at a concentration of 40 mg/mL and I_3K has a concentration of 5 mg/mL in 20 mM HEPES buffer (pH 6). One-way factor analysis of variance (ANOVA) was performed. P values of *P < 0.05, **P < 0.01, ***P < 0.001 and ****P < 0.0001 were considered as significant.

4.5. Conclusion

In this chapter, cell attachment on a previously non-fouling surface derived from the natural silk fibroin protein has been improved by the addition of a synthetic peptide, Ac-I_3K-NH_2. The chemical structure of this peptide made up of three units of the hydrophobic amino acid isoleucine, I, and one unit of the cationic hydrophilic amino acid lysine, K, suggests an amphiphilic peptide capable of self-assemble under the right conditions. Although, this self-assembly behaviour has been previously studied elsewhere [176, 203], here, the formation of nanotubes when I_3K is dissolved at pH 6 in 20 mM HEPES buffer was analysed via AFM. Different self-assembly times were assessed and scanned, all of them showed the formation of long (> 1 mm) nanotubes after 1 day of incubation. The self-assembly process occurring in aqueous solution allows all the hydrophilic lysine group to be facing outwards of the nanotube structure. This allowed the positively charged I_3K peptide to coat the negatively charged RSF surface via electrostatic interactions at pH 6. Moreover, it was demonstrated that this interaction was strong enough, so the peptide remained coupled with the silk after 7 days of incubation in cell culture conditions. Therefore, making the RSF:I_3K coated cover glasses an ideal candidate for cell culture.

Finally, cell attachment and cytocompatibility of these surfaces were assessed. While the use of I_3K to improve cell attachment has been previously studied by our research group [197], the peptide was only used after 7 days of self-assembly. In this case, different incubation times (0, 1, 3, 5 and 7 days) were studied to see the relevance of this in tissue engineering applications. Cell attachment increased significantly when I_3K was incubated for 1 and 3 days, decreasing for longer times. All samples showed a mixture of fully spread cells and sedimented cells. On the other hand, indirect cytocompatibility assays showed that for incubation periods longer than 3 days, no decreased metabolic activity was detected due to the samples leaching into the media. On the other hand, direct metabolic assay showed a significant decrease in all samples, possibly due to the fact that some of the cells were not fully attached and could not carry out metabolic activities.

Overall, it has been proven that I_3K is an ideal candidate to improve cell adhesion on scaffolds for tissue engineering applications. However, the importance of scaffold orientation, is really important in the field of nerve regeneration. While in this chapter the overall cell adhesion properties of the I3K-RSF surfaces were investigated, in the next chapter, I_3K will be micropatterned via drop-on-demand (DoD) inkjet printing to further direct cell attachment and to mimic the microenvironment of nerve cells.

Chapter 5. Micropatterning of I_3K peptide on RSF surface to guide PC12-Adh attachment and proliferation

5.1. Introduction

Inkjet printing is a very adaptable technique that can be used to create both 2D features and 3D structures. This technique allows high precision deposition of small amounts of ink, usually in the picolitre range. Inkjet printing can be divided into two big groups depending on the type of jetting, continuous or drop-on-demand (DoD) (Figure 42). In continuous inkjet printing, the printhead generates a continuous jet of ink. On the other hand, the DoD only produces a drop when it is required; for this, two different methods can be used, thermal or piezoelectric DoD inkjet printing.

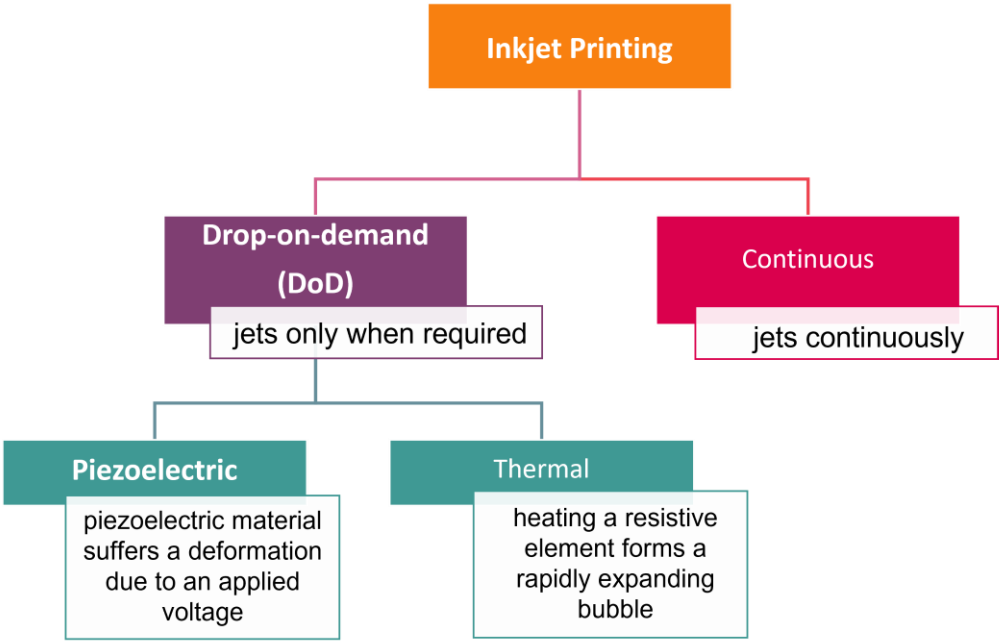

Figure 42. Schematic representation of the types of inkjet printing.

Thermal DoD printing uses a special printhead equipped with a heating element, usually a resistor. A current is applied which makes the resistor heat which in turn vaporises a small volume of the ink forming a bubble. This bubble keeps expanding which pushes the ink out of the nozzle of the printhead, then as it cools down, the bubble generates a vacuum, taking ink from the ink reservoir and filling the bubble. This keeps repeating every time a drop is needed.

This method requires an ink that contains a volatile element so it can form the bubble, and the ink cannot be degraded or affected by the heat. This method has been successfully used to print live cells [204, 205] and other materials such as proteins [206]. However, cell survivability and protein degradation can be affected by the harsh temperature and pressure conditions inherent to the method.

On the other hand, a piezoelectric approach can be used. In the case of MicroFab printheads, the piezoelectric material in an annular element that surrounds a tube made of glass as can be seen in Figure 43A . When a voltage is applied to the electrodes an electrical field is produced which, in turn, causes the piezoelectric material to deform. Depending on the polarity of the voltage applied the deformation can happen in two directions, radially and axially. This deformation is transferred from the piezoelectric material to the glass through an epoxy bond creating a negative pressure (from the equilibrium). This travels through the liquid, i.e. bio-ink, in the form of an expansion acoustic wave that travels towards both the orifice and the supply end of the glass tube. It is at this latest point that it bounces back towards the orifice in the form of a compression wave (positive pressure in respect of the equilibrium). Thus, jetting a droplet from the orifice and quickly refilling with more ink from the reservoir. This removes the need for a volatile solvent to be added to the ink which reduces the cost. This method has also been used successfully to print cells [59, 207-211] or patterns of some biomaterials such as peptides and proteins [196, 197, 212].

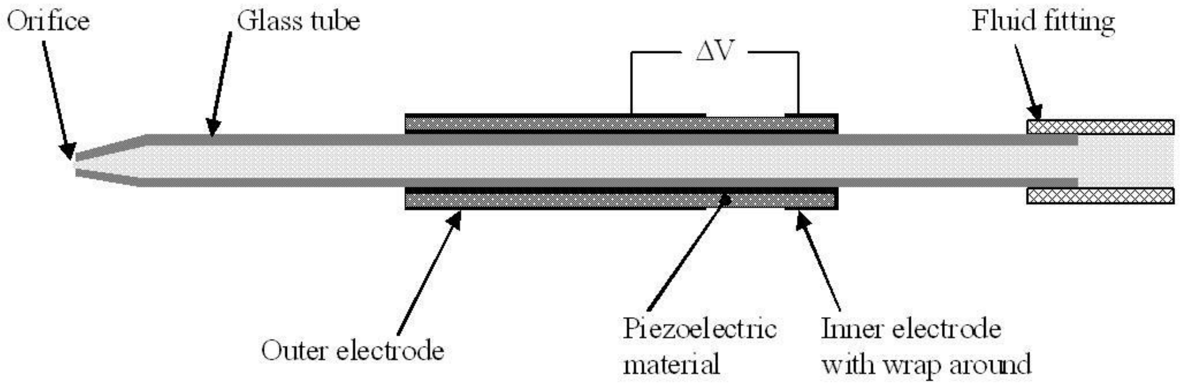

Figure 43. Schematic representation of the jetting device are reproduced from the manufacturer's website, MicroFab Technologies Inc., USA [213].

Spatially oriented micro features can be found in natural tissues such as parallel collagen fibrils in tendons, concentric circles (lamellae) in bones or longitudinally aligned axons in nerves [214]. Moreover, topographical features such as roughness, micropores and mechanical properties, or chemical cues such as surface energy, wettability, or bioactive molecules, can affect cell behaviour such as attachment, migration, or differentiation [215, 216]. For example, Cai et al. [217] used inkjet printing to create a gradient pattern of laminin that showed that cell adhesion was dependent on the laminin concentration of the gradient. On the other hand, Ker et al. [218] demonstrated that differentiation into bone and tendon can be promoted by the addition of spatially defined patterns. This can be of great interest to the field of organ-on-a-chip [219]. In particular, the patterning of neuronal cells to create complex patterns or arrays of multiconnected neurons is of special interest to the fields of bioelectronics, neurological implants, or biosensors [219, 220].

5.1.1 Micropatterning via inkjet printing of self-assembling peptides (SAP)

Self-assembling peptides have emerged as a promising class of bioinks for inkjet printing due to their unique structural characteristics and biological compatibility as described in Chapter 4. Use of novel amphiphilic peptide to improve cell attachment on non-fouling RSF surfaceGuo et al. [212] demonstrated the versatility of peptide inks for coding cell micropatterns, which enabled the development of functional architectures suitable for regenerative medicine. This also showed the inherent ability of SAP materials to recreate the dynamic complexity of biological tissues. Moreover, Li et al. [221] showed how aligned scaffolds with biomolecular gradients can be flexibly produced, optimizing conditions for neuronal repair, particularly in regenerative medicine contexts. The precise patterning of cells within scaffolds reinforces the interaction between scaffold topography and cellular behaviour, ultimately supporting the regeneration of nerve tissue.

The mechanisms underlying the self-assembly of peptides contribute significantly to the effectiveness of inkjet printing techniques. Hart et al. [222] explored the use of supramolecular networks, illustrating how sequential deposition can enhance the organizational structure of printed materials. This approach allows for controlled alignment and spatial distribution of peptides, which can optimise the physiological responses of different cells and tissues.

The integration of inkjet printing with self-assembled peptides for tissue engineering presents a promising trajectory that combines innovative material properties with advanced printing techniques. The synergistic effects of these self-assembling peptides enable the creation of bioactive, structured scaffolds that can support cellular functions and tissue regeneration, thus enhancing outcomes in biomedical applications. This has already being demonstrated by our own research group [196]. Here, Sun et al. showed that combining the synthetic peptide I_3QGK with silk scaffolds can help guiding the growth and attachment of neuronal cells.

5.2. Aims and objectives

This chapter explores the use of drop-on-demand (DoD) inkjet printing to create I_3K micropatterns on RSF surfaces, aiming to enhance neuronal cell adhesion and alignment. It investigates the optimisation of these patterns to promote cell recognition and differentiation of PC12-Adh cells. Additionally, the study examines the role of nerve growth factor (NGF) in supporting neuronal differentiation on the printed patterns.

The aims of this chapter are:

1. Print the peptide I_3K via drop-on-demand (DoD) inkjet printing a micropattern on RSF surfaces
2. Assess the cell attachment and differentiation of PC12-Adh growing on those patterns

The objectives of this chapter are:

1. Use DoD inkjet printing to create I_3K micropatterns to promote adhesion of the neuronal cell line PC12-Adh
2. Optimise those patterns so they can be recognised by the cells to promote cell alignment
3. Differentiate PC12-Adh cells growing on those patterns with and without the help of nerve growth factor (NGF)

5.3. Materials and methods

5.3.1. Materials

Details of the materials used were described in Chapter 2 Section 2.1.

5.3.2. Silk degumming and dissolution

The RSF solution preparation process was described in Chapter 2 Section 2.2.

B. mori silk cocoons were degummed for 90 min, dissolved using Ajisawa's method and dialysed using a 12 kD MWCO dialysis tube. RSF solution was then diluted to 40 mg/mL when needed.

5.3.3. Dissolution of peptide I_3K

The dissolution of I_3K peptide was described in Chapter 2 Section 2.7. The peptide was dissolved at a concentration of 5 m/mL and left to self-assemble for 3 days at room temperature. Then diluted to 1 mg/mL or 0.5 mg/mL right before printing.

5.3.4. Preparation of RSF surfaces via spin coating

The spin coat process was described in Chapter 2 Section 2.8. RSF solution was diluted to a concentration of 40 mg/mL. Here, 10x10 mm square cover glasses 1.5 mm thickness (Agar Scientific, UK)

5.3.5. Contact angle

The contact angle process was described in Chapter 2 Section 2.9.2. Here, a 5 µL drop of either deionised water or of I_3K solution (0.5 mg/mL) were used.

5.3.6. Micropatterning via drop-on-demand inkjet printing

Drop-on-Demand (DoD) inkjet printing process was described in Chapter 2 Section 2.10. Here, bioink was made of 1 or 0.5 mg/mL I_3K self-assembled for 3 days. Ink is prepared fresh every time.

5.3.7. *In vitro* studies with PC12-Adh neuronal-like cell line

General cell culture

General cell culture procedure as well as general culture media preparation were described in Chapter 2 Section 2.5.1.

Differentiation studies

Differentiation of PC12-Adh cell line was described in Chapter 2 Section 2.5.4.

5.3.8. Fluorescence Microscopy and analysis of cells

Staining and fluorescence imaging procedures were described in Chapter 2 Section 2.6.1. and Chapter 2 Section 2.6.3.

5.3.9. Statistical analysis

Data were presented as mean ± standard deviation (N = 3 or otherwise mentioned). One-way or two-way factor analysis of variance (ANOVA) was performed for all multiple group experiments. P values of $^{*}P < 0.05$, $^{**}P < 0.01$, $^{***}P < 0.001$ and $^{****}P < 0.0001$ were considered as significant. The statistical analysis was performed using Prism GraphPad software. Equality was confirmed by Tukey's multiple comparison test.

5.4. Results and Discussion

5.4.1. Printing of initial I_3K micropatterns on RSF surfaces via drop-on-demand inkjet printing

To print micropatterns of I_3K (1 mg/mL) a custom-made inkjet printer equipped with a piezoelectric printhead was used. This printhead has a glass nozzle with an orifice of 40 µm (Figure 44).

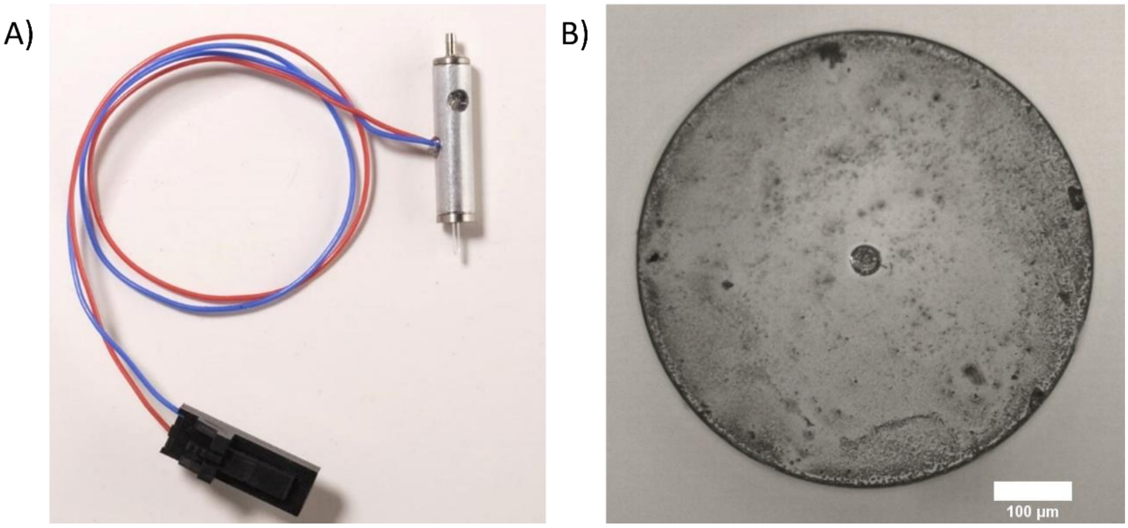

Figure 44. A) Image of the jetting device are reproduced from the manufacturer's website, MicroFab Technologies Inc., USA [213], B) Brightfield image of the 40 µm glass orifice (scale bar is 100 µm)

As mentioned before, the printhead device used in this study is equipped with a piezoelectric material that when subjected to a voltage pulse creates a pressure wave that forms and ejects a droplet from the orifice of the nozzle. This pulse waveform can be classified into single polar pulse (Figure 45A) and bipolar pulse waveform (Figure 45B) [223].

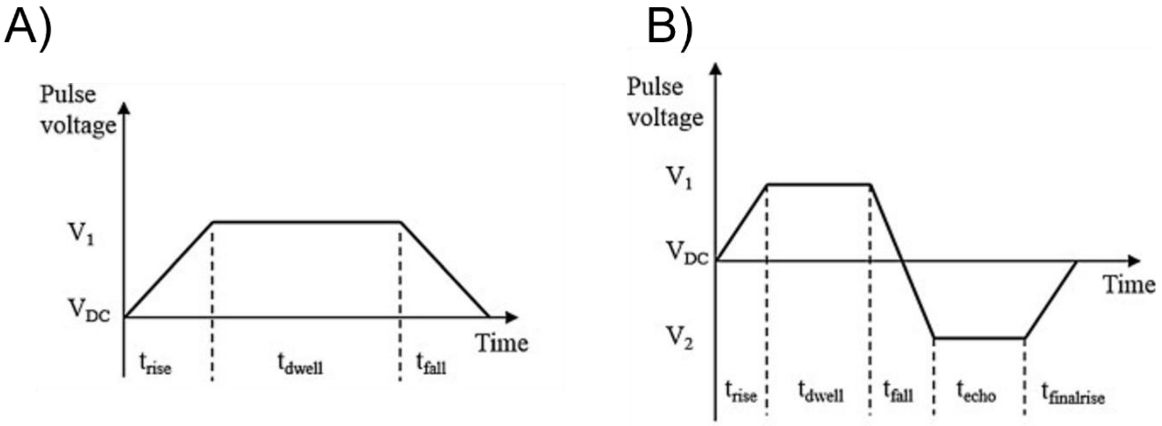

Figure 45. Schematic graphical representation of A) single polar pulse waveform and B) bipolar pulse waveform. Adapted from the work of Wu, C.-H. and W.-S. Hwang [223].

The printer is equipped with a camera and a strobe light. The strobe light frequency matches with the ink jetting from the nozzle which allows the camera to capture the droplet formation that usually occurs within the order of microseconds (µs). The use of stroboscopic photography to image the otherwise too fast droplet formation has previously been used [224, 225]. Figure 46A illustrates the time and voltage input parameters, and the waveform produced as a result of these parameters. Furthermore, Figure 45B shows the time lapse of the droplet formation using the set of parameters in Figure 45A.

However, Figure 46B shows that the droplet formation in this case consists of a tail that eventually breaks up into multiple satellite droplets. The jetting process is highly affected by viscosity and surface tension of the bioink, this can be described by the inverse of the Ohnesorge number (Oh) defined as Z,

$$Z = \frac{1}{Oh} = \frac{\sqrt{\rho\sigma L}}{\mu} = \frac{Re}{\sqrt{We}} \sim \frac{\sqrt{inertia \ \cdot surface\ tension}}{viscous\ forces}$$

Equation 3. Equation used to calculate the dimensionless constant Z and its relation to the dimensionless Ohnesorge number (Oh), Reynolds number (Re) and Weber number.

where

- μ is the dynamic viscosity of the liquid
- ρ is the density of the liquid
- σ is the surface tension
- L is the characteristic length, usually the drop diameter
- Re is the dimensionless Reynolds number

$$Re = \frac{\rho v L}{\mu}$$

Equation 4. Equation used to calculate the dimensionless Reynolds number (Re).

- We is the dimensionless Weber number

$$We = \frac{\rho v^2 L}{\sigma}$$

Equation 5. Equation used to calculate the dimensionless Weber number (We).

- v is the flow speed

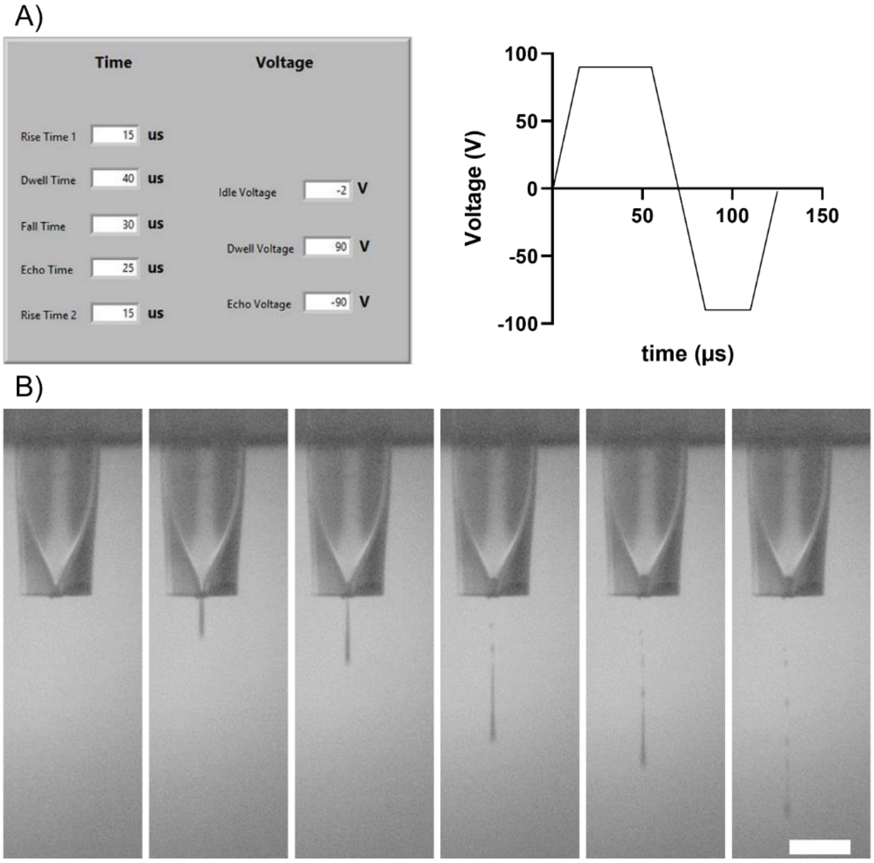

Time

Rise Time 1 15 us
Dwell Time 40 us
Fall Time 30 us
Echo Time 25 us
Rise Time 2 15 us

Voltage

Idle Voltage -2 V
Dwell Voltage 90 V
Echo Voltage -90 V

Figure 46. A) Time and voltage input parameters and the bipolar waveform obtained B) Strobe time lapse images of the I_3K (1 mg/mL) ink droplet being formed from a jetting device with a nozzle diameter of 40 µm. Scale bar represents 500 µm.

Initially, Fromm [226] reached the conclusion that Z > 2 was required to achieve stable droplets, this was later revised by Derby [227] to the range of 1 < Z < 10 (Figure 47). Low Z numbers imply high viscosity forces which mean more pressure is needed to eject a droplet or no jetting will occur. On the other hand, high Z numbers mean lower viscosity and the possibility of continuous flow or satellite droplet formation. Both cases will affect the final definition and quality of the printing. Current studies have established an optimised range of 2 < Z < 20 [228].

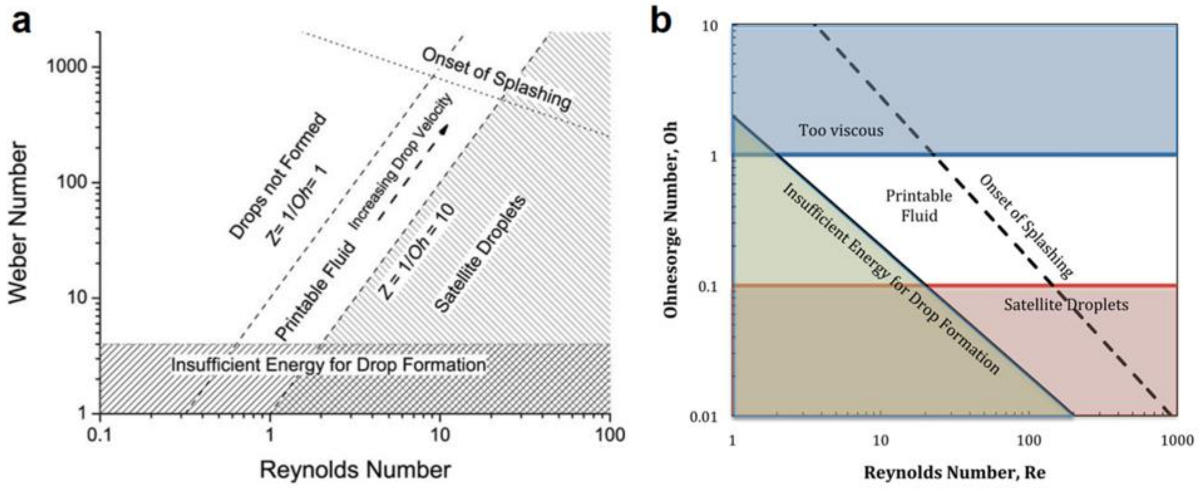

Figure 47. Theoretical operating regimes of inkjet printing based on the dimensionless numbers: Reynolds number (Re), Weber number (We) and Ohnesorge number (Oh). Reproduced from the works of Zhang, Y., et al. [224] and Lohse, D. [225].

However, these Z ranges have proven to be unreliable and liquids with other values have been successfully printed. If satellite formation occurs, there are different methods that can help minimise their impact in the quality of printing. Satellite droplets can re-join the main droplet because of a difference in velocity [224, 229]. Additionally, modifying the pressure in the ink chamber by modifying the piezoelectric waveform can also help with the reduction of satellite drops [230, 231]. On the other hand, addition of surfactants and polymers can also affect the printability of the ink. While most studies with added surfactants have focused on the post-printing relevance on the evaporation and coffee rings instead of the droplet formation, the addition of polymers with different molecular weights can drastically change the jet behaviour, even at lower concentrations [224].

However, Figure 48 shows that despite having a droplet formation accompanied by multiple satellite droplets the quality and definition of the printing remained unaffected.

In the present study, inks with a concentration of I_3K in HEPES buffer (20 mM, pH 6) higher than 1 mg/mL proved to be unreliable, unstable, and not duplicable. Therefore, a layer-by-layer approach was used to build up the I_3K peptide concentration on the RSF surface. In total, 11 parallel lines with one, three or five layers were printed; these micropatterns can be observed in Figure 48.

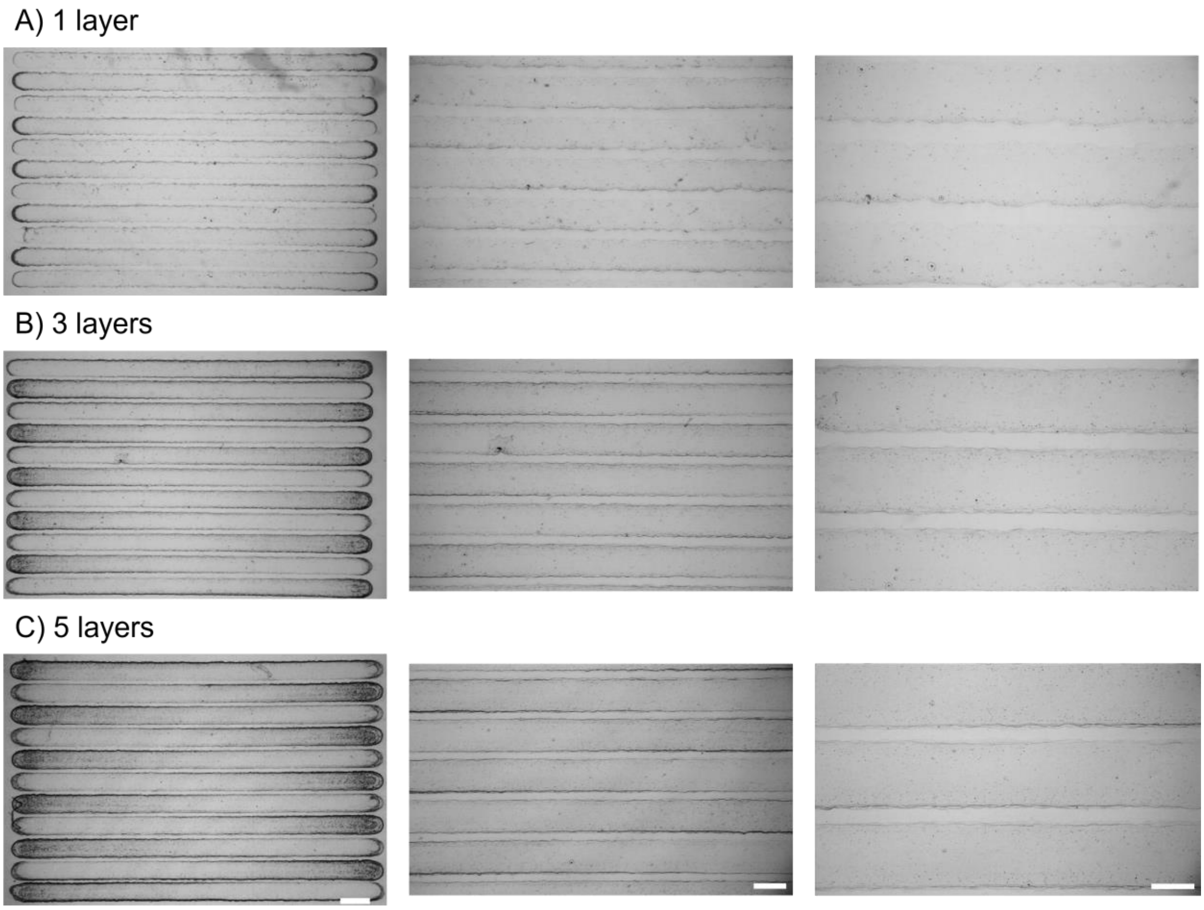

Figure 48. Brightfield images with different magnifications (2.5x, 5x and 10x) of I_3K micropatterns printed via drop-on-demand inkjet printed on RSF coated cover glasses. Different numbers of layers are printed: A) 1 layer, B) 3 layers and C) 5 layers. The scale bar of each column is 500 µm, 300 µm and 200 µm, respectively.

Moreover, the effect of the number of layers on the width of the lines was assessed. Results can be seen in Figure 49. Although the average width of the lines seemed to increase with the number of layers, statistical analysis showed there is no significant difference between them, with the width of the lines ranging between 271 µm ±14 for 1 layer, 288 µm ±11 for 3 layers and 294 µm ±6 for 5 layers.

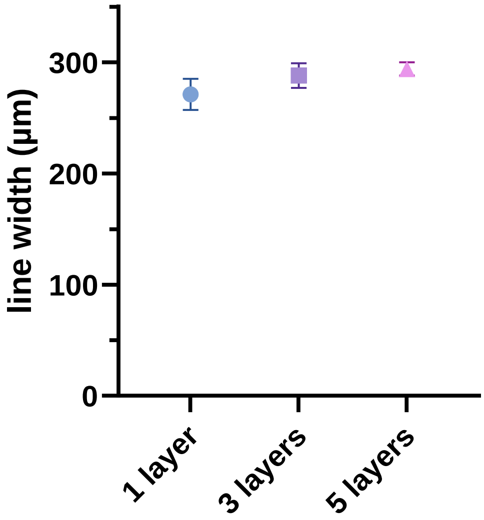

Figure 49. Graphical representation of the average width of the micropattern lines when they are printed with different numbers of layers. One-way factor analysis of variance (ANOVA) was performed. P values of *P < 0.05, **P < 0.01, ***P < 0.001 and ****P < 0.0001 were considered as significant.

5.4.2. *In vitro* studies with PC12-Adh neuronal-like cell line on initial micropatterns

These patterns were used as substrates for growing PC12-Adh cells. Figure 50 shows cells growing on the different samples. While growth and proliferation of cells was constrained to the patterned surface containing I_3K, on the positive controls (cover glass and TCP) cells grew without any constraints. Moreover, in the control samples, cells proliferated tightly in clumps or colonies showing good attachment and spreading, while cells in the micropatterns grew more as individual cells, acquiring a polygonal morphology with cytoplasmic extensions that could be related to differentiation and neurite growth.

The quantity of the peptide on the RSF substrate increases accordingly to the number of printed layers. Therefore, more peptide on the surface suggests a larger number of cells would attach to the printed micropatterns. As mentioned in Chapter 4, the coating of RSF with the I_3K peptide is based on the different overall charge of both materials. However, increasing the peptide concentration via this layer-by-layer approach would imply that a stronger electrostatic interaction occurs between the first layers and the RSF surface and consequently this interaction would decrease in the presence of a larger number of printed layers. Therefore, a limit of 5 printed layers was used as the maximum number of recognised patterns by the cells. This is further confirmed by the almost confluency of cells presented in the 5-layer pattern (Figure 50 C).

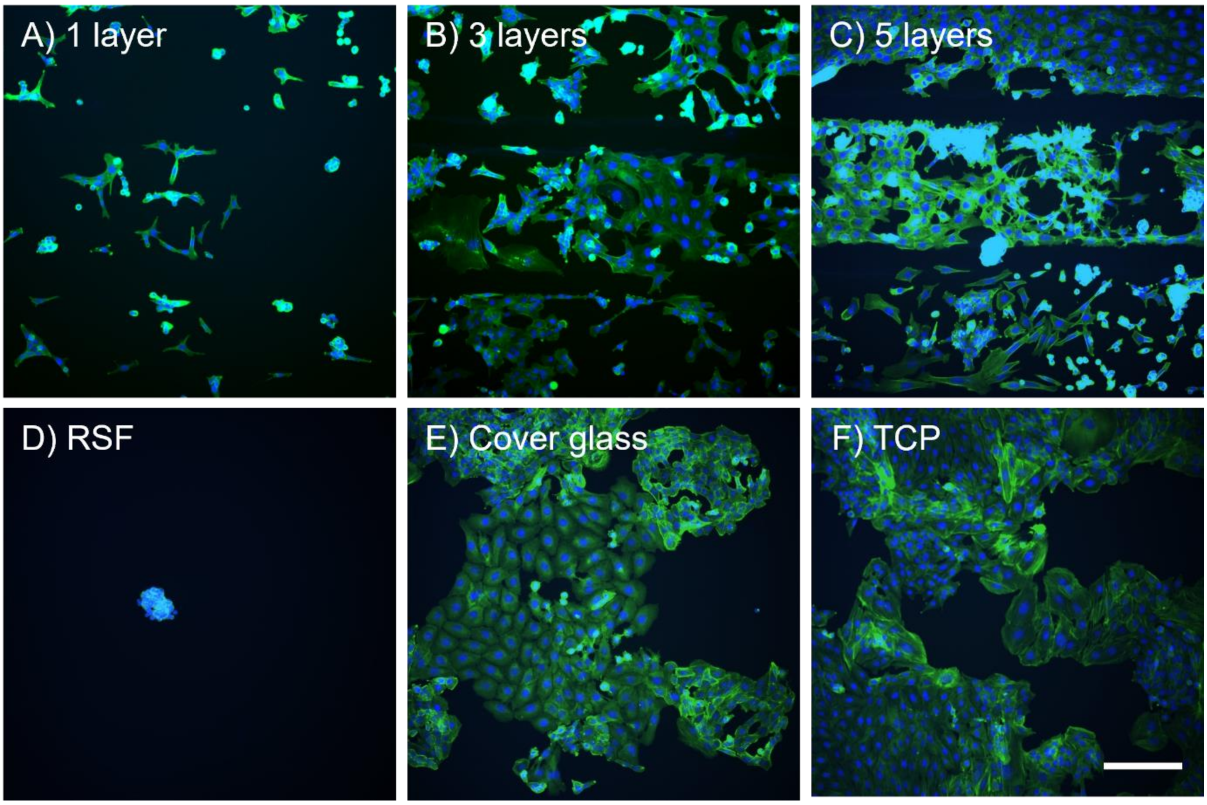

Figure 50. Fluorescence images of PC12-Adh neuronal cells growing on micropatterned I_3K lines. Cell nuclei are labelled with DAPI (blue) while phalloidin-FITC (green) is used to label F-actin filaments in the cytoskeleton. The lines with different number of layers of I_3K are printed by DoD inkjet printing with a 40 µm nozzle on top of the RSF coated cover glasses. A) 1 layer, B) 3 layers, C) 5 layers, D) RSF surface, E) cover glass surface, F) TCP (tissue control plastic). Scale bar = 200 µm.

However, the overall width of the samples, shown in Figure 49, indicated that these patterns were between 270 - 290 µm in width while PC12-Adh cells are 20 - 30 µm in size. This difference in size suggests that the cells would miss the linear topographical cues provided by the micropatterns. Hence, they attached and proliferated inside the pattern, but they did not align with it. Therefore, a further optimisation of the pattern is needed, this will be carried out by reducing the concentration of the ink and modifying the waveform of the piezoelectric.

5.4.3. Contact angle of I_3K bioink on RSF surfaces

Static contact angle provides information on the wettability properties of a solid surface, i.e., how a liquid spreads over a solid surface. This angle is measured at the interphase between the three phases: liquid, solid and gas (usually air) (Figure 51) and depends on thermodynamic properties such as surface energy [232, 233]. Moreover, when the used liquid is water, this can be related to the hydrophilicity/hydrophobicity [188] of the solid surfaces.

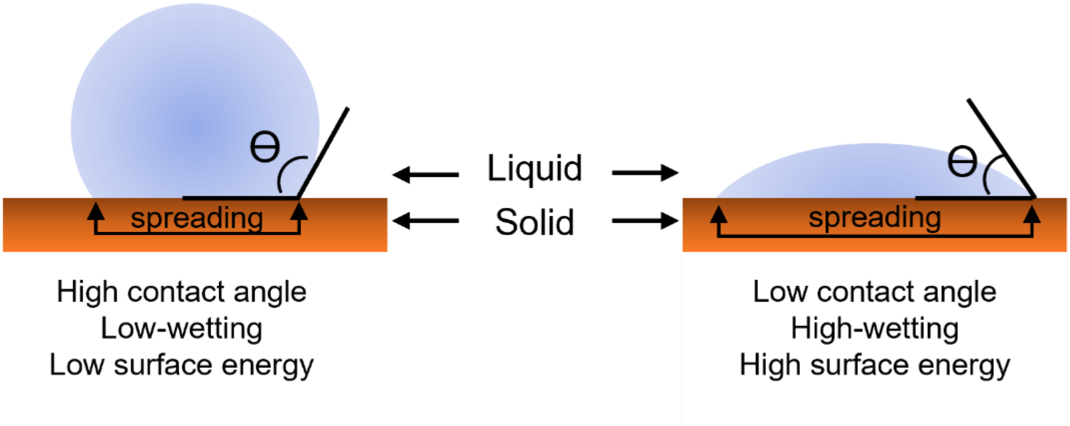

Figure 51. Schematic representation of different contact angle, Θ (°) and its relation to wettability and surface energy. Adapted from the works of Zhang, B. and W. Xu [188], Janssen, D., et al. [232] and Huhtamäki, T., et al. [233].

Since different liquid droplets would interact differently with the same solid surface, this can provide an insight of how a specific liquid will spread over a solid surface. For this reason, the contact angle using our bioink (0.5 mg/ml of I_3K dissolved in 20 mM HEPES buffer at pH 6) and deionised water (DI-water) on RSF coated cover glasses are compared (Figure 52). While the contact angle for deionised water was on an average 59°, when using the I_3K bioink a higher average angle of 96°, therefore the surface energy is lower and the bioink spread less on RSF surfaces than when using water. This interaction is critical for the spreading and adhesion of the droplet to the substrate while printing, which is also related to the final definition and quality of the printed structures.

While static water contact angle can give the wettability property of a specific surface which can then be related to its hydrophilicity/hydrophobicity [188], different liquid droplets would interact differently with the same solid surface. This can provide an insight of how a liquid will spread over a solid surface. For this reason, the contact angle using our bioink (0.5 mg/mL of I_3K dissolved in 20 mM HEPES buffer at pH 6) and deionised water (DI-water) on RSF coated cover glasses were compared (Figure 52). While the contact angle for deionised water was on average 59°, when using the I3K bioink a higher average angle of 96° was observed. Therefore, the surface energy was lower and the bioink spread less on RSF surfaces than when using water. This interaction is critical for the spreading and adhesion of the droplet to the substrate while printing.

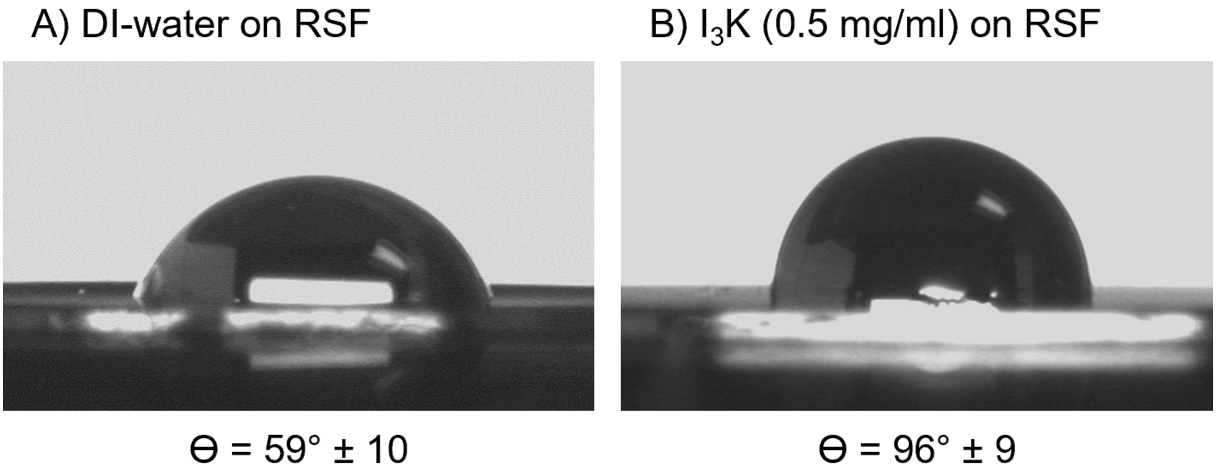

Figure 52. Contact angle of A) deionised water on RSF coated cover glass and B) bioink, 0.5 mg/mL I_3K in 20 mM HEPES buffer (pH 6).

On the other hand, the degree of spreading in inkjet printing, since the droplet volume is in picolitres and have low in-flight velocity, is mostly determined by energy dissipation methods such as impact forces and capillary forces [234-237].

5.4.4. Optimisation of micropatterns done via inkjet-printing

Waveform

As mentioned before, the printhead device used for the present study is equipped with a piezoelectric material that when subjected to a voltage pulse deforms and jets a droplet. This pulse waveform can be classified into single polar pulse (Figure 45A) and bipolar pulse waveform (Figure 45B) [223]. Moreover, it has been investigated before the effect of this waveform on the satellite droplets formation [230, 231].

In this study, only the effect of the voltage applied to the piezoelectric was investigated. Figure 53 shows the different droplets formed with all the different voltage pulses used and their corresponding waveform. For single polar pulse, the lowest voltage that was able to produce a droplet was 35 V; below this, no droplet was formed. For voltages between 35 – 50 V a main droplet was formed followed by a secondary droplet that followed the same path. Above 90 V, bioink was jetted in the form of a tail that followed the main droplet path.

Moreover, for voltages above 80 V, the time in which the strobe photo was taken had to be decreased from 300 µs to 150 - 200 µs since the droplet was formed quicker and it was out of the field of view.

On the other hand, when a bipolar pulse wave was used, the formation of the droplet was quicker than that of the single polar pulse. Moreover, a stable droplet was formed at lower voltages such as ±30 V with just one satellite droplet. Increasing the voltage also increased the number of satellite droplets. These also merged into a tail that followed the path of the main droplet, this was achieved at a lower voltage, 50 – 60 V, when compared to the single polar wave pulse.

Overall, the droplet corresponding to the ±30 V bipolar pulse wave was selected for future printing studies as it was the most stable and reproducible and also generated less satellite droplets, although the ones that were formed followed the path of the main droplet and did not affect the quality or the definition of the printing patterns.

A series of stroboscopic images were acquired at different time points to assess the droplet formation when using a bipolar pulse wave with a voltage of ±30 V (Figure 54 B). The droplet started forming around 60 µs while complete detachment from the nozzle occurred at around 100 µs. After this, a main droplet followed by a second droplet was seen following the same path until they were out of the field of view. Figure 54 shows the time lapse of the drop formation.

Lastly, size and reproducibility of the optimised droplet was assessed. It should also be noted that the I_3K ink is made fresh for every printing batch and after 3 days of self-assembly, therefore, some differences in printability can be expected. Hence, a total of 12 different printing days were considered and three strobe images of the printing droplets were taken to use in this analysis. Figure 55 A shows four representative stroboscopic images of the droplet formed on different days of printing, differences in the droplet velocity can be observed since some droplets had moved farther from the nozzle although all the images were taken around 400 µs after the voltage pulse was applied. On the other hand, Figure 55 B shows a graphical representation of the volume of each jetted droplet, statistical analysis does not show any

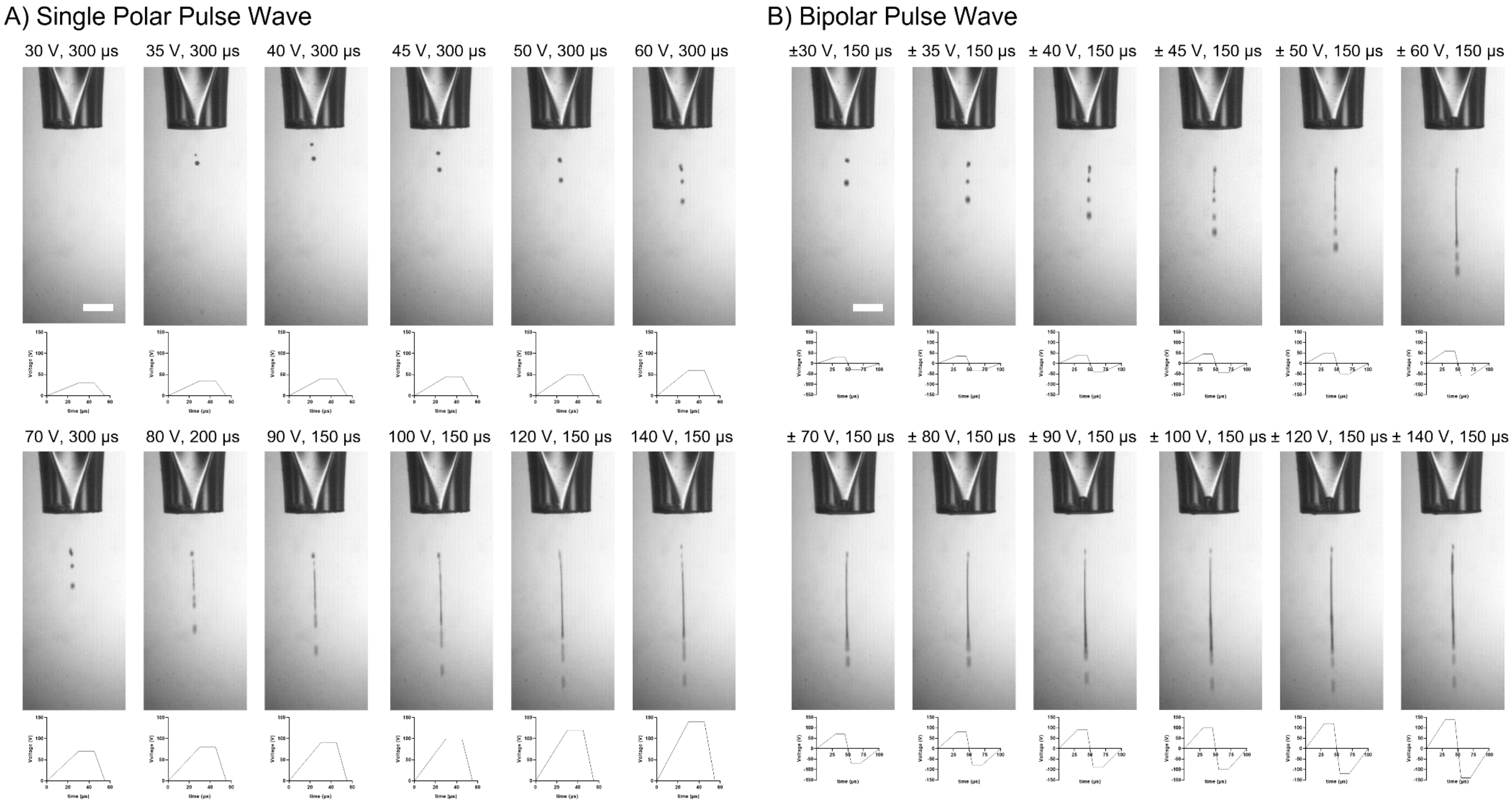

Figure 53. Strobe images of the droplet jetting for A) single polar pulse wave and B) bipolar pulse wave. Each set gives information related to the voltage applied, the time at which the strobe image was taken, the strobe image and the graphical representation of the waveform. Frequency used was 100 Hz. Scale bar represents 300 µm.

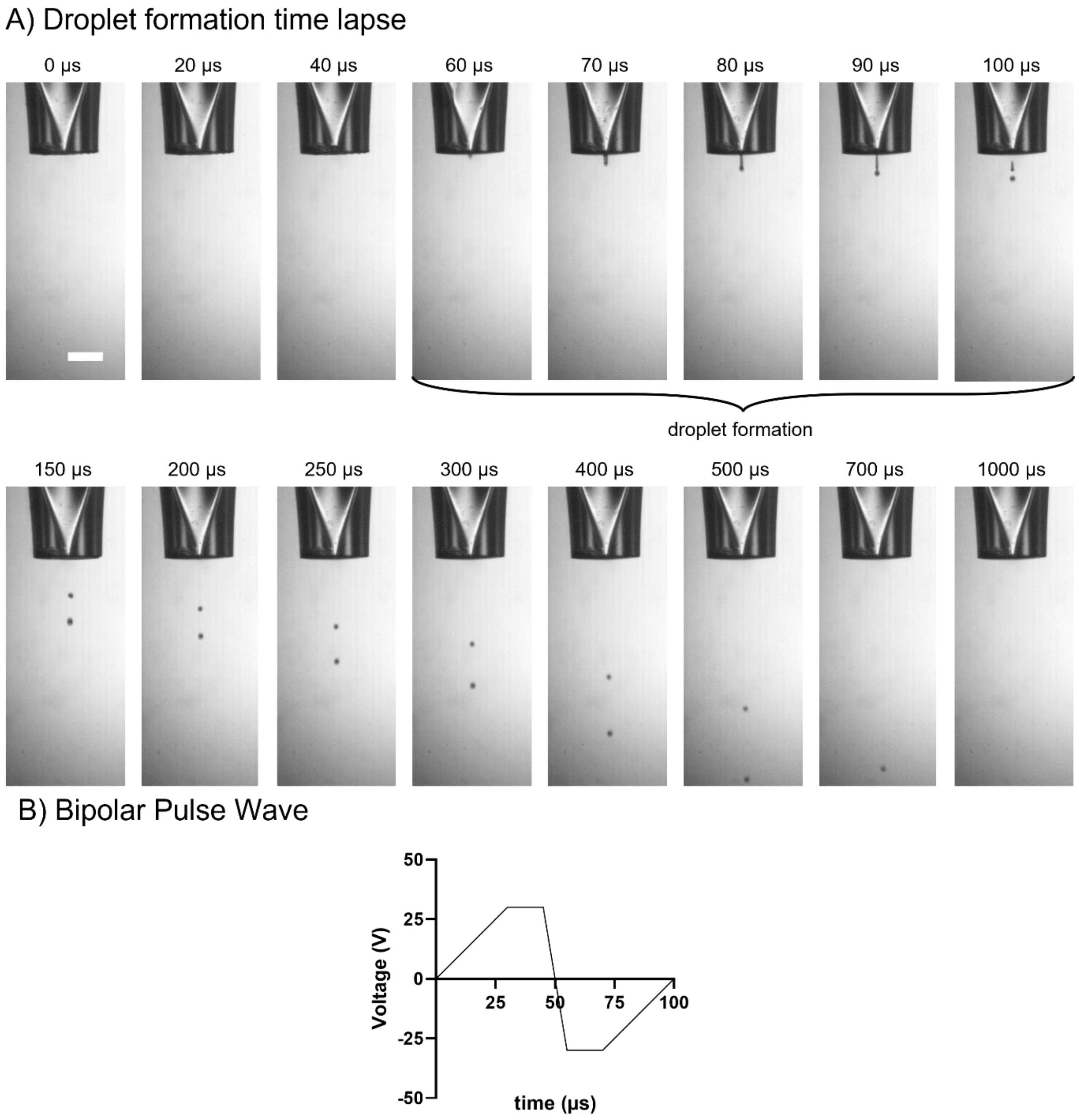

Figure 54. A) Strobe time lapse images of the droplet formation using a bipolar pulse wave with a voltage of ±30 V. Droplet is beginning to form at 60 µs while complete detachment from the nozzle occurs at 100 µs. Two droplets are finally formed and jetted following the same path. Scale bar represents 300 µm. B) Bipolar pulse wave graph with an amplitude of ±30 V.

significant difference between droplet 1 (satellite) at different days of printing, moreover, there is also no statistical difference between droplet 2 (main) on the different printing days. All in all, an average of 72.6 pl ± 7.6 were jetted per trigger, considering both droplets, 28.2 pl ± 5.6 for the satellite droplet and 44.4 pl ± 7.6 for the main droplet.

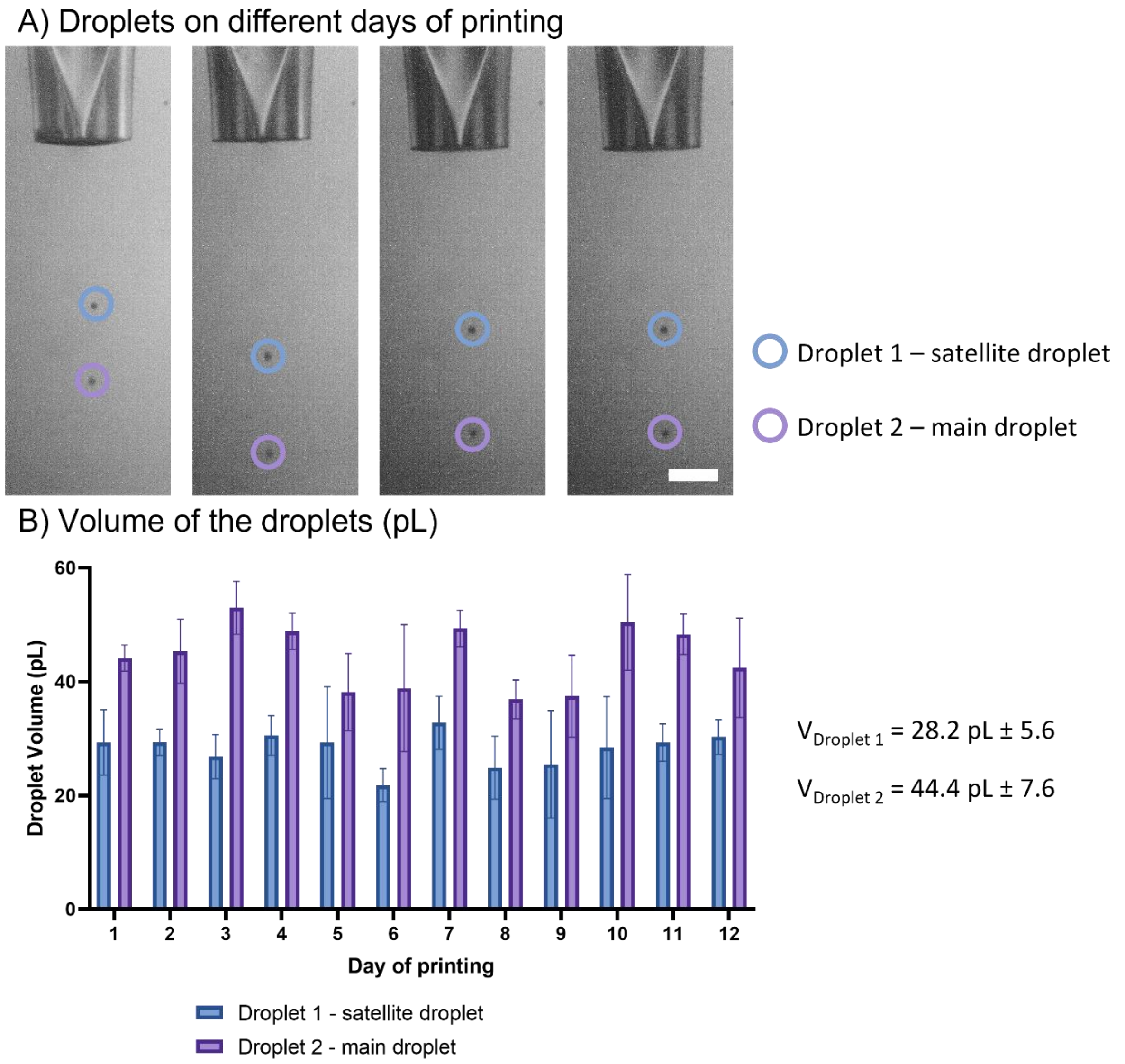

Figure 55. A) Strobe images of different droplets taken at the same time in the jetting process but on different days of printing with freshly made I_3K inks. Scale is 300 µm. B) Graphical representation of the average volume of each droplet (pL), two-way factor analysis of variance (ANOVA) was performed. P values of *P < 0.05, **P < 0.01, ***P < 0.001 and ****P < 0.0001 were considered as significant

Droplet spacing

Droplet spacing (DS) is an important parameter that can define the resolution of the printing. Using a drop-on-demand inkjet printer implies the ink is printed as individual drops rather than as a continuous jet. Therefore, to create continuous micropatterns drops need to overlap, this is achieved by decreasing the DS. However, optimisation of the DS was needed to avoid scalloped profiles that can affect the quality of the printing and to obtain a uniform profile. On the other hand, if the DS is too low, bulging of the pattern can occur leading to areas where the printed area is wider than required. This behaviour has been previously described by Soltman et al. [238]. More recently, the ability to use a varied instead of uniform DS throughout printing has been studied. Mu et al. [239] used non-uniform DS to develop a technique where a higher density of droplets at the end of a printed line can compensate for the inherent flows, i.e., Marangoni and capillary flows, that can make the printed surface convex instead of flat. This can also eliminate the need to use multiple solvents in the ink which can, in turn, reduce the overall cost of the printing.

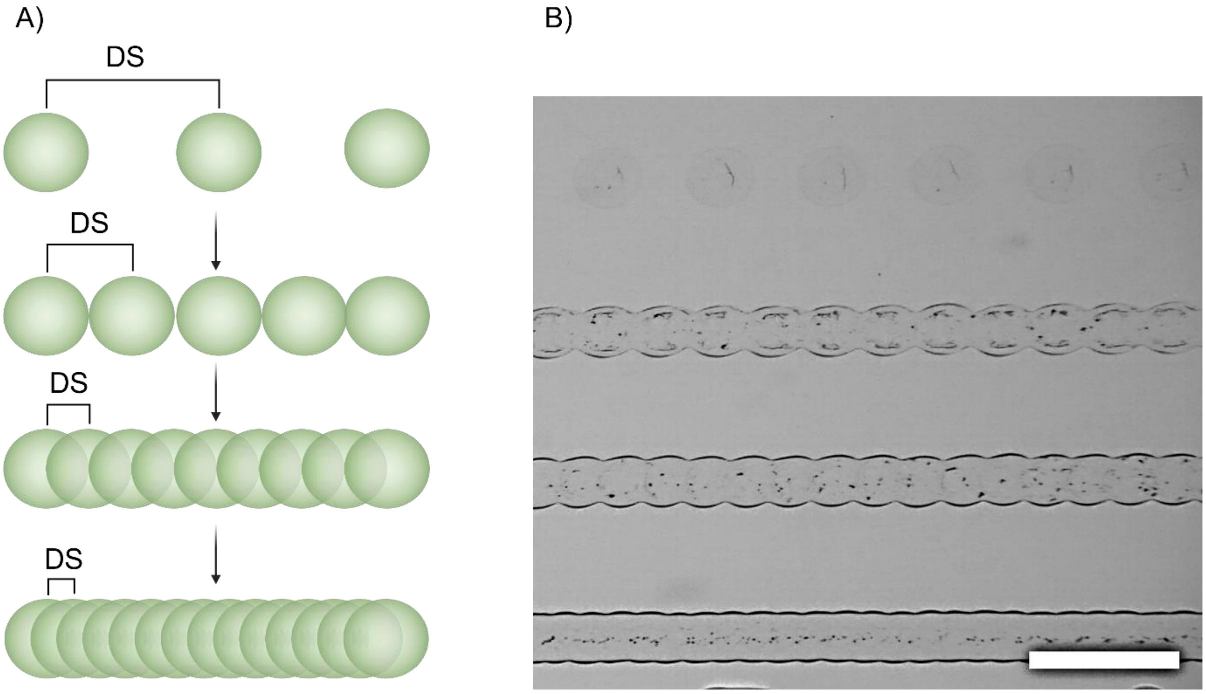

Figure 56. A) schematic representation of how decreasing the droplet spacing (DS) can generate continuous patterns, B) Brightfield images of the DS change effect on the printed patterns, DS decreases from top to bottom. Scale bas is 200 µm.

Optimised micropatterns

Finally, the micropatterns were printed using the optimised bipolar wave pulse and droplet spacing. However, the patterns showed irregularities at the end of each printed line. Because the interaction between the I_3K ink droplet and the RSF surface had a low surface energy and therefore a high contact angle, ϴ = 96° ± 9, the ink was absorbed towards the beginning of each line. The Marangoni and capillary flows on the evaporation of sessile droplets dramatically affect the drying process of the droplet and, thus, the final printing quality. This has been thoroughly studied before [240-243]. Figure 57 A shows the printing of one single layer with an alternate direction of printing, here it can be seen that the end of each line appears to be disappearing (orange arrows). Once an individual line finished printing, it had not dried completely, by printing it again but in the opposite direction, a full line was achieved. Figure 57 B shows that all printed lines with a double layer have a beginning and an end. This way of printing a double layer is different from printing more than one layer, with the double layer approach the second pass is done while the line of the pattern has not fully dried and so they merge together in one line. On the other hand, the printing of the layers is done once the previous layer has already dried and, therefore, more material builds up overtime.

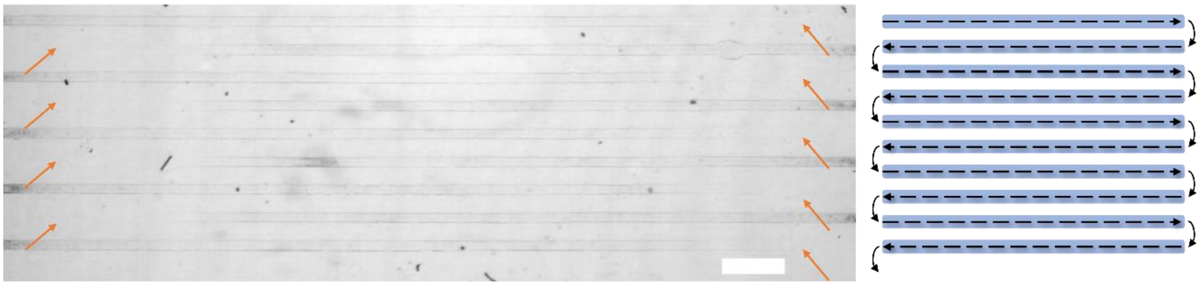
A) 1 single layer

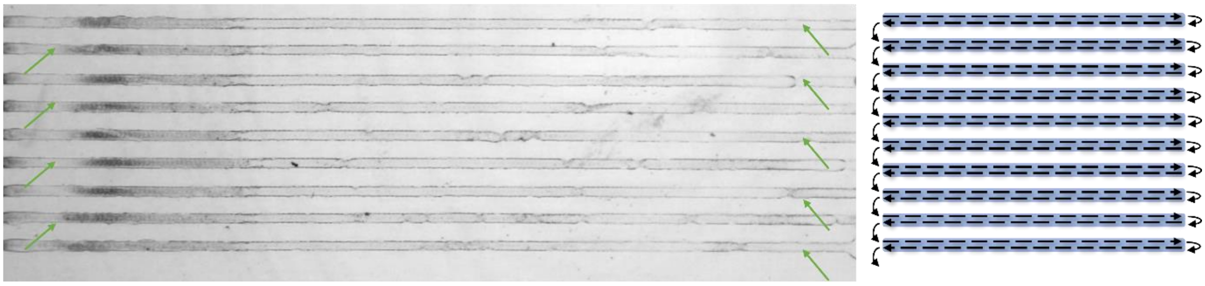
B) 1 double layer

Figure 57. A) Brightfield image of a printed single layer sample, orange arrows indicate missing ends of the lines, B) brightfield image of a printed double layer sample, green arrows indicate successful printing of the ends of the lines. On the right side the printing direction for each sample is represented by arrows. Scale bar is 500 µm.

Using this double layer approach, samples with different numbers of layers were printed. The focus of all the optimisation process was to reduce the width of each line of the pattern so that this can be recognised by the cells. Statistical analysis shows a significant decrease in the line width when comparing the same number of printed layers, before and after optimisation. The width for 1 layer decreased from 271 µm ±14 to 69 µm ±3, for 3 layer the change was from 288 µm ±11 to 83 µm ±7 and, lastly, for 5 layers the width was reduced from 294 µm ±6 to 92 µm ±16, this can be seen in Figure 58. In total, twenty parallel lines were printed per sample with an average length of 7.5 – 7.6 mm as seen in Figure 59.

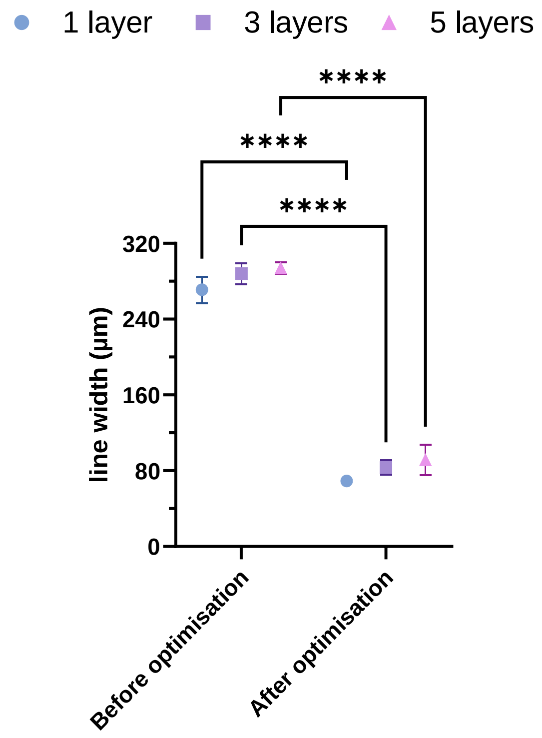

Figure 58. Graphical representation of the average width of the micropattern lines when they are printed with different numbers of layers. Two-way factor analysis of variance (ANOVA) was performed. P values of *P < 0.05, **P < 0.01, ***P < 0.001 and ****P < 0.0001 were considered as significant.

5.4.5. *In vitro* studies with PC12-Adh neuronal-like cell line on optimised micropatterns

Cell attachment of PC12-Adh cells was assessed qualitatively on the I_3K micropatterns on RSF coated cover glasses. Samples with different numbers of layers, i.e., 1, 3 and 5 layers, were used as scaffolds to grow PC12-Adh cells. Figure 60 shows fluorescence images of cells after growing for 7 days with general culture media. While 1 layer of I_3K exhibited low cell attachment, cells in samples with 3 and 5 layers grew along the lines and proliferated. This is consistent with previous work carried out and published by our research group [196, 197], where cell attachment was also promoted by the inkjet-printed micropatterns of self-assembled peptides. However, in their study, cell alignment was not achieved since the width of those patterns was above the size recognised by the cells. In contrast, in the present study, alignment of PC12-Adh cells was achieved.

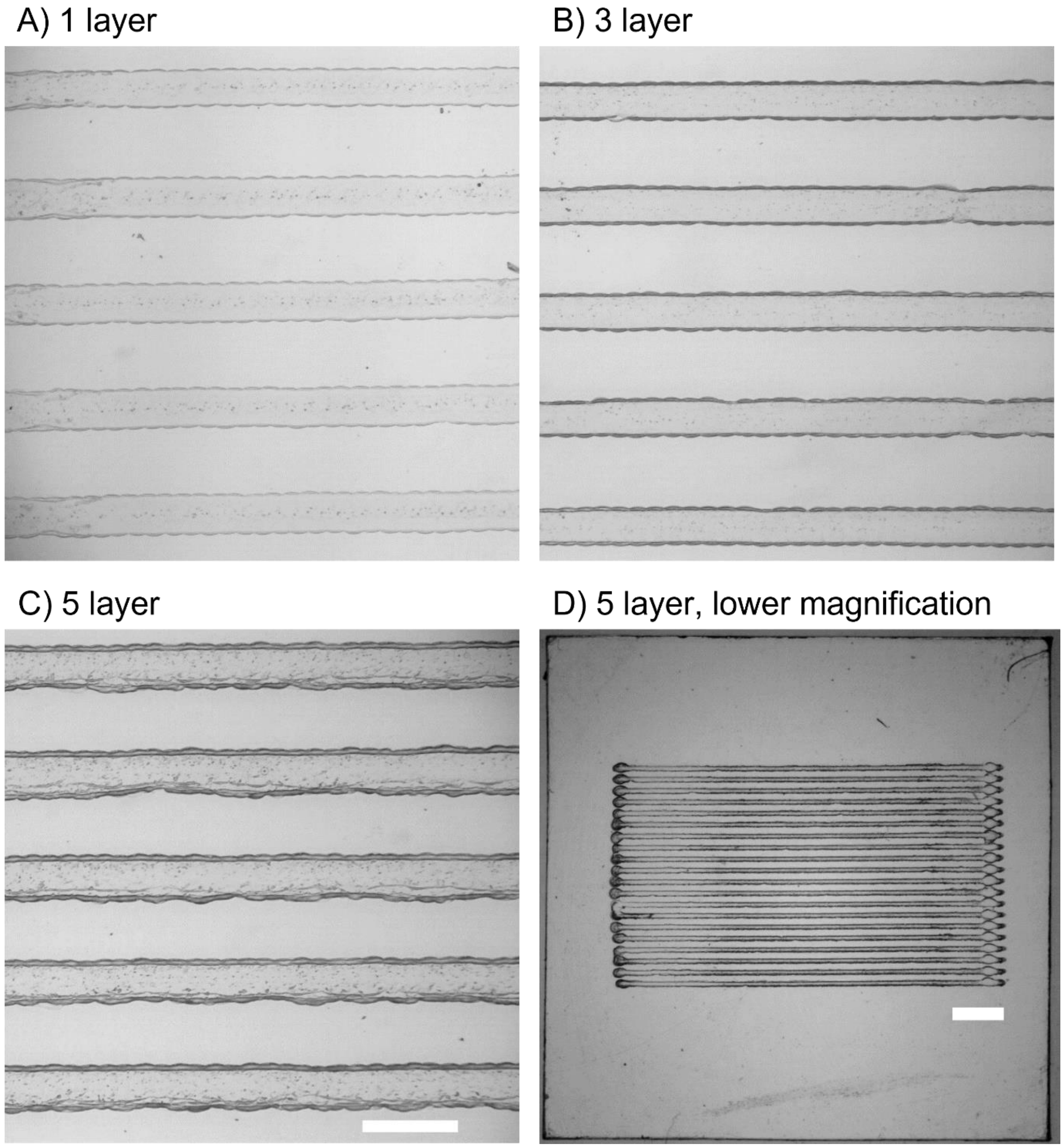

Figure 59. Brightfield images of I_3K micropatterns printed via drop-on-demand inkjet printed on RSF coated cover glasses with optimised droplet formation. Different numbers of layers are printed: A) 1 layer, B) 3 layers and C) 5 layers. Scale bar represents 200 µm. D) Overall brightfield images of 5 layers I_3K micropattern RSF coated cover glasses, scale bar represents 1 mm.

A) 1 layer

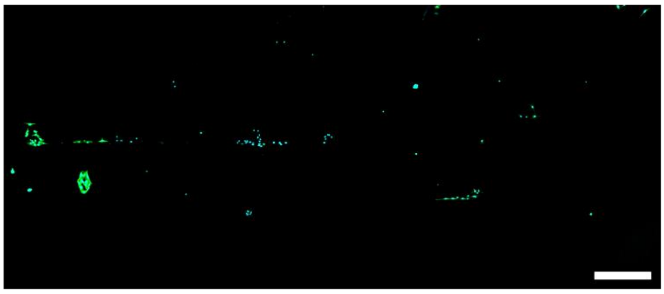

B) 3 layer

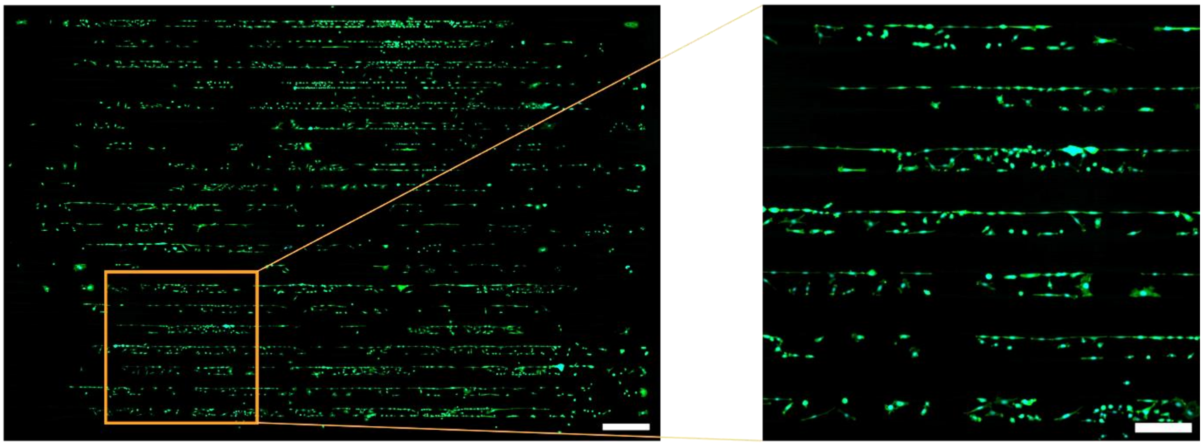

C) 5 layer

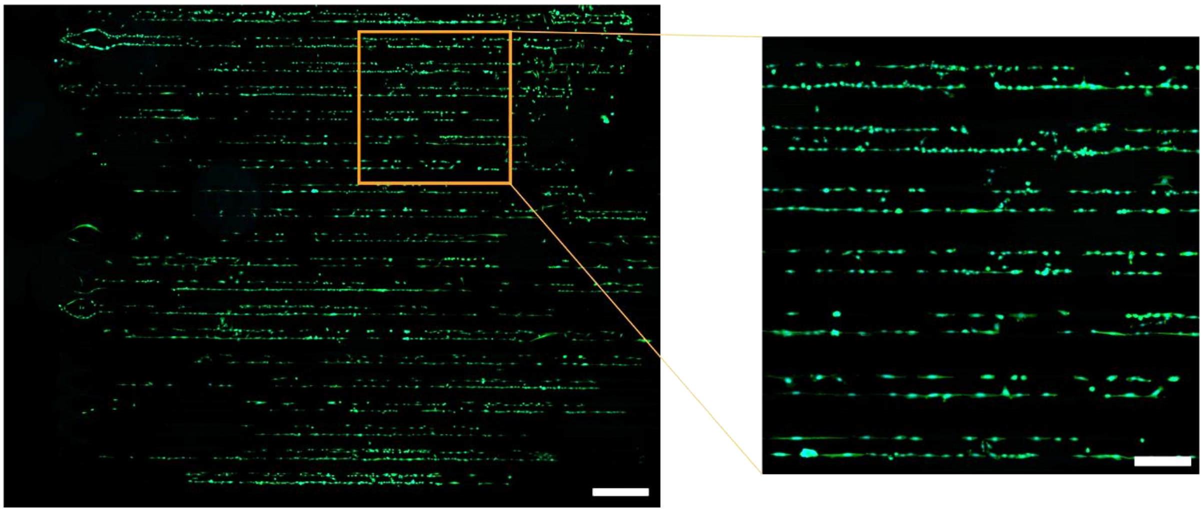

Figure 60. Fluorescence images of PC12-Adh neuronal cells growing on I_3K micropatterned lines. Cell nuclei are labelled with DAPI (blue) while phalloidin-FITC (green) is used to label F-actin filaments in the cytoskeleton. The lines with different number of layers of I_3K were printed by DoD inkjet printing with a 40 µm nozzle on top of the RSF coated cover glasses. A) 1 layer, B) 3 layers and C) 5 layers. Scale bar represents 500 µm on left side and 200 µm on the right side.

Moreover, 20 lines were printed in each sample as shown in Figure 59 D, however, images of the cells show more lines than those printed. The reason for this can be seen in Figure 61 A. Each printed line corresponded to two of the lines of grown cells. This is perhaps because the peptide accumulated on the edges of the printed lines instead of covering each line in a uniform manner. This is known as the "coffee ring effect" because of the ring structure left after drying is similar to that seen when a drop of coffee dries. This has been studied before by several authors [238, 240, 243-245]. Lim et al. [240] studied the effect of the evaporation, capillary, and Marangoni flows, on the final morphology and microstructure of inkjet printed films in organic semiconductors. They concluded that a nucleation event occurred at the edge of the drying droplet leaving a ringlike structure on these films. The addition of another solvent with low surface tension and high boiling point solved this issue [240].

Although, this coffee ring effect is undesirable in most cases as it affects the quality of the printing since it prevents the formation of homogenous layers; in this study, the possible nucleation of the self-assembled I_3K nanotubes at the edges of the patterned line produced two narrow bio-active edges in each line that were recognised by the cells as the attachment site. A possible mechanism explaining this effect is shown in Figure 61 B.

5.4.6. *In vitro* differentiation studies with PC12-Adh neuronal-like cell line on optimised micropatterns

PC12-Adh cell line is a useful nerve model commonly used in neuroscience research. This cell line can be differentiated into morphological and functional nerve cells with an external stimulus such as the presence of nerve growth factor (NGF) or brain-derived neurotrophic factor (BDNF) [105, 107, 141, 246]. When these cells are differentiated, they undergo neurite development, i.e., a group of developed axons and dendrites, (Figure 62) and express markers such as synapsin I and Beta-III tubulin (βIII-tubulin) [105, 247]. Moreover, differentiated PC12-Adh show a behaviour change in growth, from growing as polygonal cells in tight clusters to individual cells that show neurite connections with each other as seen in Figure 62 B. Moreover, cells in Figure 62 B have differentiated by growing on RSF:I_3K (40 mg/mL : 5 mg/mL) coated cover glasses without the need of NGF or BDNF.

Moreover, in Figure 62 B cells were differentiated without the presence of an external stimuli such as NGF, cells were grown directly on RSF:I_3K (40 mg/mL : 5 mg/mL) coated cover

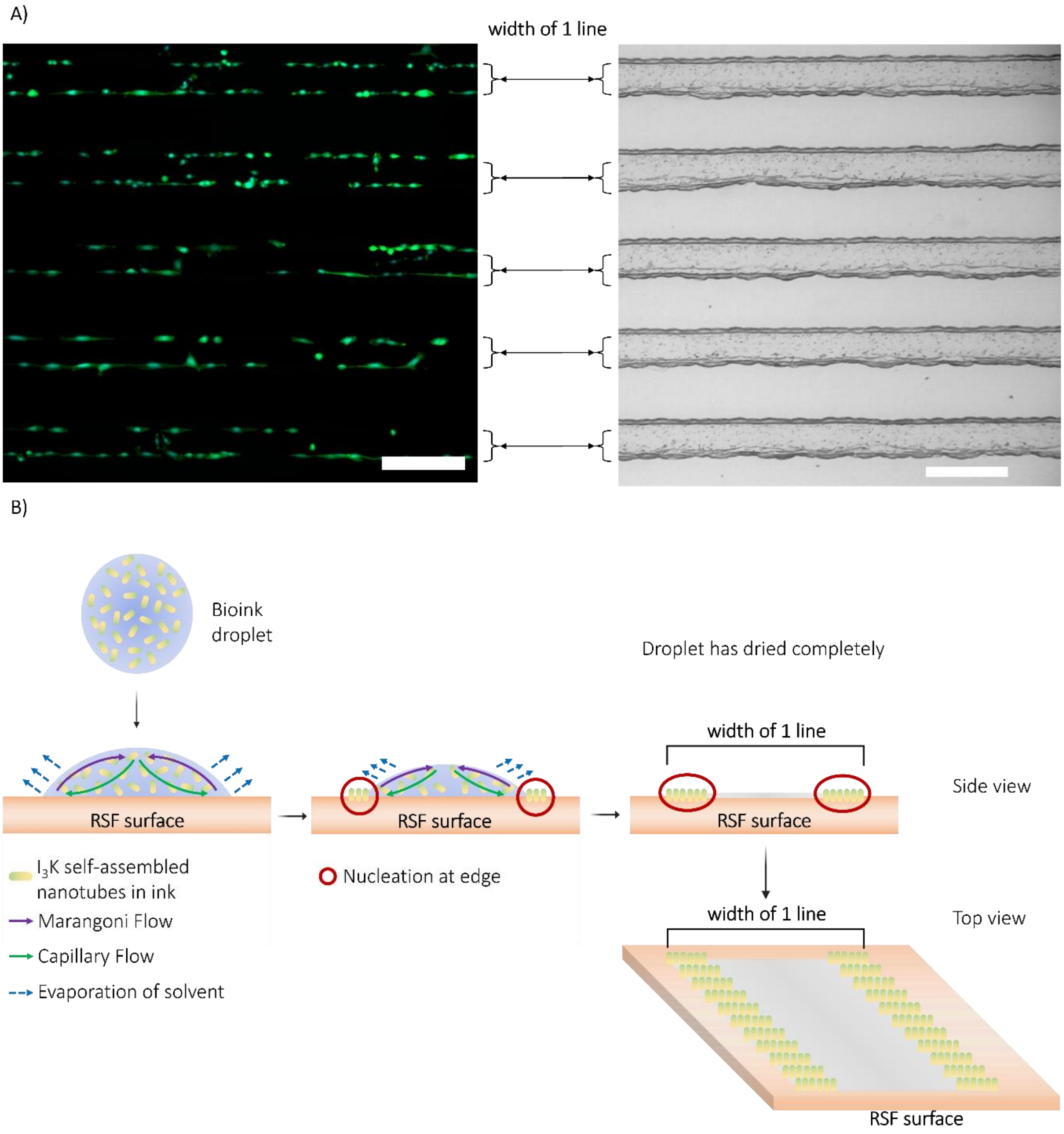

Figure 61. A) Comparison of fluorescence and brightfield images of I$_3$K micropatterns with and without PC12-Adh cells, respectively, displaying the width of 1 line. Cell nuclei are labelled with DAPI (blue) while phalloidin-FITC (green) is used to label F-actin filaments in the cytoskeleton. B) Proposed drying mechanism showing how the Marangoni, capillary and evaporation flows affect the nucleation of the I$_3$K peptide in the drying process. Adapted from the works of Lim, J.A., et al. [240] and Uddin, M.J., J. Hassan, and D. Douroumis [241]

glasses. This indicates that I$_3$K not only promotes cell adhesion and proliferation, but it can be an ideal candidate for differentiation.

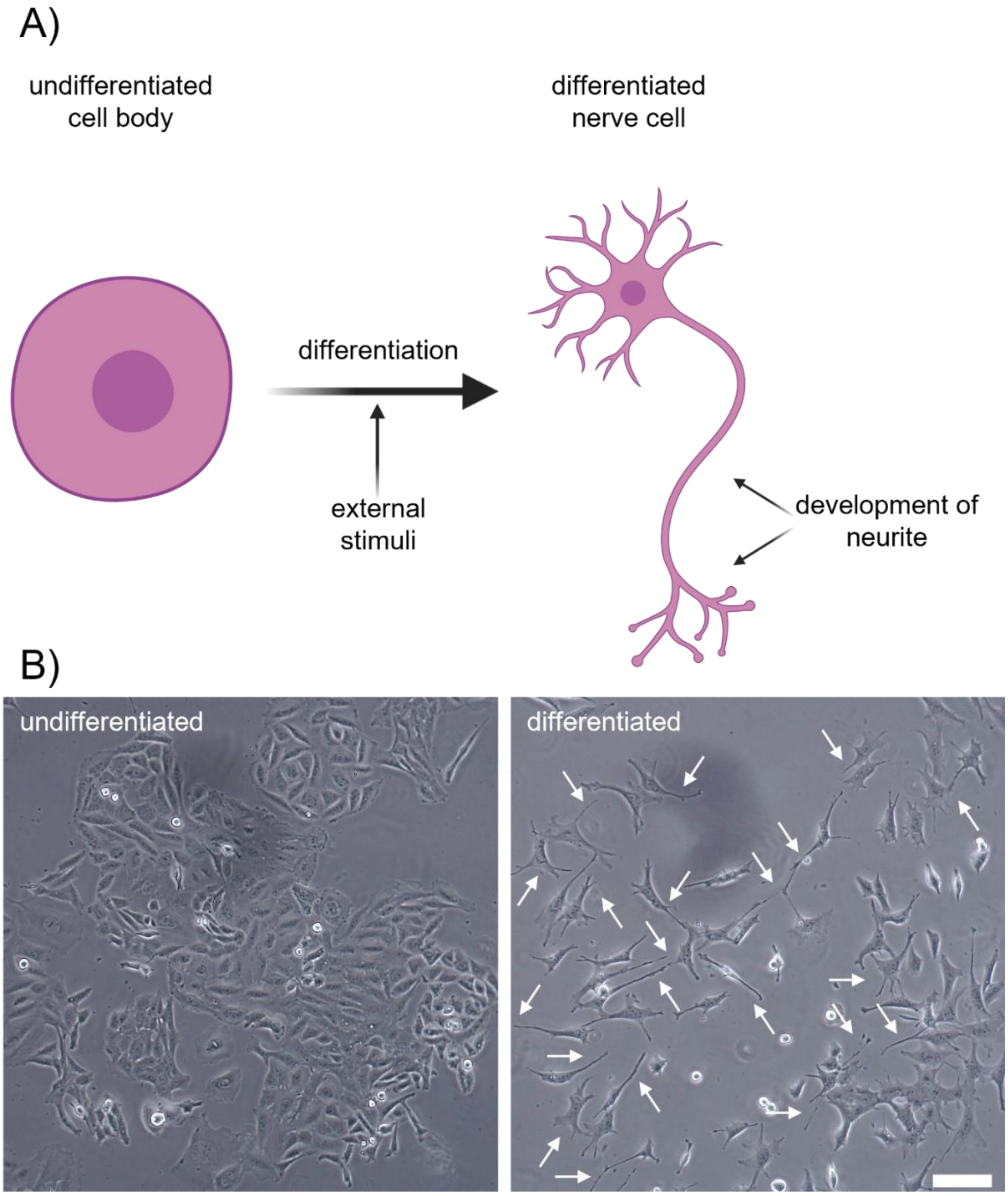

Figure 62. A) Schematic representation of the differentiation of a nerve cell under an external stimulus, B) Brightfield images of undifferentiated (left) PC12-Adh cells growing on tissue culture plastic (TCP) and differentiated (right) PC12-Adh growing on RSF:I_3K (40 mg/mL : 5 mg/mL) coated cover glasses. Arrows indicate the presence of developed neurites induced by differentiation. Scale bar represents 100 µm.

In vitro differentiation studies

For differentiation studies only printed samples with 3 layers of I_3K were used. Also, the number of cells seeded on the samples was reduced to allow more space between cells so neurites can develop. Nerve growth factor (NGF) was added to the media at a concentration of 50 ng/mL to half of the samples to promote differentiation. Figure 64 shows the result of these differentiation studies. Both samples with and without NGF showed signals of differentiation. Considering that NGF is necessary to induce differentiation in PC12-Adh cells, this suggests a role for I_3K in inducing nerve differentiation in vitro. The average length of neurite in samples with NGF was 69.5 µm ± 24, this increased to 79.4 µm ± 47 in samples without NGF. This is larger than previously reported by Sun et al. [197], where the average length of neurites in PC12-Adh grown on RSF:I_3K (40 mg/mL : 3 mg/mL and 40 mg/mL : 4 mg/mL)coated glass was between 20-25 µm [197]. The longest neurite found without the use of NGF was 226.5 µm in comparison with 112.6 µm on samples with NGF. On the other hand, the most common type of nerve cell developed was bipolar (two neurites growing in opposite directions from the cell body) (Figure 64 white arrows). In addition, some multipolar neurons, where cells produced more than two neurites (Figure 64 blue arrows) were also developed. Multipolar nerves were more common in samples with NGF.

However, the relation between the presence of I_3K, linear topographical cues given by the patterns and the differentiation in the absence of NGF was not clear and more studies are needed to determine which factor was more important in the differentiation of nerve cells.

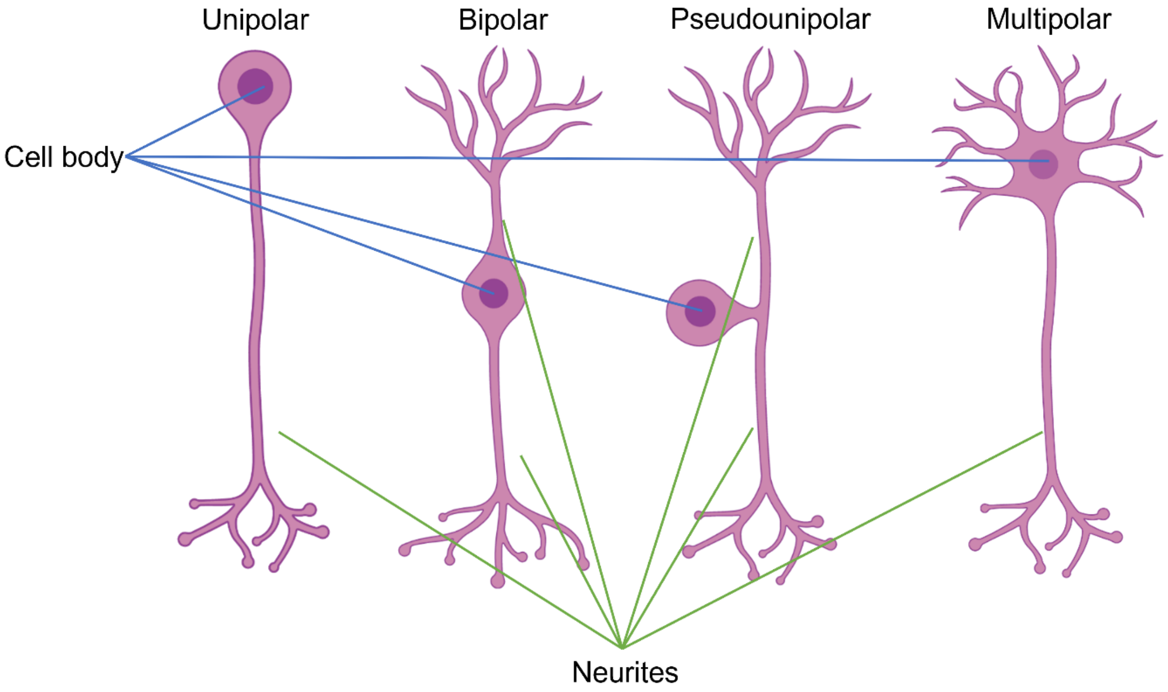

Figure 63. Schematic representation of different types of neurons based on the number and location of the neurite growth. Created with BioRender [93].

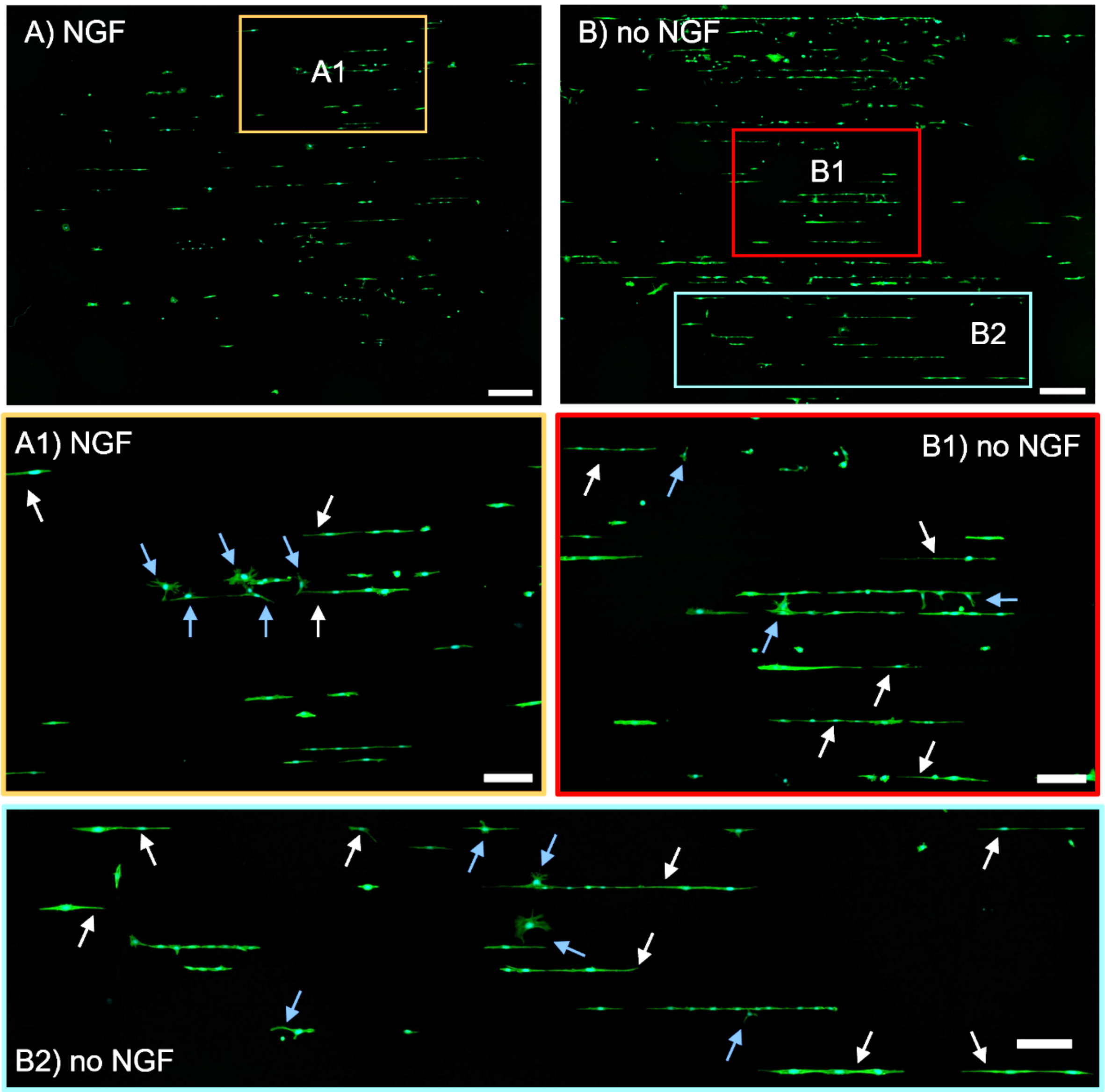

Figure 64. Fluorescence images of PC12-Adh neuronal cells growing on I_3K micropatterned lines. Cell nuclei are labelled with DAPI (blue) while phalloidin-FITC (green) is used to label F-actin filaments in the cytoskeleton. The lines with 3 layers of I_3K are printed by DoD inkjet printing with a 40 µm nozzle on top of a RSF coated cover glass. A) nerve growth factor (NGF) was added to the media to promote differentiation, B) no NGF was added. Arrows indicate the presence of developed neurites induced by differentiation, blue indicate multipolar and white bipolar. Scale represents 500 µm for A and B, and 200 µm for A1, B1 and B2.

5.5. Conclusion

In this chapter, the novel amphiphilic peptide I_3K was successfully printed using the drop-on-demand (DoD) inkjet printing. Spatially oriented microfeatures of biological relevance were selected to be printed, in this case parallel lines similar to the longitudinal parallel axons in nerves [214]. Inkjet printer is a reliable technique to print high quality samples with great definition using small amounts of ink. Preliminary patterns showed that the bioink containing

I_3K in HEPES buffer (20 mM, pH 6) after 3 days of self-assembly could be printed achieving high definition. The patterns were printed using a layer-by-layer approach which determined the final I_3K concentration on each pattern; more layers meant more peptide was jetted on the RSF surface. However, these samples with 1, 3 and 5 layers proved to be too wide (271 µm ±14 for 1 layer, 288 µm ±11 for 3 layers and 294 µm ±6 for 5 layers) to be recognised by the cells as the topographical cues for cell attachment and alignment. Optimisation of the droplet was carried out to decrease the width of the patterns. Since the jetting mechanism of the inkjet printer is governed by the piezoelectric material present in the printhead, by modifying the voltage pulse applied, the droplet can be, in turn, modified. This allowed the width of each line of the pattern to be decreased to 69 µm ±3, 83 µm ±7 and 92 µm ±16 for 1, 3 and 5 printed layers, respectively.

PC12-Adh cells were cultured on the optimised patterns. This showed that 1 layer did not produce enough bioactive groups on the surface to promote cell adhesion. In contrast, 3 and 5 layers showed good cell attachment and proliferation after 7 days in culture. Moreover, cells seemed to attach to the edges, a mechanism based on the nucleation of the I_3K nanotubes at the edges of each line of the pattern was proposed. This was founded on the effects of Marangoni, capillary and evaporation flows during the drying process, also known as “coffee ring effect”.

Finally, differentiation studies were carried out with and without NGF, a neurotrophic factor commonly used to promote differentiation in PC12-Adh nerve cells. It was observed that differentiation occurred both with and without NGF, suggesting I_3K can play a role in the *in vitro* differentiation of nerve cells. The average length of neurites in samples with NGF was found to be 69.5 µm ± 24, while in samples without NGF the neurite length increased to 79.4 µm ± 47. The most common type of nerve cell developed was bipolar but multipolar cells were also found, although they were more common in samples with NGF.

However, further studies are needed to find the relation between the differentiation of these cells in the absence of NGF and the presence of I_3K, topographical cues given by the patterns or both.

Chapter 6. Conclusion and Future work

Although SF is a natural protein that has been used successfully in tissue engineering due to its good biocompatibility and biodegradability properties, poor cell attachment to the regenerated materials, RSF, has been reported [2]. RSF is obtained from raw silk by removing a glue-like protein called sericin in a process called degumming. This harsh processing, boiling cocoons in an alkali solution, can affect the final properties of the SF materials. In this study, the relation between the degumming processing and the cell attachment on RSF was assessed. Results obtained from 3 different degumming times, i.e., 30, 60 and 90 min, suggested that although removal of SS was successful, longer periods of degumming caused damaged to the SF fibres as seen in SEM images. Moreover, only RSF solutions from 30 min of degumming had cell attachment showing good biocompatibility. On the other hand, RSF obtained after degumming for 90 min showed low cell attachment while having good indirect biocompatibility. This suggested that this type of silk could be useful to control the cell attachment and guide it.

Furthermore, the use of a novel amphiphilic peptide, I_3K, that could self-assemble into long nanotubes to promote cell addition was proposed. Self-assembly in aqueous solution provided with a nanotube with all the lysine groups facing outwards, these bioactive side chains have been commonly used to promote cell adhesion through coatings with polylysine proteins. AFM scans proved that, at biological pH, electrostatic forces between negatively charged RSF surfaces and positively charged I_3K nanotubes were strong enough to maintain the RSF:I_3K coating in cell culture conditions. In addition, the effect of self-assembly time (0, 1, 3, 5 and 7 days at ambient conditions) on cell attachment was also assessed. All of the different I_3K coated RSF surfaces showed an increase in cell attachment compared to uncoated RSF surfaces. However, I_3K self-assembled for 3 days showed higher cell attachment than the positive control. This I_3K coated RSF surfaces also proved to be cytocompatible. Consequently, it was proven that I_3K is an ideal candidate to improve cell adhesion on scaffolds for tissue engineering applications

The ability to control and guide cell attachment can produce spatial and topographic cues that can affect cell behaviour such as attachment, migration, or even differentiation. To produce spatially controlled regions, non-cell-adhesive background, RSF surfaces, and a cell-promoting material, self-assembled I_3K, are needed. Drop-on-demand inkjet printing is a technique that allows high precision deposition of small amounts of ink, usually in the picolitre range, reducing costs when bioinks are generally expensive. Here, it was proposed to use a bioink made from self-assembled I3K peptide to create bioactive patterns on non-fouling RSF surfaces that can be used to promote cell adhesion and proliferation. Preliminary micropatterns showed good cell attachment and proliferation results, however, the specific cues for these spatially oriented micropatterns were too big (27 µm to 290 µm) to be recognised by the cells (20 - 30 µm). An optimisation of the droplet generated by applying different voltage pulse to piezoelectric actuator of the printhead was carried out. Consequently, a reduction of the width of the patterns to 69 µm - 90 µm was achieved. Cell culture in these narrow patterns showed attachment and proliferation along the edges of each line of the pattern. A possible accumulation of the I_3K peptide on the edges due to Marangoni, capillary and evaporation flows was proposed. Moreover, this type of attachment showed excellent cell alignment that promoted differentiation of the PC12-Adh cells even in the absence of the neurotrophic factor, NGF; suggesting a role for I_3K in inducing nerve differentiation in vitro.

6.1 Future work

In order to continue the line of research and obtain optimised results, further studies are needed, for instance, to clarify whether the differentiation is due to the presence of the I_3K, the topographical cues of the micropatterns or both. Moreover, other amphiphilic peptides can be used such as I_3KVAV, I_3RGDS or I_3QGK as bioinks, individually or as a combination of multi peptide solutions. The use of other critically relevant cells such as Schwann cells needs to be evaluated in the future since these are essential for the myelination of the axons which is a critical step in regeneration of peripheral nerves. Finally, the use of these peptides and silk fibroin as bioactive surfaces for other types of cells (osteoblasts, fibroblasts, and others) can be explored in the future.

The ability to use other amphiphilic peptides as bioinks, to create more complex geometries (Figure 63) and to culture many numbers of different cells showcases the adaptability and applicability of this technique in the fields of tissue engineering and regenerative medicine.

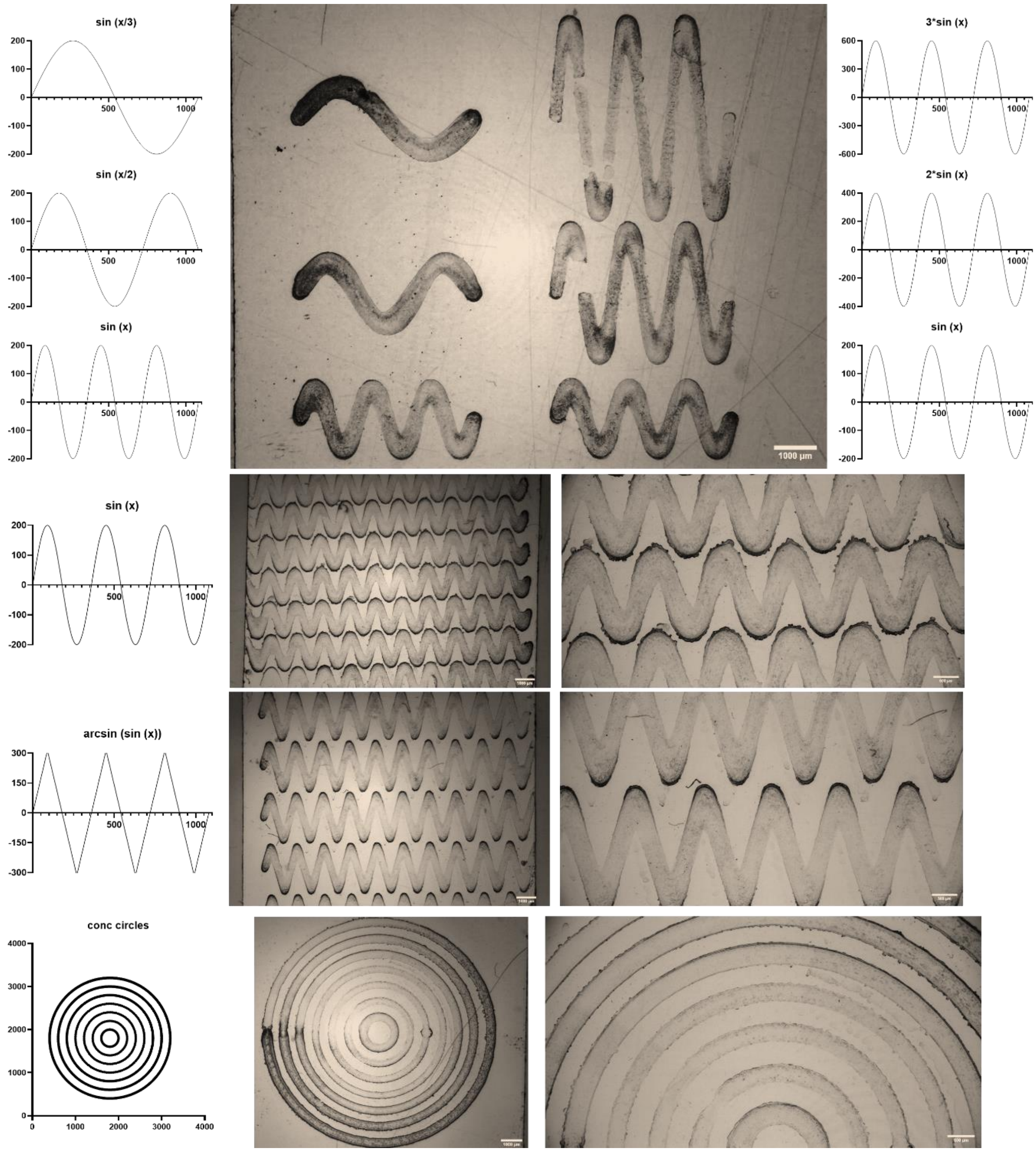

Figure 65. Brightfield images of complex patterns made by drop-on-demand inkjet printing with I_3K bioink on RSF surfaces (1 mg/mL and 40 mg/mL respectively) .

One potential application of printed micropatterns is in organ-on-a-chip (OOC) systems. These chips are typically made of clear, flexible polymers with tiny channels that allow the flow of nutrients, cells, and fluids, replicating the environment of real organs. They combine tissue engineering, microfluidics, and biomaterials to create realistic models of organs and control cell microenvironments. Such systems are particularly significant in the development of neuronal models, as they enable high-throughput research that is often limited by the lack of reliable in vitro models.

Printing technologies play a significant role in the design and fabrication of nerve guidance conduits (NGCs) that can be integrated into OOC systems. For instance, Fang et al. [248] highlighted the need for NGCs that possess suitable mechanical properties and topology to direct axon growth and facilitate neovascularization. The biocompatibility and performance of OOC systems are enhanced by combining microfabrication with advanced bioprinting methods. For example, Petcu et al. [249] investigated how 3D-printed scaffolds can improve the healing microenvironment for peripheral nerves These engineered surfaces can influence cellular behaviour, such as the migration and differentiation of Schwann cells and stem cells, which are essential for successful nerve repair.

In summary, organ-on-a-chip technologies combined with cutting-edge printing methodologies and materials science facilitate the development of sophisticated models for studying peripheral nerve regeneration, paving the way for significant advancements in nerve repair therapies.

Appendix A. Validation of βIII-tubulin immunostaining

βIII-tubulin is a protein found in microtubules in the cytoskeleton of neuronal cells that can be used as an early marker of nerve differentiation [250]. This marker has been successfully used to identify nerve cells from other cells such as glial or Schwann cells in tissues of animal origin [106, 107, 197, 250, 251].

The biochemical process to identify these markers or antigens can be done by direct or indirect immunolabeling. In the direct approach the primary antibody is covalently conjugated to the antigen and to a fluorophore. On the other hand, when the primary antibody is covalently linked to the antigen of interest and to a second fluorophore-conjugated antibody is known as indirect immunolabeling.

To localise the expression of βIII-tubulin, an indirect approach was used. The primary antibody mouse anti-βIII-tubulin was used to bind to the βIII-tubulin antigen, while a secondary antibody, horse anti-mouse IgG (conjugated with the fluorophore Texas RED) was used for detection of the primary antibody. One important step of the immunolabeling process is the blocking of non-specific binding of the antibodies to cells or tissue due to charge interactions or Van de Waals forces that can cause background staining.

Therefore, a validation of the immunolabeling protocol and antibodies was carried out on PC12-Adh grown on tissue culture plastic. This is done to validate the specificity of the secondary antibody to the primary and to check there was no inadvertent binding of the secondary antibody to the sample. Two different serums were tested for blocking the non-specific binding of the secondary antibody. Usually, serum is chosen based on the animal in which the secondary antibody is grown, horse in this case. This validation may not be as important in cell lines compared to tissues where multiple antibodies may be used and noise due to non-specific binding can become a problem. The results of this validation are shown in Figure 66; only when both primary and secondary antibodies are used, expressed βIII-tubulin is detected.

Immunolabeling was done as described in Chapter 2 Section 2.6.2. This was based on optimised protocols by [252]. However, the expression of βIII tubulin in PC12-Adh cells was not clear as shown in Figure 66. The difference found in the dual labelling of PC12-Adh with

Phalloidin-FITC, a highly selective stain for the F-actin filaments that develop in the cytoplasm of cells, and βIII tubulin antibodies, suggests that βIII tubulin may not be an appropriate marker for PC12-cells. Hence, optimisation with other markers needs to be carried out. Due to time constraints, further optimisation was not possible and Phalloidin-FITC was selected for fluorescence staining in this work.

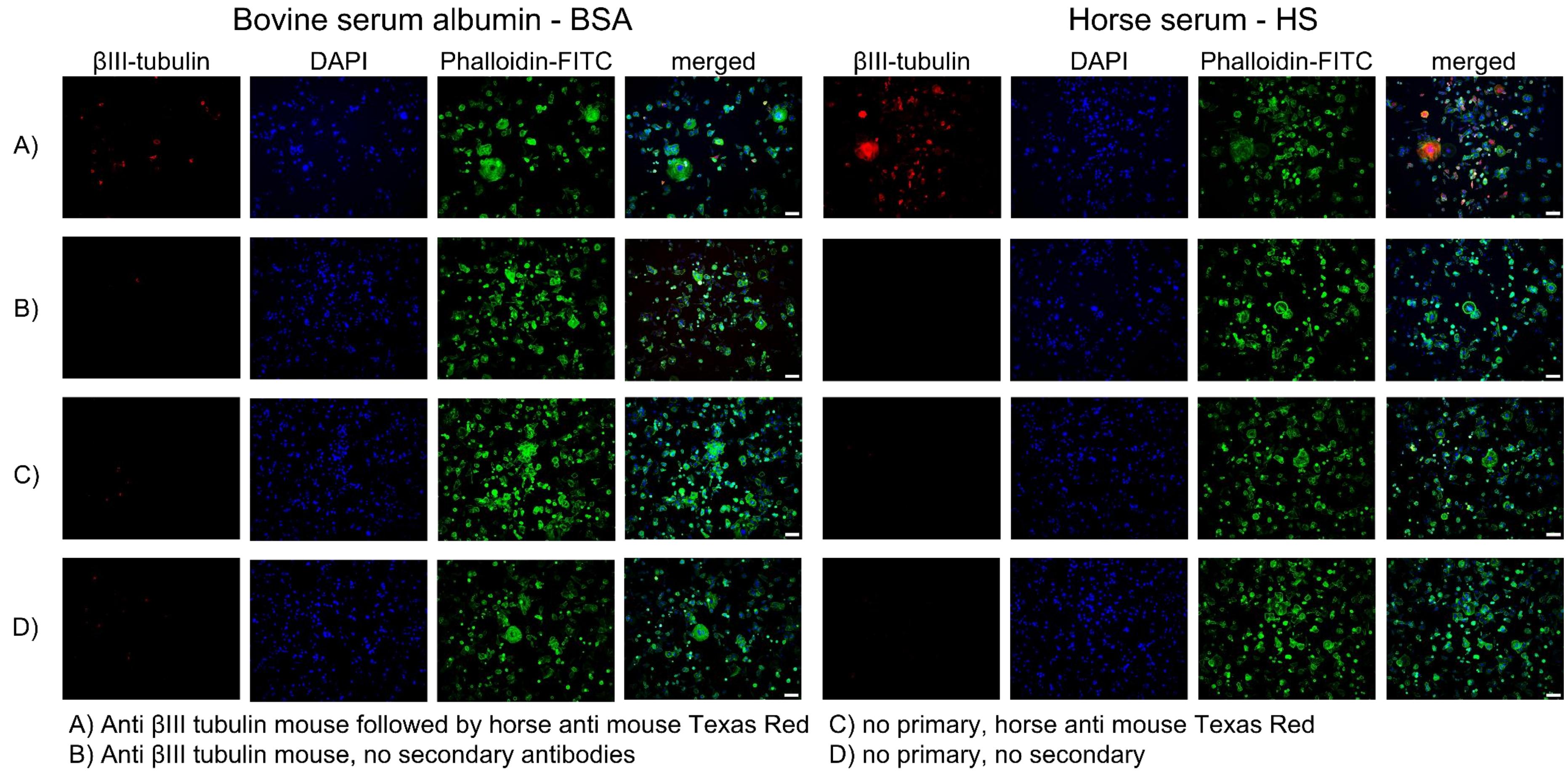

Figure 66. Fluoresce images of PC12-Adh growing on tissue culture plastic (TCP). Cell nuclei are labelled with DAPI (blue) while phalloidin-FITC (green) is used to label F-actin filaments in the cytoskeleton. βIII tubulin is immunolabeled using the antibodies A) anti βIII tubulin mouse followed by horse anti-mouse Texas red, B) anti βIII tubulin mouse, no secondary, C) no primary, horse anti-mouse Texas red, D) no primary, no secondary. For the blocking step bovine serum albumin (BSA) or horse serum (HS) was used. Scale bar represents 100 µm.

References

1. Vepari, C. and D.L. Kaplan, *Silk as a Biomaterial.* Prog Polym Sci, 2007. **32**(8-9): p. 991-1007.
2. Dhyani, V. and N. Singh, *Controlling the cell adhesion property of silk films by graft polymerization.* ACS Appl Mater Interfaces, 2014. **6**(7): p. 5005-11.
3. Coelho, F., et al., *Silk fibroin/hydroxyapatite composite membranes: Production, characterization and toxicity evaluation.* Toxicology in Vitro, 2020. **62**: p. 104670.
4. Andersson, M., J. Johansson, and A. Rising, *Silk Spinning in Silkworms and Spiders.* International Journal of Molecular Sciences, 2016. **17**(8): p. 1290.
5. Plaza, G.R., et al., *Effect of water on Bombyx mori regenerated silk fibers and its application in modifying their mechanical properties.* Journal of Applied Polymer Science, 2008. **109**(3): p. 1793-1801.
6. Plaza, G.R., et al., *Relationship between microstructure and mechanical properties in spider silk fibers: identification of two regimes in the microstructural changes.* Soft Matter, 2012. **8**(22): p. 6015-6026.
7. Zhao, H.-P., X.-Q. Feng, and H.-J. Shi, *Variability in mechanical properties of Bombyx mori silk.* Materials Science and Engineering: C, 2007. **27**(4): p. 675-683.
8. Pérez-Rigueiro, J., et al., *Tensile properties of Argiope trifasciata drag line silk obtained from the spider's web.* Journal of Applied Polymer Science, 2001. **82**(9): p. 2245-2251.
9. Omenetto, F.G. and D.L. Kaplan, *New Opportunities for an Ancient Material.* Science, 2010. **329**(5991): p. 528.
10. Koh, L.-D., et al., *Structures, mechanical properties and applications of silk fibroin materials.* Progress in Polymer Science, 2015. **46**: p. 86-110.
11. Malay, A.D., et al., *Relationships between physical properties and sequence in silkworm silks.* Scientific Reports, 2016. **6**: p. 27573.
12. Rockwood, D.N., et al., *Materials fabrication from Bombyx mori silk fibroin.* Nature Protocols, 2011. **6**: p. 1612-1631.
13. Cao, T.-T. and Y.-Q. Zhang, *Processing and characterization of silk sericin from Bombyx mori and its application in biomaterials and biomedicines.* Materials Science and Engineering: C, 2016. **61**: p. 940-952.
14. Aramwit, P., et al., *Monitoring of inflammatory mediators induced by silk sericin.* Journal of Bioscience and Bioengineering, 2009. **107**(5): p. 556-561.
15. Panilaitis, B., et al., *Macrophage responses to silk.* Biomaterials, 2003. **24**(18): p. 3079-3085.
16. Nayak, S., et al., *The promotion of osseointegration of titanium surfaces by coating with silk protein sericin.* Biomaterials, 2013. **34**(12): p. 2855-2864.

17. Zhang, H.P., et al., *Hydroxyapatite/sericin composite film prepared through mineralization of flexible ethanol-treated sericin film with simulated body fluids.* Ceramics International, 2014. **40**(1, Part A): p. 985-991.

18. Yamada, H., et al., *Preparation of undegraded native molecular fibroin solution from silkworm cocoons.* Materials Science and Engineering: C, 2001. **14**(1): p. 41-46.

19. Gulrajani, M.L., R. Agarwal, and S. Chand, *Degumming of silk with a fungal protease.* Indian Journal of Fibre and Textile Research, 2000. **25**(2): p. 138-142.

20. Zhou, C.-Z., et al., *Fine organization of Bombyx mori fibroin heavy chain gene.* Nucleic Acids Research, 2000. **28**(12): p. 2413-2419.

21. Ha, S.-W., et al., *Structural Study of Irregular Amino Acid Sequences in the Heavy Chain of Bombyx mori Silk Fibroin.* Biomacromolecules, 2005. **6**(5): p. 2563-2569.

22. Cebe, P., et al., *Silk I and Silk II studied by fast scanning calorimetry.* Acta Biomaterialia, 2017. **55**: p. 323-332.

23. Valluzzi, R. and S.P. Gido, *The crystal structure of Bombyx mori silk fibroin at the air–water interface.* Biopolymers, 1997. **42**(6): p. 705-717.

24. Huemmerich, D., U. Slotta, and T. Scheibel, *Processing and modification of films made from recombinant spider silk proteins.* Applied Physics A, 2006. **82**(2): p. 219-222.

25. Lu, S., et al., *The influence of the hydrophilic-lipophilic environment on the structure of silk fibroin protein.* Journal of Materials Chemistry B, 2015. **3**(13): p. 2599-2606.

26. Cheng, Y., et al., *On the strength of β-sheet crystallites of Bombyx mori silk fibroin.* Journal of The Royal Society Interface, 2014. **11**(96).

27. Jacobsen, M.M., et al., *Silk-fibronectin protein alloy fibres support cell adhesion and viability as a high strength, matrix fibre analogue.* Scientific Reports, 2017. **7**: p. 45653.

28. Khorasani, M.T., H. Mirzadeh, and S. Irani, *Plasma surface modification of poly (l-lactic acid) and poly (lactic-co-glycolic acid) films for improvement of nerve cells adhesion.* Radiation Physics and Chemistry, 2008. **77**(3): p. 280-287.

29. Kundu, B., et al., *Silk fibroin biomaterials for tissue regenerations.* Adv Drug Deliv Rev, 2013. **65**(4): p. 457-70.

30. Rajkhowa, R., et al., *Structure and properties of biomedical films prepared from aqueous and acidic silk fibroin solutions.* Journal of Biomedical Materials Research Part A, 2011. **97A**(1): p. 37-45.

31. Hu, K., et al., *Preparation of fibroin/recombinant human-like collagen scaffold to promote fibroblasts compatibility.* Journal of Biomedical Materials Research Part A, 2007. **84A**(2): p. 483-490.

32. Freddi, G., et al., *Silk fibroin/cellulose blend films: Preparation, structure, and physical properties.* Journal of Applied Polymer Science, 2003. **56**(12): p. 1537-1545.

33. Jin, H.-J., et al., *Biomaterial Films of Bombyx Mori Silk Fibroin with Poly(ethylene oxide).* Biomacromolecules, 2004. **5**(3): p. 711-717.

34. Liu, Y., et al., *Thermal and crystalline behaviour of silk fibroin/nylon 66 blend films.* Polymer, 2004. **45**(22): p. 7705-7710.

35. Li, Z.-H., et al., *Silk fibroin-based scaffolds for tissue engineering.* Frontiers of Materials Science, 2013. **7**(3): p. 237-247.

36. Tang, X., et al., *Evaluation on in vitro biocompatibility of silk fibroin-based biomaterials with primarily cultured hippocampal neurons.* Journal of Biomedical Materials Research Part A, 2008. **91A**(1): p. 166-174.

37. Ghaznavi, A.M., et al., *Silk fibroin conduits: a cellular and functional assessment of peripheral nerve repair.* Ann Plast Surg, 2011. **66**(3): p. 273-9.

38. Seo, Y.K., et al., *Correlation between scaffold in vivo biocompatibility and in vitro cell compatibility using mesenchymal and mononuclear cell cultures.* Cell Biology and Toxicology, 2009. **25**(5): p. 513-522.

39. Numata, K., P. Cebe, and D.L. Kaplan, *Mechanism of enzymatic degradation of beta-sheet crystals.* Biomaterials, 2010. **31**(10): p. 2926-2933.

40. Horan, R.L., et al., *In vitro degradation of silk fibroin.* Biomaterials, 2005. **26**(17): p. 3385-3393.

41. Yang, Y., et al., *Degradation behaviors of nerve guidance conduits made up of silk fibroin in vitro and in vivo.* Polymer Degradation and Stability, 2009. **94**(12): p. 2213-2220.

42. Lu, Q., et al., *Degradation mechanism and control of silk fibroin.* Biomacromolecules, 2011. **12**(4): p. 1080-1086.

43. Wang, Y., et al., *In vivo Degradation of Three-Dimensional Silk Fibroin Scaffolds.* Biomaterials, 2008. **29**(24-25): p. 3415-3428.

44. Thurber, A.E., F.G. Omenetto, and D.L. Kaplan, *In vivo bioresponses to silk proteins.* Biomaterials, 2015. **71**: p. 145-157.

45. Jeong, L., et al., *Plasma-treated silk fibroin nanofibers for skin regeneration.* International Journal of Biological Macromolecules, 2009. **44**(3): p. 222-228.

46. Zhang, Q., et al., *Multichannel silk protein/laminin grafts for spinal cord injury repair.* Journal of Biomedical Materials Research Part A, 2016. **104**(12): p. 3045-3057.

47. Yanagisawa, S., et al., *Improving Cell-Adhesive Properties of Recombinant Bombyx mori Silk by Incorporation of Collagen or Fibronectin Derived Peptides Produced by Transgenic Silkworms.* Biomacromolecules, 2007. **8**(11): p. 3487-3492.

48. Sun, W., et al., *Viability and neuronal differentiation of neural stem cells encapsulated in silk fibroin hydrogel functionalized with an IKVAV peptide.* Journal of Tissue Engineering and Regenerative Medicine, 2017. **11**(5): p. 1532-1541.

49. Wang, H., et al., *Effect of RGD-modified silk material on the adhesion and proliferation of bone marrow-derived mesenchymal stem cells.* Journal of Huazhong University of Science and Technology [Medical Sciences], 2009. **29**(1): p. 80-83.

50. Hu, X., et al., *Charge-Tunable Autoclaved Silk-Tropoelastin Protein Alloys That Control Neuron Cell Responses.* Advanced Functional Materials, 2013. **23**(31): p. 3875-3884.

51. Kim, U.J., et al., *Three-dimensional aqueous-derived biomaterial scaffolds from silk fibroin.* Biomaterials, 2005. **26**(15): p. 2775-85.

52. Ajisawa, A., *Dissolution of silk fibroin with calcium chloride/ethanol aqueous solution.* Journal of Sericultural Science of Japan, 1998. **67**: p. 91-94.

53. Wang, X., et al., *Sonication-induced gelation of silk fibroin for cell encapsulation.* Biomaterials, 2008. **29**(8): p. 1054-1064.

54. Yucel, T., P. Cebe, and D.L. Kaplan, *Vortex-Induced Injectable Silk Fibroin Hydrogels.* Biophysical Journal, 2009. **97**(7): p. 2044-2050.

55. Chao, P.-H.G., et al., *Silk hydrogel for cartilage tissue engineering.* Journal of biomedical materials research. Part B, Applied biomaterials, 2010. **95**(1): p. 84-90.

56. Ribeiro, M., et al., *Development of silk fibroin/nanohydroxyapatite composite hydrogels for bone tissue engineering.* European Polymer Journal, 2015. **67**: p. 66-77.

57. Lawrence, B.D., et al., *Silk film biomaterials for cornea tissue engineering.* Biomaterials, 2009. **30**(7): p. 1299-1308.

58. Sanjana, N.E. and S.B. Fuller, *A fast flexible ink-jet printing method for patterning dissociated neurons in culture.* Journal of Neuroscience Methods, 2004. **136**(2): p. 151-163.

59. Tse, C., et al., *Inkjet printing Schwann cells and neuronal analogue NG108-15 cells.* Biofabrication, 2016. **8**(1): p. 015017.

60. Tamura, T., et al., *Germline transformation of the silkworm Bombyx mori L. using a piggyBac transposon-derived vector.* Nature Biotechnology, 2000. **18**(1): p. 81-84.

61. Kambe, Y., et al., *Effects of RGDS sequence genetically interfused in the silk fibroin light chain protein on chondrocyte adhesion and cartilage synthesis.* Biomaterials, 2010. **31**(29): p. 7503-7511.

62. Tomita, M., *Transgenic silkworms that weave recombinant proteins into silk cocoons.* Biotechnology Letters, 2011. **33**(4): p. 645-654.

63. Sahoo, J.K., et al., *Silk chemistry and biomedical material designs.* Nature Reviews Chemistry, 2023. **7**(5): p. 302-318.

64. Serban, M.A. and D.L. Kaplan, *pH-Sensitive Ionomeric Particles Obtained via Chemical Conjugation of Silk with Poly(amino acid)s.* Biomacromolecules, 2010. **11**(12): p. 3406-3412.

65. Hasturk, O., J.K. Sahoo, and D.L. Kaplan, *Synthesis and Characterization of Silk Ionomers for Layer-by-Layer Electrostatic Deposition on Individual Mammalian Cells.* Biomacromolecules, 2020. **21**(7): p. 2829-2843.

66. Sahoo, J.K., et al., *Sugar Functionalization of Silks with Pathway-Controlled Substitution and Properties.* Advanced Biology, 2021. **5**(7): p. 2100388.

67. Murphy, A.R., P.S. John, and D.L. Kaplan, *Modification of silk fibroin using diazonium coupling chemistry and the effects on hMSC proliferation and differentiation.* Biomaterials, 2008. **29**(19): p. 2829-2838.

68. Subia, B., et al., *Folate conjugated silk fibroin nanocarriers for targeted drug delivery.* Integrative Biology, 2014. **6**(2): p. 203-214.

69. Santi, S., et al., *A Bio-inspired Multifunctionalized Silk Fibroin.* ACS Biomaterials Science & Engineering, 2021. **7**(2): p. 507-516.

70. Vidal, G., et al., *Enhanced cellular adhesion on titanium by silk functionalized with titanium binding and RGD peptides.* Acta Biomater, 2013. **9**(1): p. 4935-43.

71. Sofia, S., et al., *Functionalized silk-based biomaterials for bone formation.* Journal of Biomedical Materials Research, 2000. **54**(1): p. 139-148.

72. Wang, X. and D.L. Kaplan, *Functionalization of Silk Fibroin with NeutrAvidin and Biotin.* Macromolecular Bioscience, 2011. **11**(1): p. 100-110.

73. Arslan, E., et al., *Bioactive Supramolecular Peptide Nanofibers for Regenerative Medicine.* Advanced Healthcare Materials, 2014. **3**(9): p. 1357-1376.

74. O'Brien, F.J., *Biomaterials & scaffolds for tissue engineering.* Materials Today, 2011. **14**(3): p. 88-95.

75. Li, C., et al., *Electrospun silk-BMP-2 scaffolds for bone tissue engineering.* Biomaterials, 2006. **27**(16): p. 3115-3124.

76. Rajkhowa, R., et al., *Reinforcing Silk Scaffolds with Silk Particles.* Macromolecular Bioscience, 2010. **10**(6): p. 599-611.

77. Yoo, C.R., et al., *Effect of chitin/silk fibroin nanofibrous bicomponent structures on interaction with human epidermal keratinocytes.* International Journal of Biological Macromolecules, 2008. **42**(4): p. 324-334.

78. Roh, D.-H., et al., *Wound healing effect of silk fibroin/alginate-blended sponge in full thickness skin defect of rat.* Journal of Materials Science: Materials in Medicine, 2006. **17**(6): p. 547-552.

79. Yang, Y., et al., *Biocompatibility evaluation of silk fibroin with peripheral nerve tissues and cells in vitro.* Biomaterials, 2007. **28**(9): p. 1643-52.

80. Kehoe, S., X.F. Zhang, and D. Boyd, *FDA approved guidance conduits and wraps for peripheral nerve injury: a review of materials and efficacy.* Injury, 2012. **43**(5): p. 553-72.

81. Goulart, C.O., et al., *Evaluation of biodegradable polymer conduits – poly(l-lactic acid) – for guiding sciatic nerve regeneration in mice.* Methods, 2016. **99**: p. 28-36.

82. Dinis, T.M., et al., *3D multi-channel bi-functionalized silk electrospun conduits for peripheral nerve regeneration.* J Mech Behav Biomed Mater, 2015. **41**: p. 43-55.

83. Rider, P., et al., *Biocompatible silk fibroin scaffold prepared by reactive inkjet printing.* Journal of Materials Science, 2016. **51**(18): p. 8625-8630.

84. Wittmer, C.R., et al., *Multifunctionalized electrospun silk fibers promote axon regeneration in central nervous system.* Advanced functional materials, 2011. **21**(22): p. 4202-4202.

85. Tian, L., et al., *Coaxial electrospun poly(lactic acid)/silk fibroin nanofibers incorporated with nerve growth factor support the differentiation of neuronal stem cells.* RSC Advances, 2015. **5**(62): p. 49838-49848.

86. Wu, Y., et al., *Self-assembled IKVAV peptide nanofibers promote adherence of PC12 cells.* J Huazhong Univ Sci Technolog Med Sci, 2006. **26**(5): p. 594-6.

87. Sahab Negah, S., et al., *Laminin-derived Ile-Lys-Val-ala-Val: a promising bioactive peptide in neural tissue engineering in traumatic brain injury.* Cell and Tissue Research, 2018. **371**(2): p. 223-236.

88. Kim, J.W., et al., *Effect of RGDS and KRSR peptides immobilized on silk fibroin nanofibrous mats for cell adhesion and proliferation.* Macromolecular Research, 2010. **18**(5): p. 442-448.

89. Mauri, E., et al., *Evaluation of RGD functionalization in hybrid hydrogels as 3D neural stem cell culture systems.* Biomaterials Science, 2018. **6**(3): p. 501-510.

90. Gil, E.S., et al., *Helicoidal multi-lamellar features of RGD-functionalized silk biomaterials for corneal tissue engineering.* Biomaterials, 2010. **31**(34): p. 8953-8963.

91. Kardestuncer, T., et al., *RGD-tethered silk substrate stimulates the differentiation of human tendon cells.* Clin Orthop Relat Res, 2006. **448**: p. 234-9.

92. Chan, B.P. and K.W. Leong, *Scaffolding in tissue engineering: general approaches and tissue-specific considerations.* European Spine Journal, 2008. **17**(Suppl 4): p. 467-479.

93. BioRender. Available from: BioRender.com.

94. More, S.V., S. Chavan, and A.A. Prabhune, *Silk Degumming and Utilization of Silk Sericin by Hydrolysis Using Alkaline Protease from Beauveria Sp. (MTCC 5184): A Green Approach.* Journal of Natural Fibers, 2018. **15**(3): p. 373-383.

95. Wang, W., et al., *A comparative study of ultrasonic degumming of silk sericin using citric acid, sodium carbonate and papain.* Coloration Technology, 2019. **135**(3): p. 195-201.

96. Rahman, M., et al., *Green Degumming of Silk by Enzyme Extracted from Natural Sources.* Journal of Materials Science and Chemical Engineering, 2020. **08**(08): p. 30-40.

97. Phillips, D.M., et al., *Dissolution and Regeneration of Bombyx mori Silk Fibroin Using Ionic Liquids.* Journal of the American Chemical Society, 2004. **126**(44): p. 14350-14351.

98. Bogy, D.B. and F.E. Talke, *Experimental and Theoretical Study of Wave Propagation Phenomena in Drop-on-Demand Ink Jet Devices.* IBM Journal of Research and Development, 1984. **28**(3): p. 314-321.

99. Gregory, D.A., et al., *Reactive Inkjet Printing and Propulsion Analysis of Silk-based Self-propelled Micro-stirrers.* Journal of Visualized Experiments, 2019(146).

100. Gregory, D.A., et al., *Controlling the Composition and Position of Metal–Organic Frameworks via Reactive Inkjet Printing.* Advanced Materials Interfaces, 2023: p. 2300027.

101. Gregory, D.A., et al., *Reactive Inkjet Printing of Biocompatible Enzyme Powered Silk Micro-Rockets.* Small, 2016. **12**(30): p. 4048-4055.

102. Kumar, P., et al., *3D printable self-propelling sensors for the assessment of water quality via surface tension.* JCIS Open, 2022. **5**: p. 100044.

103. Kumar, P., et al., *3D inkjet printed self-propelled motors for micro-stirring.* Journal of Colloid and Interface Science, 2022. **623**: p. 96-108.

104. Yung, H.S., et al., *Nerve Growth Factor-Induced Differentiation of PC12 Cells Is Accompanied by Elevated Adenylyl Cyclase Activity.* Neurosignals, 2010. **18**(1): p. 32-42.

105. Wiatrak, B., et al., *PC12 Cell Line: Cell Types, Coating of Culture Vessels, Differentiation and Other Culture Conditions.* Cells, 2020. **9**(4): p. 958.

106. Sandoval-Castellanos, A.M., F. Claeyssens, and J.W. Haycock, *Bioactive 3D Scaffolds for the Delivery of NGF and BDNF to Improve Nerve Regeneration.* Frontiers in Materials, 2021. **8**.

107. Sandoval-Castellanos, A.M., F. Claeyssens, and J.W. Haycock, *Biomimetic surface delivery of NGF and BDNF to enhance neurite outgrowth.* Biotechnology and Bioengineering, 2020. **117**(10): p. 3124-3135.

108. Kim, H.J., et al., *Effect of degumming methods on structural characteristics and properties of regenerated silk.* International Journal of Biological Macromolecules, 2017. **104**: p. 294-302.

109. Allardyce, B.J., et al., *The impact of degumming conditions on the properties of silk films for biomedical applications.* Textile Research Journal, 2016. **86**(3): p. 275-287.

110. Wang, Z., et al., *Effect of silk degumming on the structure and properties of silk fibroin.* The Journal of The Textile Institute, 2019. **110**(1): p. 134-140.

111. Wray, L.S., et al., *Effect of processing on silk-based biomaterials: Reproducibility and biocompatibility.* Journal of Biomedical Materials Research Part B: Applied Biomaterials, 2011. **99B**(1): p. 89-101.

112. Wang, Y., et al., *Proteomic Analysis of Silk Fibroin Reveals Diverse Biological Function of Different Degumming Processing From Different Origin.* Front Bioeng Biotechnol, 2021. **9**: p. 777320.

113. Wang, Q., et al., *Effect of various dissolution systems on the molecular weight of regenerated silk fibroin.* Biomacromolecules, 2013. **14**(1): p. 285-9.

114. Zhao, Y., et al., *Processing, mechanical properties and bio-applications of silk fibroin-based high-strength hydrogels.* Acta Biomaterialia, 2021. **125**: p. 57-71.

115. Aznar-Cervantes, S.D., et al., *Influence of the protocol used for fibroin extraction on the mechanical properties and fiber sizes of electrospun silk mats.* Materials Science and Engineering: C, 2013. **33**(4): p. 1945-1950.

116. Zhang, X., et al., *Preparation and Biocompatibility Characterization of Regenerated Silk Fibroin Films.* Journal of Macromolecular Science, Part B, 2021. **60**(8): p. 603-615.

117. Cheng, G., et al., *Insignificant Difference in Biocompatibility of Regenerated Silk Fibroin Prepared with Ternary Reagent Compared with Regenerated Silk Fibroin Prepared with Lithium Bromide.* Polymers, 2022. **14**(18): p. 3903.

118. Li, M., et al., *Controlling molecular conformation of regenerated wild silk fibroin by aqueous ethanol treatment.* Polymers for Advanced Technologies, 2003. **14**(10): p. 694-698.

119. Jeong, L., et al., *Time-resolved structural investigation of regenerated silk fibroin nanofibers treated with solvent vapor.* International Journal of Biological Macromolecules, 2006. **38**(2): p. 140-144.

120. Terada, D., et al., *The outermost surface properties of silk fibroin films reflect ethanol-treatment conditions used in biomaterial preparation.* Materials Science and Engineering: C, 2016. **58**: p. 119-126.

121. Puerta, M., et al., *Influence of ethanol post-treatments on the properties of silk protein materials.* SN Applied Sciences, 2019. **1**(11).

122. Kaewpirom, S. and S. Boonsang, *Influence of alcohol treatments on properties of silk-fibroin-based films for highly optically transparent coating applications.* RSC Advances, 2020. **10**(27): p. 15913-15923.

123. Dou, H. and B. Zuo, *Effect of sodium carbonate concentrations on the degumming and regeneration process of silk fibroin.* The Journal of The Textile Institute, 2015. **106**(3): p. 311-319.

124. Wang, Q., et al., *Observations of 3 nm Silk Nanofibrils Exfoliated from Natural Silkworm Silk Fibers.* ACS Materials Letters, 2020. **2**(2): p. 153-160.

125. Tanaka, T., et al., *Thermal properties of bombyx mori and several wild silkworm silks Phase transition of liquid silk.* Journal of Thermal Analysis and Calorimetry, 2002. **70**(3): p. 825-832.

126. Holland, C., et al., *Differential Scanning Calorimetry of Native Silk Feedstock.* Macromolecular Bioscience, 2019. **19**(3): p. 1800228.

127. Moraes, M.A.D., et al., *Preparation and Characterization of Insoluble Silk Fibroin/Chitosan Blend Films.* Polymers, 2010. **2**(4): p. 719-727.

128. Gupta, P., et al., *Mimicking Form and Function of Native Small Diameter Vascular Conduits Using Mulberry and Non-mulberry Patterned Silk Films.* ACS Applied Materials & Interfaces, 2016. **8**(25): p. 15874-15888.

129. Lee, K.Y. and W.S. Ha, *DSC studies on bound water in silk fibroin/S-carboxymethyl kerateine blend films.* Polymer, 1999. **40**(14): p. 4131-4134.

130. Motta, A., L. Fambri, and C. Migliaresi, *Regenerated silk fibroin films: Thermal and dynamic mechanical analysis.* Macromolecular Chemistry and Physics, 2002. **203**(10-11): p. 1658-1665.

131. Mohd Yusoff, N.I.S., et al., *Structural and characterization studies of insoluble thai bombyx mori silk fibroin films.* Malaysian Journal of Fundamental and Applied Sciences, 2019. **15**(1): p. 18-22.

132. Mazzi, S., et al., *Comparative thermal analysis of Eri, Mori, Muga, and Tussar silk cocoons and fibroin fibers.* Journal of Thermal Analysis and Calorimetry, 2014. **116**(3): p. 1337-1343.

133. Wang, H.-Y. and Y.-Q. Zhang, *Effect of regeneration of liquid silk fibroin on its structure and characterization.* Soft Matter, 2013. **9**(1): p. 138-145.

134. Dong, H.-L., et al., *Metabolomics differences between silkworms (Bombyx mori) reared on fresh mulberry (Morus) leaves or artificial diets.* Scientific Reports, 2017. **7**(1).

135. Nultsch, K. and O. Germershaus, *Silk fibroin degumming affects scaffold structure and release of macromolecular drugs.* European Journal of Pharmaceutical Sciences, 2017. **106**: p. 254-261.

136. Zhang, F., et al., *Silk dissolution and regeneration at the nanofibril scale.* Journal of Materials Chemistry B, 2014. **2**(24): p. 3879.

137. Kundu, B., et al., *Isolation and processing of silk proteins for biomedical applications.* International Journal of Biological Macromolecules, 2014. **70**: p. 70-77.

138. Ribeiro, M., et al., *The role of dialysis and freezing on structural conformation, thermal properties and morphology of silk fibroin hydrogels.* Biomatter, 2014. **4**(1): p. e28536.

139. Meng, L., et al., *Autonomous Self-Healing Silk Fibroin Injectable Hydrogels Formed via Surfactant-Free Hydrophobic Association.* ACS Applied Materials & Interfaces, 2020. **12**(1): p. 1628-1639.

140. Zhang, L., et al., *Tailoring degradation rates of silk fibroin scaffolds for tissue engineering.* Journal of Biomedical Materials Research Part A, 2019. **107**(1): p. 104-113.

141. Iwasaki, Y., et al., *Induction of a Distinct Morphology and Signal Transduction in TrkB/PC12 Cells by Nerve Growth Factor and Brain-Derived Neurotrophic Factor.* Journal of Neurochemistry, 2002. **68**(3): p. 927-934.

142. Oprea, D., et al., *PC-12 Cell Line as a Neuronal Cell Model for Biosensing Applications.* Biosensors, 2022. **12**(7): p. 500.

143. Nogueira, G.M., et al., *Preparation and characterization of ethanol-treated silk fibroin dense membranes for biomaterials application using waste silk fibers as raw material.* Bioresource Technology, 2010. **101**(21): p. 8446-8451.

144. Lee, S., et al., *Conformation Transition Kinetics of Silk Fibroin in Aqueous Solution Explored Using Circular Dichroism Spectroscopy.* ChemistrySelect, 2021. **6**(8): p. 1735-1740.

145. Grasman, J.M., et al., *The Effect of Sterilization Methods on the Structural and Chemical Properties of Fibrin Microthread Scaffolds.* Macromolecular Bioscience, 2016. **16**(6): p. 836-846.

146. Rnjak-Kovacina, J., et al., *The Effect of Sterilization on Silk Fibroin Biomaterial Properties.* Macromolecular Bioscience, 2015. **15**(6): p. 861-874.

147. Gil, E.S., et al., *Impact of Sterilization on the Enzymatic Degradation and Mechanical Properties of Silk Biomaterials.* Macromolecular Bioscience, 2014. **14**(2): p. 257-269.

148. De Moraes, M.A., R.F. Weska, and M.M. Beppu, *Effects of sterilization methods on the physical, chemical, and biological properties of silk fibroin membranes.* Journal of Biomedical Materials Research Part B: Applied Biomaterials, 2014. **102**(4): p. 869-876.

149. Feoktistova, M., P. Geserick, and M. Leverkus, *Crystal Violet Assay for Determining Viability of Cultured Cells.* Cold Spring Harbor Protocols, 2016. **2016**(4): p. pdb.prot087379.

150. Wang, H.-Y., Y.-Q. Zhang, and Z.-G. Wei, *Dissolution and processing of silk fibroin for materials science.* Critical Reviews in Biotechnology, 2021. **41**(3): p. 406-424.

151. Lavogina, D., et al., *Revisiting the Resazurin-Based Sensing of Cellular Viability: Widening the Application Horizon.* Biosensors, 2022. **12**(4): p. 196.

152. Silva, F.S.G., et al., *Determination of Metabolic Viability and Cell Mass Using a Tandem Resazurin/Sulforhodamine B Assay.* Current Protocols in Toxicology, 2016. **68**(1): p. 2.24.1-2.24.15.

153. Sivkova, R., et al., *Surface Design of Antifouling Vascular Constructs Bearing Biofunctional Peptides for Tissue Regeneration Applications.* International Journal of Molecular Sciences, 2020. **21**(18): p. 6800.

154. Damodaran, V.B. and N.S. Murthy, *Bio-inspired strategies for designing antifouling biomaterials.* Biomaterials Research, 2016. **20**(1).

155. Wang, R., et al., *Forward Wound Closure with Regenerated Silk Fibroin and Polylysine-Modified Chitosan Composite Bioadhesives as Dressings.* ACS Applied Bio Materials, 2020. **3**(11): p. 7941-7951.

156. Li, C., et al., *ε-Poly-l-lysine-modified natural silk fiber membrane wound dressings with improved antimicrobial properties.* International Journal of Biological Macromolecules, 2022. **220**: p. 1049-1059.

157. Kim, Y.H., et al., *Enhancement of neuronal cell adhesion by covalent binding of poly-d-lysine.* Journal of Neuroscience Methods, 2011. **202**(1): p. 38-44.

158. Chwalek, K., et al., *Engineered 3D Silk-collagen-based Model of Polarized Neural Tissue.* Journal of Visualized Experiments : JoVE, 2015(104): p. 52970.

159. Chwalek, K., et al., *In vitro bioengineered model of cortical brain tissue.* Nature Protocols, 2015. **10**: p. 1362.

160. Kang, Z., et al., *An RGD-Containing Peptide Derived from Wild Silkworm Silk Fibroin Promotes Cell Adhesion and Spreading.* Polymers, 2018. **10**(11): p. 1193.

161. Wei, J., X.-Q. Sun, and B.-X. Hou, *Evaluation of Silk Fibroin-RGD-Stem Cell Factor Scaffold Effect on Adhesion, Migration, and Proliferation of Stem Cells of Apical Papilla.* Stem Cells International, 2021. **2021**: p. 1-10.

162. Castro-Domínguez, C., et al., *Axonal Guidance Using Biofunctionalized Straining Flow Spinning Regenerated Silk Fibroin Fibers as Scaffold.* Biomimetics, 2023. **8**(1): p. 65.

163. He, Y. and F. Lu, *Development of Synthetic and Natural Materials for Tissue Engineering Applications Using Adipose Stem Cells.* Stem Cells International, 2016. **2016**: p. 1-12.

164. Sedighi, M., et al. *Multifunctional Self-Assembled Peptide Hydrogels for Biomedical Applications*. Polymers, 2023. **15**, DOI: 10.3390/polym15051160.

165. Jung, J.P., et al., *Co-assembling peptides as defined matrices for endothelial cells.* Biomaterials, 2009. **30**(12): p. 2400-2410.

166. Acar, H., et al., *Self-assembling peptide-based building blocks in medical applications.* Advanced Drug Delivery Reviews, 2017. **110-111**: p. 65-79.

167. Ding, X., et al., *Synthetic peptide hydrogels as 3D scaffolds for tissue engineering.* Advanced Drug Delivery Reviews, 2020. **160**: p. 78-104.

168. Chen, J. and X. Zou, *Self-assemble peptide biomaterials and their biomedical applications.* Bioactive Materials, 2019. **4**: p. 120-131.

169. Tan, A., J. Rajadas, and A.M. Seifalian, *Biochemical engineering nerve conduits using peptide amphiphiles.* Journal of Controlled Release, 2012. **163**(3): p. 342-352.

170. Tysseling, V.M., et al., *Self-assembling peptide amphiphile promotes plasticity of serotonergic fibers following spinal cord injury.* Journal of Neuroscience Research, 2010. **88**(14): p. 3161-3170.

171. Panda, J.J. and V.S. Chauhan, *Short peptide based self-assembled nanostructures: implications in drug delivery and tissue engineering.* Polym. Chem., 2014. **5**(15): p. 4431-4449.

172. Sieminski, A.L., et al., *Primary sequence of ionic self-assembling peptide gels affects endothelial cell adhesion and capillary morphogenesis.* Journal of Biomedical Materials Research Part A, 2008. **87A**(2): p. 494-504.

173. Yang, S., et al., *Self-assembling peptide hydrogels functionalized with LN- and BDNF-mimicking epitopes synergistically enhance peripheral nerve regeneration.* Theranostics, 2020. **10**(18): p. 8227-8249.

174. Lu, C., et al., *Bioactive Self-Assembling Peptide Hydrogels Functionalized with Brain-Derived Neurotrophic Factor and Nerve Growth Factor Mimicking Peptides Synergistically Promote Peripheral Nerve Regeneration.* ACS Biomaterials Science & Engineering, 2018. **4**(8): p. 2994-3005.

175. Shen, X., et al., *Repairing sciatic nerve injury with self-assembling peptide nanofiber scaffold-containing chitosan conduit.* Front Neurol, 2022. **13**: p. 867711.

176. Xu, H., et al., *Twisted Nanotubes Formed from Ultrashort Amphiphilic Peptide I3K and Their Templating for the Fabrication of Silica Nanotubes.* Chemistry of Materials, 2010. **22**(18): p. 5165-5173.

177. Isidro-Llobet, A., M. Álvarez, and F. Albericio, *Amino Acid-Protecting Groups.* Chemical Reviews, 2009. **109**(6): p. 2455-2504.

178. Wang, Q., et al., *Self-assembled peptide nanotubes as potential nanocarriers for drug delivery.* RSC Advances, 2014. **4**(48): p. 25461.

179. Deshmukh, S.A., et al., *Water ordering controls the dynamic equilibrium of micelle–fibre formation in self-assembly of peptide amphiphiles.* Nature Communications, 2016. **7**(1): p. 12367.

180. Wong Po Foo, C., et al., *Role of pH and charge on silk protein assembly in insects and spiders.* Applied Physics A, 2006. **82**: p. 223-233.

181. Aye, S.S.S., et al., *Silk Hydrogel Electrostatically Functionalized with a Polycationic Antimicrobial Peptide: Molecular Interactions, Gel Properties, and Antimicrobial Activity.* Langmuir, 2022. **38**(1): p. 50-61.

182. Beena, M., J.M. Ameer, and N. Kasoju, *Optically Clear Silk Fibroin Films with Tunable Properties for Potential Corneal Tissue Engineering Applications: A Process–Property–Function Relationship Study.* ACS Omega, 2022. **7**(34): p. 29634-29646.

183. Ramachandran, C., et al., *In Vitro Culture of Human Corneal Endothelium on Non-Mulberry Silk Fibroin Films for Tissue Regeneration.* Translational Vision Science & Technology, 2020. **9**(4): p. 12-12.

184. Lawrence, B.D., et al., *Effect of Hydration on Silk Film Material Properties.* Macromolecular Bioscience, 2010. **10**(4): p. 393-403.

185. Starinskiy, S., et al., *Spreading of Impacting Water Droplet on Surface with Fixed Microstructure and Different Wetting from Superhydrophilicity to Superhydrophobicity.* Water, 2023. **15**(4): p. 719.

186. Al-Azzam, N. and A. Alazzam, *Micropatterning of cells via adjusting surface wettability using plasma treatment and graphene oxide deposition.* PLOS ONE, 2022. **17**(6): p. e0269914.

187. Arima, Y. and H. Iwata, *Effect of wettability and surface functional groups on protein adsorption and cell adhesion using well-defined mixed self-assembled monolayers.* Biomaterials, 2007. **28**(20): p. 3074-3082.

188. Zhang, B. and W. Xu, *Superhydrophobic, superamphiphobic and SLIPS materials as anti-corrosion and anti-biofouling barriers.* New Journal of Chemistry, 2021. **45**(34): p. 15170-15179.

189. Fountain, J.N., et al., *Towards Non-stick Silk: Tuning the Hydrophobicity of Silk Fibroin Protein.* ChemBioChem, 2022. **23**(22).

190. Xu, Y., et al., *A Silk Fibroin/Collagen Nerve Scaffold Seeded with a Co-Culture of Schwann Cells and Adipose-Derived Stem Cells for Sciatic Nerve Regeneration.* PLOS ONE, 2016. **11**(1): p. e0147184.

191. Chen, J., et al., *Human bone marrow stromal cell and ligament fibroblast responses on RGD-modified silk fibers.* Journal of Biomedical Materials Research Part A, 2003. **67A**(2): p. 559-570.

192. W., M.D.S.G.S., *Adhesion of cells to surfaces coated with polylysine. Applications to electron microscopy.* The Journal of Cell Biology, 1975. **66**(1): p. 198-200.

193. Mao, S., et al., *Measurement of Cell–Matrix Adhesion at Single-Cell Resolution for Revealing the Functions of Biomaterials for Adherent Cell Culture.* Analytical Chemistry, 2018. **90**(15): p. 9637-9643.

194. Xing, G.-W., et al., *Capture of cervical exfoliative cells on a glass slide coated by 3-glycidyloxypropyl trimethoxysilane and poly-L-lysine.* Journal of Pharmaceutical Analysis, 2012. **2**(3): p. 174-179.

195. Tang-Schomer, M.D., et al., *Bioengineered functional brain-like cortical tissue.* Proceedings of the National Academy of Sciences, 2014. **111**(38): p. 13811.

196. Sun, W., et al., *Patterning the neuronal cells via inkjet printing of self-assembled peptides on silk scaffolds.* Progress in Natural Science: Materials International, 2020. **30**(5): p. 686-696.

197. Sun, W., et al., *Cell guidance on peptide micropatterned silk fibroin scaffolds.* Journal of Colloid and Interface Science, 2021. **603**: p. 380-390.

198. Khalili, A.A. and M.R. Ahmad, *A Review of Cell Adhesion Studies for Biomedical and Biological Applications.* International journal of molecular sciences, 2015. **16**(8): p. 18149-18184.

199. Cantini, M., et al., *Non-monotonic cell differentiation pattern on extreme wettability gradients.* Biomater. Sci., 2013. **1**(2): p. 202-212.

200. Jahani, H., et al., *Controlled surface morphology and hydrophilicity of <i>polycaprolactone</i> toward selective differentiation of mesenchymal stem cells to neural like cells.* Journal of Biomedical Materials Research Part A, 2015. **103**(5): p. 1875-1881.

201. Varani, J., et al., *Use of recombinant and synthetic peptides as attachment factors for cells on microcarriers.* Cytotechnology, 1993. **13**(2): p. 89-98.

202. Zarrintaj, P., et al., *Polylysine for skin regeneration: A review of recent advances and future perspectives.* Bioengineering & Translational Medicine, 2022. **7**(1).

203. Wang, Q., et al., *Morphology-controlled synthesis of silica materials templated by self-assembled short amphiphilic peptides.* RSC Advances, 2013. **3**(36): p. 15955-15965.

204. Oropeza, B.P., et al., *Assessment of Angiogenesis and Cell Survivability of an Inkjet Bioprinted Biological Implant in an Animal Model.* Materials, 2022. **15**(13): p. 4468.

205. Solis, L.H., et al., *Thermal inkjet bioprinting triggers the activation of the VEGF pathway in human microvascular endothelial cells in vitro.* Biofabrication, 2019. **11**(4): p. 045005.

206. Montenegro-Nicolini, M., V. Miranda, and J.O. Morales, *Inkjet Printing of Proteins: an Experimental Approach.* The AAPS Journal, 2017. **19**(1): p. 234-243.

207. Lee, K.B., et al., *A versatile method for dynamically controlled patterning of small populations of epithelial cells on substrates via non-contact piezoelectric inkjet printing.* PLOS ONE, 2017. **12**(4): p. e0176079.

208. Lorber, B., et al., *Adult rat retinal ganglion cells and glia can be printed by piezoelectric inkjet printing.* Biofabrication, 2014. **6**(1): p. 015001.

209. Saunders, R.E., J.E. Gough, and B. Derby, *Delivery of human fibroblast cells by piezoelectric drop-on-demand inkjet printing.* Biomaterials, 2008. **29**(2): p. 193-203.

210. Barui, S., et al., *Acoustic Poration and Dynamic Healing of Mammalian Cell Membranes during Inkjet Printing.* ACS Biomaterials Science and Engineering, 2020. **6**(1): p. 749-757.

211. Park, J.A., et al., *Freeform micropatterning of living cells into cell culture medium using direct inkjet printing.* Scientific Reports, 2017. **7**(1): p. 14610.

212. Guo, J., et al., *Coding Cell Micropatterns Through Peptide Inkjet Printing for Arbitrary Biomineralized Architectures.* Advanced Functional Materials, 2018. **28**(19): p. 1800228.

213. MicroFab Technologies Inc., U.; Available from: http://www.microfab.com/index.php?option=com_content&view=article&id=140&Itemid=160.

214. Zhang, Y., et al., *Scaffolds for tissue engineering produced by inkjet printing.* Open Engineering, 2012. **2**(3).

215. Cai, S., et al., *Recent advance in surface modification for regulating cell adhesion and behaviors.* Nanotechnology Reviews, 2020. **9**(1): p. 971-989.

216. Falconnet, D., et al., *Surface engineering approaches to micropattern surfaces for cell-based assays.* Biomaterials, 2006. **27**(16): p. 3044-3063.

217. Cai, K., et al., *Inkjet printing of laminin gradient to investigate endothelial cellular alignment.* Colloids and Surfaces B: Biointerfaces, 2009. **72**(2): p. 230-235.

218. Ker, E.D.F., et al., *Bioprinting of growth factors onto aligned sub-micron fibrous scaffolds for simultaneous control of cell differentiation and alignment.* Biomaterials, 2011. **32**(32): p. 8097-8107.

219. Offenhäusser, A., et al., *Microcontact printing of proteins for neuronal cell guidance.* Soft Matter, 2007. **3**(3): p. 290-298.

220. Hussain, A., N. Abbas, and A. Ali *Inkjet Printing: A Viable Technology for Biosensor Fabrication*. Chemosensors, 2022. **10**, DOI: 10.3390/chemosensors10030103.

221. Li, X., et al., *Aligned Scaffolds With Biomolecular Gradients for Regenerative Medicine.* Polymers, 2019. **11**(2): p. 341.

222. Hart, L.R., et al., *Supramolecular Approach to New Inkjet Printing Inks.* Acs Applied Materials & Interfaces, 2015. **7**(16): p. 8906-8914.

223. Wu, C.-H. and W.-S. Hwang, *The effect of the echo-time of a bipolar pulse waveform on molten metallic droplet formation by squeeze mode piezoelectric inkjet printing.* Microelectronics Reliability, 2015. **55**(3): p. 630-636.

224. Zhang, Y., et al., *Suppression and Utilization of Satellite Droplets for Inkjet Printing: A Review.* Processes, 2022. **10**(5): p. 932.

225. Lohse, D., *Fundamental Fluid Dynamics Challenges in Inkjet Printing.* Annual Review of Fluid Mechanics, 2022. **54**(1): p. 349-382.

226. Fromm, J.E., *Numerical Calculation of the Fluid Dynamics of Drop-on-Demand Jets.* IBM Journal of Research and Development, 1984. **28**(3): p. 322-333.

227. Derby, B. and N. Reis, *Inkjet Printing of Highly Loaded Particulate Suspensions.* MRS Bulletin, 2003. **28**(11): p. 815-818.

228. Liu, Y. and B. Derby, *Experimental study of the parameters for stable drop-on-demand inkjet performance.* Physics of Fluids, 2019. **31**(3): p. 032004.

229. McIlroy, C. and O.G. Harlen, *Effects of drive amplitude on continuous jet break-up.* Physics of Fluids, 2019. **31**(6): p. 064104.

230. Chen, A.U. and O.A. Basaran, *A new method for significantly reducing drop radius without reducing nozzle radius in drop-on-demand drop production.* Physics of Fluids, 2002. **14**(1): p. L1-L4.

231. Dong, H., W.W. Carr, and J.F. Morris, *An experimental study of drop-on-demand drop formation.* Physics of Fluids, 2006. **18**(7): p. 072102.

232. Janssen, D., et al., *Static solvent contact angle measurements, surface free energy and wettability determination of various self-assembled monolayers on silicon dioxide.* Thin Solid Films, 2006. **515**(4): p. 1433-1438.

233. Huhtamäki, T., et al., *Surface-wetting characterization using contact-angle measurements.* Nature Protocols, 2018. **13**(7): p. 1521-1538.

234. Modak, C.D., et al., *Drop impact printing.* Nature Communications, 2020. **11**(1).

235. Hu, S., et al., *Morphology simulation of drop-on-demand inkjet-printed droplets.* npj Flexible Electronics, 2022. **6**(1).

236. Yarin, A.L., *DROP IMPACT DYNAMICS: Splashing, Spreading, Receding, Bouncing….* Annual Review of Fluid Mechanics, 2006. **38**(1): p. 159-192.

237. Perelaer, J., et al., *The Spreading of Inkjet-Printed Droplets with Varying Polymer Molar Mass on a Dry Solid Substrate.* Macromolecular Chemistry and Physics, 2009. **210**(6): p. 495-502.

238. Soltman, D. and V. Subramanian, *Inkjet-Printed Line Morphologies and Temperature Control of the Coffee Ring Effect.* Langmuir, 2008. **24**(5): p. 2224-2231.

239. Mu, L., et al., *Inkjet-printing line film with varied droplet-spacing.* Organic Electronics, 2017. **51**: p. 308-313.

240. Lim, J.A., et al., *Self-Organization of Ink-jet-Printed Triisopropylsilylethynyl Pentacene via Evaporation-Induced Flows in a Drying Droplet.* Advanced Functional Materials, 2008. **18**(2): p. 229-234.

241. Uddin, M.J., J. Hassan, and D. Douroumis, *Thermal Inkjet Printing: Prospects and Applications in the Development of Medicine.* Technologies, 2022. **10**(5): p. 108.

242. van Gaalen, R.T., et al., *Marangoni circulation in evaporating droplets in the presence of soluble surfactants.* Journal of Colloid and Interface Science, 2021. **584**: p. 622-633.

243. Heine, J.S. and H.J. Bart, *Local analysis of Marangoni effects during and after droplet formation.* The Canadian Journal of Chemical Engineering, 2020. **98**(5): p. 1164-1171.

244. He, P. and B. Derby, *Controlling Coffee Ring Formation during Drying of Inkjet Printed 2D Inks.* Advanced Materials Interfaces, 2017. **4**(22): p. 1700944.

245. Seo, C., et al., *Altering the coffee-ring effect by adding a surfactant-like viscous polymer solution.* Scientific Reports, 2017. **7**(1): p. 500.

246. Konstantinides, N. and C. Desplan, *Neuronal differentiation strategies: insights from single-cell sequencing and machine learning.* Development, 2020. **147**(23): p. dev193631.

247. Nabiuni, M., et al., *In vitro effects of fetal rat cerebrospinal fluid on viability and neuronal differentiation of PC12 cells.* Fluids and Barriers of the CNS, 2012. **9**(1): p. 8.

248. Fang, Y., et al., *3D Printed Conductive Multiscale Nerve Guidance Conduit With Hierarchical Fibers for Peripheral Nerve Regeneration.* Advanced Science, 2023. **10**(12).

249. Petcu, E., et al., *3D Printing Strategies for Peripheral Nerve Regeneration.* Biofabrication, 2018. **10**(3): p. 032001.

250. Jiang, S.M., et al., *β-III-Tubulin: a reliable marker for retinal ganglion cell labeling in experimental models of glaucoma.* Int J Ophthalmol, 2015. **8**(4): p. 643-52.

251. Xu, S.-Y., et al., *A Modified Technique for Culturing Primary Fetal Rat Cortical Neurons.* Journal of Biomedicine and Biotechnology, 2012. **2012**: p. 1-7.

252. Sandoval-Castellanos, A.M., *Bioactive surfaces for the delivery of nerve growth factor and brain derived neurotrophic factor and its effects in neurite outgrowth*. 2021, University of Sheffield.